

**CUCURBITURIL-BASED
SUPRAMOLECULAR CONSTRUCTS FOR
THE DIVERSE APPLICATIONS OF
NANOMEDICINE**

A THESIS SUBMITTED TO
THE GRADUATE SCHOOL OF ENGINEERING AND SCIENCE
OF BILKENT UNIVERSITY
IN PARTIAL FULFILLMENT OF THE REQUIREMENTS FOR
THE DEGREE OF
MASTER OF SCIENCE
IN
MATERIALS SCIENCE AND NANOTECHNOLOGY

By
Melis Özkan
August 2020

CUCURBITURIL-BASED SUPRAMOLECULAR CONSTRUCTS
FOR THE DIVERSE APPLICATIONS OF NANOMEDICINE

By Melis Özkan

August 2020

We certify that we have read this thesis and that in our opinion it is fully adequate,
in scope and in quality, as a thesis for the degree of Master of Science.

Dönüş Tuncel(Advisor)

Fatih İnci

İrem Erel Göktepe

Approved for the Graduate School of Engineering and Science:

Ezhan Kardeşan
Director of the Graduate School

ABSTRACT

CUCURBITURIL-BASED SUPRAMOLECULAR CONSTRUCTS FOR THE DIVERSE APPLICATIONS OF NANOMEDICINE

Melis Özkan

M.Sc. in Materials Science and Nanotechnology

Advisor: Dönüş Tuncel

August 2020

The supramolecular chemistry of cucurbiturils (CBs) has been rapidly advancing to span wide range of nanomedicine applications including but not limited to pharmaceutical drug formulation and delivery, bio/medical imaging and sensing, cancer therapy, tissue engineering, development of antibacterial/antiviral agents and protein modification. Owing to unique recognition properties and low cytotoxicity, the supramolecular assemblies of CBs are particular promises for biomedicine tasks. Inspired by these developments, three multifunctional supramolecular constructs of CBs containing photoactive conjugated compounds were prepared to be utilized in nanomedicine applications covering antimicrobial and anticancer photodynamic therapy (PDT), combined PDT and photothermal therapy (PTT) for the inactivation of bacteria, drug delivery and cellular imaging.

A stable rotaxane, namely [5]-rotaxane, based on photoactive alkyne-substituted porphyrin and azide-substituted stopper group was synthesized through 1,3-dipolar cycloaddition reaction. Herein, cucurbit[6]uril (CB6) acts as both macrocycle and catalysis for the reaction and encapsulates formed triazole ring inside its cavity. [5]-rotaxane was further investigated and results revealed that it has ability to generate reactive oxygen species (ROS) including singlet oxygens in high yield even under quite low fluence of light and short exposure time and this, in turn, renders it ideal photosensitizer which remains stable at physiological pH (7.4) for prolonged times. By taking the advantages of aforementioned properties, [5]-rotaxane was employed as a broad-spectrum antibacterial agent against Gram-negative and Gram-positive bacteria as well as anticancer agent against human breast cancer cell line (MCF-7) via visible-light-induced generation of ROS. [5]-rotaxane possess negligible dark cytotoxicity upon complexation with CB6 and it can afford efficacious PDT of cancer and infectious

diseases caused by bacteria.

Another multifunctional photoactive supramolecular assembly was built through covalently binding of four cucurbit[7]uril (CB7) molecules, functioning as receptor, to a tetraphenyl porphyrin core using suitable linkers. In addition to its light-promoted antibacterial property, here, main objective was to combine chemo- and photodynamic cancer therapy which makes this study novel. Presence of CB7, enables host-guest interactions with anticancer drug, doxorubicin hydrochloride (DOX), and therefore this system was used to carry drug molecules achieving synergistic PDT and chemotherapy.

Finally, CB7-capped hybrid nanoparticles (NPs) made up of red-emitting conjugated oligomer (COL) and gold nanoparticles (Au-NPs) were obtained through one-pot synthetic method. These hybrid NPs were found to own high photostability, thermal reversibility and high ROS generation capacity. Benefitting from these properties, combined photodynamic and photothermal killing efficiency of NPs towards Gram-positive and Gram-negative bacteria was verified. Additionally, cellular imaging capability of them was shown owing to their inherently fluorescent characteristics and this feature could be utilized for image-guided PDT applications.

Keywords: Cucurbituril, photoactive conjugated compounds, porphyrin, supramolecular chemistry, nanomedicine applications.

ÖZET

ÇEŞİTLİ NANOTIP UYGULAMALARI İÇİN KÜKÜRBITÜRİL TABANLI SUPRAMOLEKÜLER YAPILAR

Melis Özkan

Malzeme Bilimi ve Nanoteknoloji, Yüksek Lisans

Tez Danışmanı: Dönüş Tuncel

Ağustos 2020

Kükürbitürillerin supramoleküler kimyası, farmasötik ilaç formülasyonu ve dağıtımı, biyo/tıbbi görüntüleme ve algılama, kanser tedavisi, doku mühendisliği, antibakteriyel/antiviral ajanların geliştirilmesi ve protein modifikasyonunu gibi uygulamaları da kapsayan ancak bunlarla sınırlı olmayan çeşitli nanotip uygulamaları için hızla gelişmektedir. Eşsiz tanıma özellikleri ve düşük sitotoksite sayesinde, kükürbitürillerin supramoleküler düzenekleri biyotıp görevleri için özellikle gelecek vaat etmektedir. Bu gelişmelerden ilham alınarak, üç adet çok işlevli, fotoaktif konjüge edilmiş bileşenler içeren, kükürbitüril tabanlı supramoleküler yapılar, antimikrobiyal ve antikanser fotodinamik terapi (PDT), bakterilerin inaktivasyonu için kombine PDT ve fototermal terapi (PTT), ilaç taşınımı ve hücresel görüntülemeyi içeren nanotip uygulamalarında kullanılmak üzere hazırlanmıştır.

Fotoaktif alkinlenmiş porfirin ve azid ile fonksiyonelleşmiş durdurucu grup-tan oluşan kararlı rotaksan, isimsel olarak, [5]-rotaksan, 1,3-dipolar siklokatılma reaksiyonları yoluyla sentezlendi. Burada, kükürbit[6]üril (CB6) reaksiyon için hem makrosikle hem de kataliz görevi görür ve oluşan triazol halkasını kendi boşluğu içinde kapsül içine alır.[5]-rotaksan daha fazla araştırılmış ve sonuçlar, [5]-rotaksanın singlet oksijenleri de içeren reaktif oksijen türlerini (ROS), yüksek verimde üretme kabiliyetine sahip olduğunu ortaya koymuştur ve bu da onu uzun süre fizyolojik pH'da (7.4) sabit kalan ideal fotosensitizör yapar. Yukarıda belirtilen özelliklerin avantajları kullanılarak [5]-rotaksan, çok düşük akıda ve kısa süreli maruz zamanındaki görünür ışıkla bile tetiklelenen ROS üretimi aracılığıyla, Gram-negatif ve Gram-pozitif bakterilere karşı geniş spektrumlu antibakteriyel ajan olarak ve insan meme kanseri hücre hattına (MCF-7) karşı

antikanser ajan olarak kullanılmıştır.[5]-rotaksanın, kükürbit[6]üril ile kompleksleşme üzerine karanlıkta ihmal edilebilir sitotoksositeye sahip olduğu ve böylece kansere ve bakterilerin neden olduğu bulaşıcı hastalıklara karşı etkili PDT fırsatı sağladığı görülmüştür.

Bir başka çok işlevli fotoaktif supramoleküler düzenek, bir tetrafenil porfirin çekirdeğine, reseptör olarak işlev gören dört kükürbit[7]üril molekülünün uygun bağlayıcılarla kovalent bağlantısı sonucu inşa edildi. Sadece ışıpta tetiklenen antibakteriyel özelliğine ek olarak, buradaki temel amaç, kemo ve fotodinamik kanser terapilerini birleştirerek, çalışmaya yenilik katmaktır. Kükürbit[7]ürillerin varlığı, antikanser ilacı, doksorubisin hidroklorür (DOX) ile konakçı konuk etkileşimlerini mümkün kılar ve bu sayede bu sistemin, ilaç moleküllerini taşıyarak, sinerjistik PDT ve kemoterapi için uygunluğu doğrulanmıştır.

Son olarak, kükürbit[7]üril ile kaplanmış, kırmızı yayıcı konjüge oligomer (COL) ve altın nanopartiküllerden (Au-NP'ler) oluşan hibrid nanoparçacıklar (NP'ler) tek potlu sentetik yöntemle elde edildi. Bu hibrid NP'lerin yüksek fotostabilite, termal tersinirlik ve yüksek ROS üretim kapasitesine sahip olduğu bulundu. Bu özelliklerden faydalanarak, NP'lerin Gram-pozitif ve Gram-negatif bakterilere karşı kombine fotodinamik ve fototermal inhibe edici etkisi anlaşılmıştır. Bunlara ek olarak, bu NP'lerin kendinden floresan özellikleri sayesinde hücresel görüntüleme kabiliyeti gösterilmiştir ve bu özellik görüntü kılavuzlu PDT uygulamaları için kullanılabilir.

Anahtar sözcükler: Kükürbitüril, fotoaktif konjüge bileşimler, porfirin, supramoleküler kimya, nanotıp uygulamaları.

Acknowledgement

First of all, I would like to express my deepest gratitudes and respect to my supervisor Assoc. Prof. Dönüş Tuncel for her invaluable and continuous support, guidance, patience and time since my undergraduate years. I am inexpressibly lucky and grateful to have such role model inspiring and motivating me with her enthusiasm, distinguished vision and teaching. I thank her for providing a solid start to my research career and making me come closer to becoming a true scientist. I truly appreciate all the opportunities she has offered me, but most importantly, I acknowledge her for being a great person and a great mentor alongside being an exemplary scientist. It is a rare privilege to be a part of DT Lab.

I am thankful to examining committee members, Asst. Prof. Fatih İnci and Assoc. Prof. İrem Erel Göktepe, for their time to evaluate my thesis. I hope they enjoy reviewing my studies as much as I have enjoyed working on it.

There is no way to express my eternal gratitude to my beloved family for unwavering support they have provided all these years for me. I am indefinably thankful to the most amazing mom on earth, Gülcan, for her unconditional love, endless care, devotion and self-sacrifice. I cannot thank my sister, Zeynep, enough for what she has done for me and no words can express how much she means to me. Many thanks to my dad, Ali, for believing in me and listening even minor achievements of mine with great interest. I am honored to be their daughter and making them proud will always be my biggest motivation and ultimate goal. I also want to express my profound appreciation to my grandparents and my aunt Aycan.

I would like to thank Asst. Prof. Seymur Jahangirov and Asst. Prof. Serim Ilday for their advices and support.

Next, I want to thank all the former and current members of DT Lab for any of their contributions. I need to express my gratitude to Dr. Ahmet Koç and

Dr. Rehan Khan for their guidance and expertise on organic synthesis. Many thanks go to Yağmur Keser for helping me to acquire theoretical and practical knowledge on biological applications and her friendly collaboration. She made laboratory work highly enjoyable for me. I was also lucky to work with Duygu Deniz Akolpoğlu even though it was for a short while. I thank Seyed Ehsan Hadi for his expertise and assistance in characterization. I also owe gratitude to Dr. Aisan Khaligh for sharing her experience and Yasaman Sheidaei for her infectious positive energy. I want to express my gratefulness of Bouthaina Aoudi.

I feel so grateful for my best friends Eda Bozkurt and Özge Özsoy always supporting me from thousands of kilometers away and making all those distances meaningless. I will always feel so thankful to have them by my side.

I am greatly indebted to my friends who are always there to cheer me up, support and motivate me in all aspects. I deeply thank Abtin Saateh, Bouthaina Auodi, Joudi Maskoun, Çisil Köksaldı, Gökçe Özkul, Doğu Özyiğit, Kerem Kurban, Hüseyin Can Çamiçi and Şahmurat Kazak for their priceless friendship and unforgettable times we have spent together. I have always appreciated the way they made office a much better place to work.

Also, I gratefully acknowledge the financial support of the Scientific and Technological Research Council of Turkey (TUBITAK) with the grant number 215Z035. I want to thank all the technical and administrative staff of UNAM for making our lives much easier.

Finally, I would like to thank Professor Khuloud Al-Jamal for allowing me to join her group at Institute of Pharmaceutical Science, King's College, London as a visiting scholar during my MSc studies and gain deeper insights and experience on nanomedicine applications. I am glad that I have met with her and her amazing research team. Special thanks go to my supervisor, Dönüş Tuncel, for granting me with this unique opportunity. I am especially thankful to Dr. Julie Tzu-Wen Wang for sharing her experience on in vivo experiments and Dina Omar for her kindness, hospitality, help and making my short stay in the UK more enjoyable.

Thank you all!

Contents

1	Introduction	1
1.1	Supramolecular Chemistry	1
1.1.1	Host-Guest Chemistry	2
1.2	Conjugated Compounds	14
1.2.1	Conjugated Polymers and Oligomers	14
1.2.2	Porphyrins	18
1.3	Supramolecular Constructs Based on Cucurbituril and Conjugated Compounds	19
1.3.1	Rotaxanes and Polyrotaxanes	20
1.4	Cucurbituril-Based Nanomedicine Applications	21
1.4.1	General View and Concepts	21
1.4.2	Drug Delivery	23
1.4.3	Cancer Therapy	24
1.4.4	Development of Antimicrobial Agents	30

2	Experimental	32
2.1	Materials	33
2.2	Instrumentation	34
2.2.1	^1H and ^{13}C Nuclear Magnetic Resonance (NMR) Spectroscopy	34
2.2.2	Electrospray Ionization-Mass Spectrometry (ESI-MS)	34
2.2.3	UV-Visible (UV-Vis) Absorbance Spectroscopy	34
2.2.4	Fluorescence Spectroscopy	35
2.2.5	Fourier-Transform Infrared (FT-IR) Spectroscopy	35
2.2.6	Time-Resolved Fluorescence (TRF) Spectroscopy	35
2.2.7	Dynamic Light Scattering (DLS) and Zeta Potential	35
2.2.8	Scanning Electron Microscopy (SEM)	36
2.2.9	Confocal Laser Scanning Microscopy (CLSM)	36
2.2.10	Isothermal Titration Calorimetry (ITC)	36
2.2.11	Microplate Reader	36
2.2.12	Critical Point Dryer (CPD)	36
2.2.13	Thermal Imaging Camera	37
2.3	Syntheses	37
2.3.1	[5]-Rotaxane	37

2.3.2	CB7-Porphyrin Conjugate (TPP-4CB7) (7)	39
2.3.3	Red-Emitting Conjugated Oligomer Nanoparticles (COL NPs)	40
2.4	Reactive Oxygen Species (ROS) Detection	41
2.5	Determination of Photothermal Conversion Efficiency and Thermal Stability	41
2.6	Isothermal Titration Calorimetry (ITC)	42
2.7	Bacterial Experiments	42
2.7.1	Preparation of <i>E. coli</i> and <i>B. subtilis</i> Suspensions	42
2.7.2	Determination of Minimum Inhibitory Concentration (MIC Assay)	42
2.7.3	Photodynamic Inactivation of Bacteria	43
2.7.4	ζ -Potential Measurements	43
2.7.5	Imaging of Antibacterial Activity by SEM	44
2.7.6	Agar Disk Diffusion Assay	44
2.8	<i>In vitro</i> Experiments	45
2.8.1	Cell culture	45
2.8.2	Cytotoxicity and photo-cytotoxicity	45
2.8.3	Drug Loading	47
2.8.4	Statistical Analysis	48

2.8.5	Preparation of Cell Fixative Solution	48
2.8.6	CLSM Experiments	49
3	Results and Discussions	50
3.1	Introduction	50
3.2	Cucurbituril and Porphyrin-Based Rotaxane	51
3.2.1	Aim of the Study	51
3.2.2	Preparation and Characterization of [5]-rotaxane	52
3.2.3	Evaluation of ROS Generation Performance of (6)	64
3.2.4	Examination of Cytotoxicity and Phototoxicity on <i>E. coli</i> and <i>B. subtilis</i>	66
3.2.5	Examination of Cytotoxicity and Photocytotoxicity on the MCF-7 Cell Line	74
3.3	Supramolecular Cucurbituril-Porphyrin Conjugate	75
3.3.1	Aim of the Study	76
3.3.2	Utilizing (7) as Drug Delivery Vehicle and Combination of Chemotherapy and PDT	77
3.4	Cucurbituril-Capped Conjugated Oligomer-Gold Nanoparticles . .	81
3.4.1	Aim of the Study	82
3.4.2	Preparation of NPs	82
3.4.3	Photophysical and Photothermal Properties of NPs	86

3.4.4	Photothermal Properties of NPs	87
3.4.5	Quantification of Photothermal Conversion Efficiency . . .	89
3.4.6	Photodynamic Effects of NPs on Bacteria	93
3.4.7	Cellular Imaging by NPs	94
3.4.8	Combined PTT/PDT Effect of NPs on Bacteria	96
4	Conclusions and Future Prospective	98

List of Figures

1.1	Molecular chemistry and supramolecular chemistry.	2
1.2	Chemical structures and 3D cartoon representations of important macrocyclic hosts.	4
1.3	Preparation of the first crown ether, dibenzo[18]crown-6.	5
1.4	Chemical structures of (a) α -CD, (b) β -CD, (c) γ -CD, (d) three-dimensional representation of CD, (e) summary of α -CD, β -CD and γ -CD properties.	6
1.5	Condensation of DMB with Lewis acid to yield DMpillar[5]arane.	7
1.6	Structure of Calix[5]arane.	8
1.7	Robert Behrend's method for synthesis and crystallization of cucurbit[6]uril.	9
1.8	Kim's method for the synthesis of CB homologues.	9
1.9	General isolation procedure of CBs.	10
1.10	X-ray crystal structures of CBs (Reprinted with permission from ref.[28] Copyright, 2005 John Wiley & Sons, Ltd.).	11
1.11	Host-guest complexes of CBs.	12

1.12	Common conjugated polymers.	15
1.13	Palladium-catalyzed C-C coupling reactions.	16
1.14	Jablonski energy diagram.	17
1.15	(a) Chemical structure of simplest porphyrin, porphine. (b) UV-vis absorbance spectrum of porphyrins.	18
1.16	Porphyrin synthesis introduced by Rothemund.	19
1.17	Schematic representations of pseudorotaxane, polypseudorotaxane, rotaxane and polyrotaxane.	21
1.18	Morphology of cells after apoptosis, necrosis and autophagy and survival superiority (Reprinted with permission from ref.[102] Copyright, 2017 John Wiley & Sons, Ltd.).	25
1.19	Photothermal cancer therapy.	26
1.20	Activation of photosensitizer to produce ROS giving rise to cell and tissue death.	27
1.21	Type-I reaction (electron or hydrogen transfer) and type-II reaction (energy transfer) in PDT.	28
1.22	PDT in clinical practice.	28
1.23	Pathogen species inactivated by PDT.	30
3.1	Synthetic route for the preparation of TPP-Br.	53
3.2	¹ H-NMR spectrum of (3) (400 MHz, CDCl ₃ , 25 °C).	54
3.3	Synthetic route for the preparation of alkyne-substituted porphyrin.	55

3.4	^1H -NMR spectrum of (4) (400 MHz, CDCl_3 , 25 °C).	56
3.5	^{13}C -NMR spectrum of (4) (CDCl_3 , 25 °C).	57
3.6	+ESI-MS spectrum of (4)	58
3.7	Preparation of (6)	59
3.8	^1H -NMR spectrum of (6) (400 MHz, D_2O , 25 °C).	60
3.9	FT-IR spectrum of (6)	61
3.10	ESI-MS spectrum of (6)	62
3.11	UV-vis absorption and fluorescence spectra of (6) in water at the concentrations of 5, 10 and 20 μM	63
3.12	TRF measurement of (6)	64
3.13	Molecular structures of 2-7 Dichlorofluorescein diacetate (DCFH-DA), 2,7-dichlorofluorescein (DCFH) and the reaction of DCFH with ROS to yield highly fluorescent 2,7-dichlorofluorescein (DCF).	65
3.14	(a) Fluorescence intensity of DCF at 524 nm as blank and in the presence of 5 μM of (6) under continuous white light illumination. I_0 , I_1 , I_2 , I_3 , I_4 correspond to blank and white light irradiated duration for 1, 2, 3, 4 minutes measurements, respectively. (b) Time response curve of DCFH oxidation in the presence of (6) and without (6) ($R^2 = 0.986$ for blank, $R^2=0.9976$ in the presence of (6)).	65
3.15	MIC Assay for (6) : concentrations between 0.5 μM and 4.74 μM in the dark.	67
3.16	MIC Assay for (6) : concentrations between 0.5 μM and 4.74 μM under white light irradiation (22 mW/cm^2).	67

3.17	MIC Assay for (6) : concentrations between 3.37 μM and 3.83 μM under white light irradiation (22 mW/cm^2).	68
3.18	(a), (b) Bacterial killing performance of (6) toward <i>E. coli</i> in the dark and under light exposure. Plate photographs for <i>E. coli</i> on YTD agar plate treated (c) control in the dark, (d) (6) -treated in the dark, (e) control under light exposure (1 min, 22 mW/cm^2) (f) (6) -treated under light exposure (1 min, 22 mW/cm^2).	69
3.19	Plate photographs for <i>E. coli</i> on YTD agar plate treated with 3.5 μM of (5) and non-treated control in the dark (left panel) and under light (right panel).	70
3.20	Biocidal activities of (5) against <i>E. coli</i> in the dark and under white light illumination.	70
3.21	Plate photographs for <i>B. subtilis</i> on YTD agar plate treated with 3.5 μM of (6) and non-treated control in the dark (left panel) and under light (right panel).	71
3.22	Biocidal activities of (6) against <i>B. subtilis</i> in the dark and under white light illumination.	72
3.23	SEM images of <i>E. coli</i> (a) control in the dark, (b) 3.5 μM of (6) -treated in the dark, (c) control under photoirradiation (d) 3.5 μM of (6) -treated under photoirradiation.	73
3.24	ζ -Potentials of <i>E. coli</i> incubated with 3.5 μM of (6) in water at 25.0 $^\circ\text{C}$ in the dark and under light.	74
3.25	Relative cell viability for MCF-7 incubated with 2-100 μM of (6) upon normalization with DMEM control group (a) in dark (P=0.0653) and (b) upon white light irradiation (10 min, 20 mW/cm^2) (P<0,0001).	75

3.26 Synthetic route for the preparation of (7)	77
3.27 Isothermal Titration Calorimetry (ITC) data for the complexation of (2) and DOX.	79
3.28 <i>In vitro</i> relative cell viability (%) after treatment with various concentrations of (7) , DOX and (7) +DOX (a) in dark, (b) upon white light irradiation (5 min, 20 mW/cm ²).	81
3.29 Schematic route to prepare (8)	83
3.30 A schematic view for the synthesis of (a) conjugated oligomer nanoparticles (COL-NP) (9) , (b) conjugated oligomer-gold nanoparticles (COL-Au-NP) (10) , and complexation of amine residues of NPs with CB7, (c) CB7@COL-NP (11) , (d) CB7@COL-Au-NP (12)	84
3.31 DLS histograms of (a) (9) , (b) (11) , (c) (10) , (d) (12)	85
3.32 UV-vis-NIR absorbance spectrum of (9) and (10) in Milli-Q water.	86
3.33 Photothermal response of NPs.	88
3.34 Time vs $-\ln(\theta)$ graph for the quantification of photothermal conversion efficiency of (10)	92
3.35 Semi-solid agar plate and corresponding SEM pictures for <i>E. coli</i> treated with 12.4 $\mu\text{g}/\text{mL}$ of NPs in the dark and under light.	93
3.36 (a) Mean <i>E. coli</i> \log_{10} CFU reduction upon NP-treatment in the dark and under light, (b) ζ -potential measurements of NP-treated <i>E. coli</i> and <i>B. subtilis</i>	94
3.37 DIC and CLSM images of (10) -treated and non-treated MCF-7 cells with and without light.	95

3.38 CLSM images of MCF-7 nuclei stained with DAPI (blue) and treated with (12) (merged).	96
3.39 Plate photographs of agar disc diffusion assays of <i>E. coli</i> and <i>B. subtilis</i> treated with 12.4 $\mu\text{g}/\text{mL}$ of ampicillin, (9) , (10) , (11) and (12) in the dark and satisfying PDT, PTT and PDT+PTT conditions.	97
3.40 Inhibition zone graphs of <i>E. coli</i> and <i>B. subtilis</i> for the plates in Figure 3.39.	97

List of Tables

1.1	Structural parameters of common CB homologues and inverted CBs (M_w = molecular weight, a=portal diameter, b=cavity diameter, c=height, d=outer diameter, V=cavity volume).	11
2.1	Concentrations used MTT assay for [5]-rotaxane in the dark. . . .	46
2.2	Concentrations used MTT assay for [5]-rotaxane under light. . . .	47
2.3	Concentrations used MTT assay for nanoparticles in the dark and under light.	47
2.4	Concentrations used MTT assay for TPP-4CB7 and DOX in the dark and under light.	48
3.1	Z-average size, PDI and zeta potential of (9) , (10) , (11) and (12)	86
3.2	The fluorescence lifetime and quantum yield of (8) , (9) and (10)	87

List of Abbreviations

<i>B. subtilis</i>	Bacillus subtilis
BBr ₃	Boron tribromide
CB	Cucurbituril
CD	Cyclodextrin
CFU	Colony forming units
CLSM	Confocal laser scanning microscopy
CONs	Conjugated oligomer nanoparticles
CPNs	Conjugated polymer nanoparticles
CPD	Critical point drying
DAPI	4',6-diamidino-2-phenylindole
DCM	Dichloromethane
DCFH	2,7-dichlorofluorescein
DDQ	2,3- dicholoro-5,6-dicyano-1,4-benzoquinone
DIC	Differential interface contrast
DLS	Dynamic light scattering
DMEM	Dulbecco's modified eagle medium
DMSO	Dimethyl sulfoxide
DOX	Doxorubicin hydrochloride
<i>E. coli</i>	Escherichia coli
ESI-MS	Electrospray ionization mass spectrometry
EtOH	Ethanol
FT-IR	Fourier transfer infrared spectroscopy

HOMO	Highest occupied molecular orbital
ITC	Isothermal titration calorimetry
LB	Luria-Bertani medium
LUMO	Lowest unoccupied molecular orbital
MIC	Minimum inhibitory concentration
MTT	Methyl thiazolyl tetrazolium
NIR	Near infrared
NMR	Nuclear magnetic resonance
NPs	Nanoparticles
OD₆₀₀	Optical density at 600 nm
PBS	Phosphate-buffered saline
PDT	Photodynamic therapy
PL	Photoluminescence
PS	Photosensitizer
PTT	Photothermal therapy
ROS	Reactive oxygen species
RT	Room temperature
SEM	Scanning electron microscopy
TCBQ	Tetrachloro- <i>p</i> -benzoquinone
THF	Tetrahydrofuran
TLC	Thin layer chromatography
TPP	Tetraphenylporphyrin
UV-vis	Ultraviolet-visible
¹ O ₂	Singlet oxygen
³ O ₂	Triplet oxygen
λ	Wavelength

List of Compound Names and Notations

- (1) Cucurbit[6]uril (CB6)
- (2) Cucurbit[7]uril (CB7)
- (3) 5,10,15,20-tetrakis(α -bromo-p-tolyl)porphyrin (TPP-Br)
- (4) Prop-2-ynyl-4-[10,15,20-tris-(4-prop-2-ynylaminomethyl-phenyl)-porphyrin-5-yl]-benzyl-amine (Propargylated porphyrin)
- (5) Protonated propargylated porphyrin
- (6) [5]-rotaxane
- (7) Porphyrin-CB7 Conjugate (TPP-4CB7)
- (8) 3,3',3'',3'''-[(1E,1'E)-2,1,3-Benzothiadiazole-4,7-diylbis(ethene-2,1-diyl)]-bis(9H-fluorene-9,9,2-triyl)-tetrakis(N,N-dimethylpropan-1-amine) (Red-emitting conjugated oligomer (COL))
- (9) Dispersed conjugated oligomer nanoparticles in water (COL-NP)
- (10) Hybrid core-shell nanoparticles based on conjugated oligomer and gold (COL-Au-NP)
- (11) Cucurbit[7]uril-capped dispersed conjugated oligomer nanoparticles in water (CB7@COL-NP)
- (12) Cucurbit[7]uril-capped hybrid core-shell nanoparticles based on conjugated oligomer and gold (CB7@COL-Au-NP)

Chapter 1

Introduction

1.1 Supramolecular Chemistry

Supramolecular chemistry is the chemistry field specialized in noncovalent intermolecular interactions. Jean-Marie Lehn mentioned the term “supramolecular chemistry” regarding macropolycyclic inclusion complexes [1] in 1978 and later described supramolecular chemistry as “chemistry beyond the molecule” [2] in 1988. Donald J. Cram, Jean-Marie Lehn and Charles J. Pedersen were awarded the Nobel Prize in chemistry in 1987 for their development and use of molecules with structure-specific interactions of high selectivity.

While molecular chemistry investigates the formation of individual molecules from molecular precursors or constituent atoms, supramolecular chemistry investigates the formation of organized molecular building blocks in mesoscale regime (Figure 1.1). Supramolecular constructs form through weak and reversible noncovalent forces between molecules such as hydrogen bonds, hydrophobic forces, van der Waals forces, metal–ligand coordination, π - π interactions, charge transfer interactions and electrostatic interactions. This formation can be via host-guest complexation, lattice inclusion (clathrate compounds) or molecular self-assembly (micelles, vesicles, liposomes, membranes, dendrimers, liquid crystals etc.). Even

though noncovalent interactions are remarkably weak (1-350 kJ/mol) in comparison to covalent bonds (150-1075 kJ/mol), multiple noncovalent interactions can result in the construction of a stable supramolecular system. [3] Supramolecular smart materials are able to adapt to their environment and have appealing properties like degradability, self-healing and shape-memory, stimuli-responsiveness. [4]

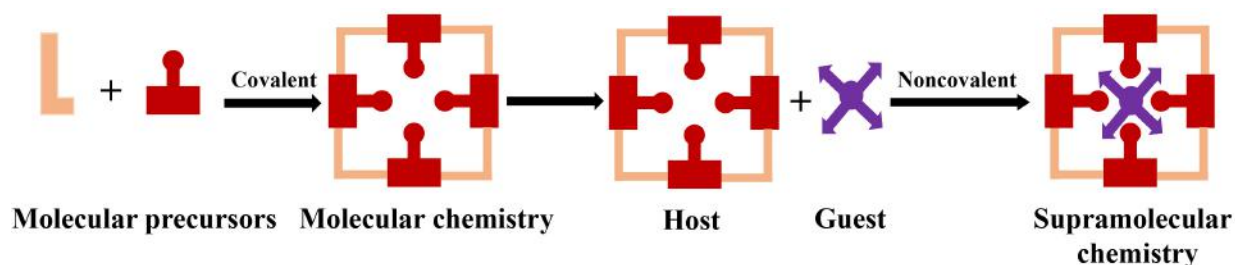


Figure 1.1: Molecular chemistry and supramolecular chemistry.

Supramolecular chemistry has been extensively studied as an interdisciplinary research field covering the concepts of molecular self-assembly, host-guest chemistry (drug delivery) molecular recognition (molecular sensors, catalysis), logic gates, molecular machinery, biomimetic systems (artificial enzymes, protein design, self-replication) and imprinting.

1.1.1 Host-Guest Chemistry

Host-guest chemistry is one of the defining branches of supramolecular chemistry based on the construction of unique complexation of two or more molecules or ions via noncovalent interactions. Resulting complexes with large supramolecular host molecules (e.g. macrocycles, cages, capsules) and smaller guest molecules own superior physicochemical characteristics superior to that of guest.

Deep understanding of binding and encapsulation properties of supramolecular hosts are essential for rational design of supramolecular systems towards targeted applications. High selectivity and binding affinity of hosts to ligands are desirable to form stable complexes. Therefore, thermodynamics of host-guest interaction

and structural parameters of host and guest molecules govern the complexation. To gain better insights, as a key concept, selectivity should be understood well by defining cooperativity, complementarity and preorganization terms, since the rational design of selective receptor is based on complementarity of host-guest interaction sites, preorganization and assigning suitable noncovalent interaction.

Cooperativity was basically defined considering enzyme-substrate interaction referring substrate binding sites in allosteric enzymes. [5] From the thermodynamic aspect, it is explained by considering free energy change (ΔG°). In multistep interactions or binding events, ΔG° in subsequent steps (in comparison with the first step) is either decreasing (implying + cooperativity) or increasing (- cooperativity) where $\Delta G^\circ = \Delta H^\circ - T\Delta S^\circ$. Here, ΔH° is enthalpy change, T is temperature and ΔS° is entropy change. [6]

Structural and chemical complementarity between binding sites of host and guest molecules is meant by complementarity. Binding sites of host should be able to contact, attract the binding sites of guest without disturbance and undergo conformational change to yield the most proper steric fit with the guest. [7]

Preorganization is another important condition for the formation of stable host-guest complexes. Prior to complexation, host and guest molecules are highly organized to minimize conformational change for binding. [8]

High selectivity is the most significant goal of supramolecular chemistry. Selectivity of host towards specific guest is sensing/recognition ability of host for that target guest by rejecting other guests in the media. Selective performance of host is determined thermodynamically and kinetically. The host-guest system with stronger binding constant will yield higher stability of complex.

1.1.1.1 Important Macrocyclic Hosts in Host-Guest Chemistry

Macrocyclic host molecules including crown ethers, cyclodextrins, pillararenes, calixarenes, cryptands, resorcinarenes, blue box and cucurbiturils are essential

building blocks to construct host-guest interaction based supramolecular platforms. These hosts can bind neutral or charged guest molecules with specific binding affinity and selectivity. Macrocyclic-based supramolecular polymers can be prepared in solution, in gel or in solid phase and exhibit high responsiveness to external stimuli covering pH change, temperature, photoirradiation, mechanical force etc. enabling to design smart materials for different applications. [9]

In the following subsections, crown ethers, cyclodextrins, pillararenes, calixarenes are briefly introduced. This thesis focuses on cucurbituril-based supramolecular constructs and therefore cucurbiturils are introduced more in detail than other macrocyclic compounds. In Figure 1.2, chemical structures and 3D representations of these macrocycles are illustrated.

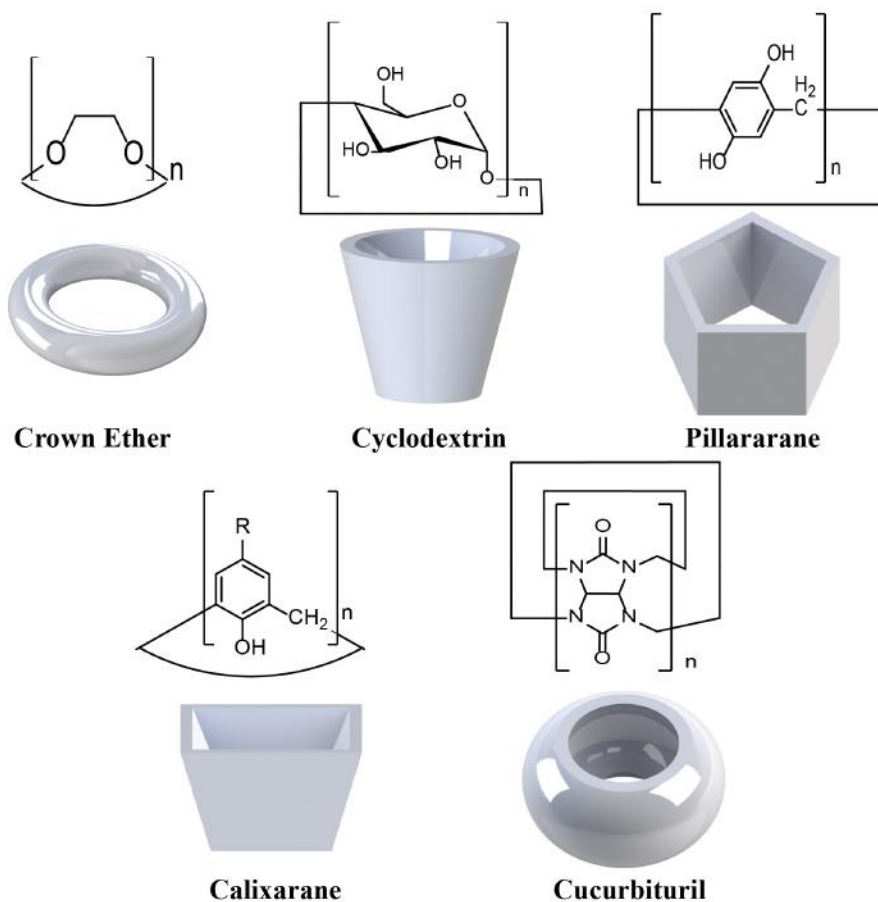


Figure 1.2: Chemical structures and 3D cartoon representations of important macrocyclic hosts.

1.1.1.1.1 Crown Ethers

Crown ethers are macrocycles based on repeating $-\text{OCH}_2\text{CH}_2-$ units derived from ethylene glycol ($\text{HOCH}_2\text{CH}_2\text{OH}$) and they possess cavity and medium polarity. Their structures resemble crown and crown ethers have high binding affinities towards metallic and organic cations. In 1967, Charles Pedersen attempted to prepare complexing agent for divalent cations and as a side product the first crown ether (dibenzo[18]crown-6) was incidentally synthesized (Figure 1.3). [10] He proceeded to synthesize and work on their binding properties and then he was co-awarded the Nobel Prize in chemistry in 1987.

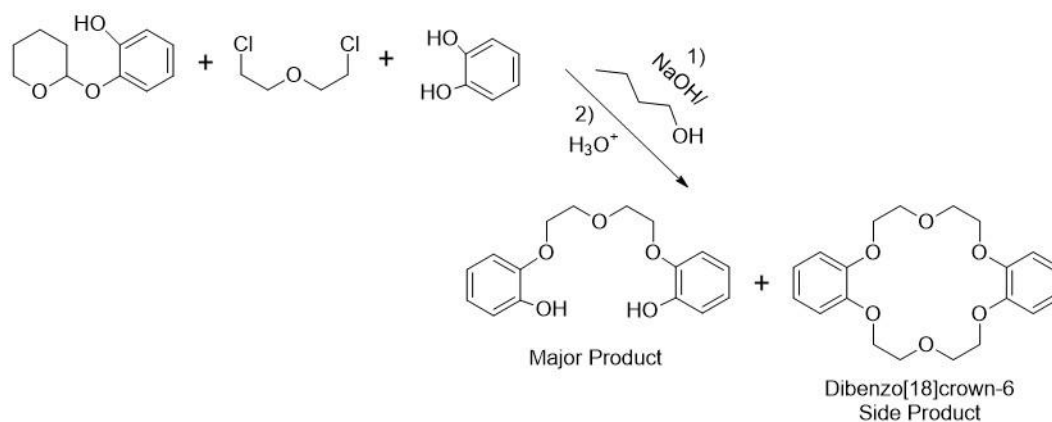


Figure 1.3: Preparation of the first crown ether, dibenzo[18]crown-6.

1.1.1.1.2 Cyclodextrins

Cyclodextrins (CD) are crystalline non-reducing oligosaccharides made up of D-glucopyranoside subunits linked by α -1,4 bonds. Number of glucose subunits (n) determines the nomenclature of CDs, n=6 refers to α -CD, 7 to β -CD and 8 to γ -CD, as given in Figure 1.4 a, b and c. They are obtained from enzymatic conversion of starch. [11]

CDs own toroidal structure with the large and the small openings (Figure 1.4 d). Small opening of the toroid is exposed to secondary hydroxyl groups of

solvent while large one is exposed to primary hydroxyl groups. As a result of this structure, central cavity is lipophilic and considerably less hydrophilic than the aqueous environment enabling the accommodation of hydrophobic guests. On the contrary, the outer surface is hydrophilic due to hydroxyl groups which makes CDs water soluble macrocycles. Properties of α -CD, β -CD and γ -CD are compiled in the table (Figure 1.4 e). [12], [13] By virtue of their good water solubility, they can form water soluble and stable complexes.

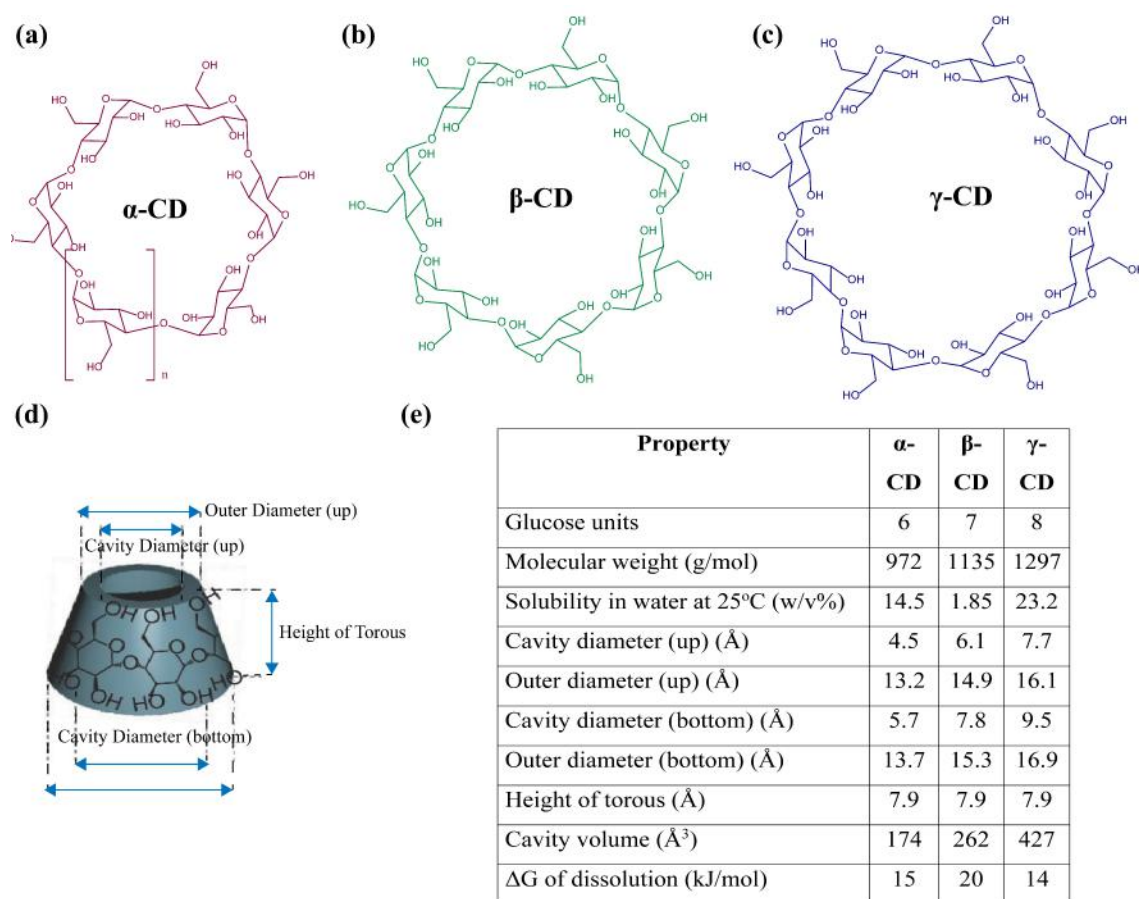


Figure 1.4: Chemical structures of (a) α -CD, (b) β -CD, (c) γ -CD, (d) three-dimensional representation of CD, (e) summary of α -CD, β -CD and γ -CD properties.

CDs and their derivatives are desirable for a wide range of applications spanning pharmaceutical formulations, nanomedicine (drug delivery vehicles), food and cosmetic industries, catalysis, chromatography, textile production etc. [14]

1.1.1.1.3 Pillararenes

Pillararenes are relatively new family of macrocycles composed of hydroquinone units connected through methylene bridges at *para* positions. In 2008, Ogoshi *et al.* have coined the word “pillar[5]arane” for the product of condensation reaction of 1,4-dimethoxybenzene (DMB) with paraformaldehyde in the presence of Lewis acid (Figure 1.5). They have also shown that, pillar[5]arane formed 1:1 host–guest complexes with dialkyl viologen and alkyl pyridinium derivatives. [15]

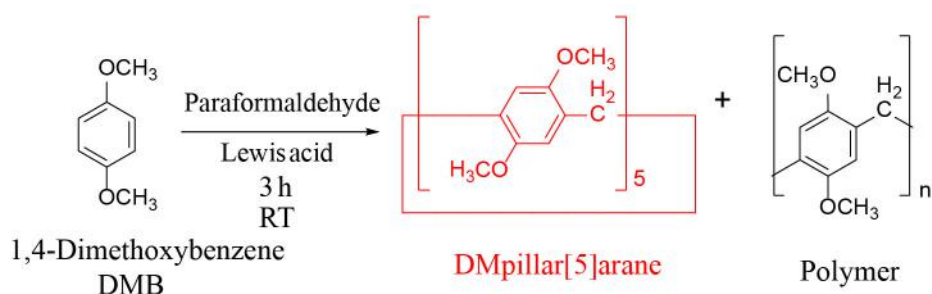


Figure 1.5: Condensation of DMB with Lewis acid to yield DMpillar[5]arane.

Pillararenes have symmetrical and rigid structures with electron-donating cavities. Versatile functionalization facilitates to be utilized in diverse applications as artificial molecular machines, [16] fluorescent sensors, [17] selective artificial transmembrane channels, [18], drug delivery systems [19] etc.

1.1.1.1.4 Calixarenes

Calixarenes are macrocycles obtained from condensation reactions of *para*-tert-butylphenol and formaldehyde. [20] Calixarenes with different ring sizes are prepared in high yield by adjusting reaction conditions (base, temperature and time). In Figure 1.6, structure of Calix[5]arane is given. Calix refers to chalice, vase in Greek describing the molecular structures of calixarenes and three-dimensional structures of calixarenes leads to hydrophobic cavities. In the literature, they

were utilized to develop fluorescent sensors, anion receptors, multivalent ligands, supramolecular nanoconstructs and polymers. [21]

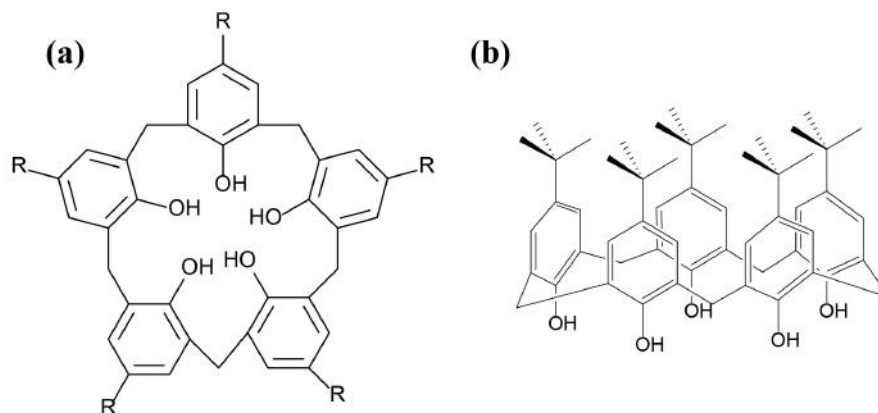


Figure 1.6: Structure of Calix[5]arane.

1.1.1.1.5 Cucurbiturils

Cucurbiturils (CBs) are robust symmetrical macrocycles obtained from acid-catalyzed condensation of glycoluril and formaldehyde firstly published by Robert Behrend in 1905. [22] Now, it corresponds to cucurbit[6]uril (CB6) implying 6 glycoluril units in the macrocycle with two hydrophilic portals containing hydrophobic cavity and carbonyls. Product was named cucurbituril due to structural resemblance to pumpkin under cucurbitaceae botanic family. In 2000, Kim *et al.* reported the new CB homologues: CB5, CB7 and CB8. [23] In 2001, Day *et al.* optimized the reaction conditions to achieve higher yield and proposed mechanism for the formation of CB5 to CB10. [24] After one year, they also presented CB10 interlocked with CB5. [25] These discoveries enabled preparation of different CB homologues and derivatives enlightening and improving the applicability of CBs.

1.1.1.1.5.1 Synthesis and Isolation of CBs

CB6 was the first discovered homologue of CBs. Synthetic route contains two steps as shown in Figure 1.7 In the first step, glycoluril and excess formaldehyde were treated with dilute hydrochloric acid and precipitate forms. In the second step, this precipitate was dissolved in concentrated H_2SO_4 at $110\text{ }^\circ\text{C}$ followed by water dilution to yield CB6. [22]

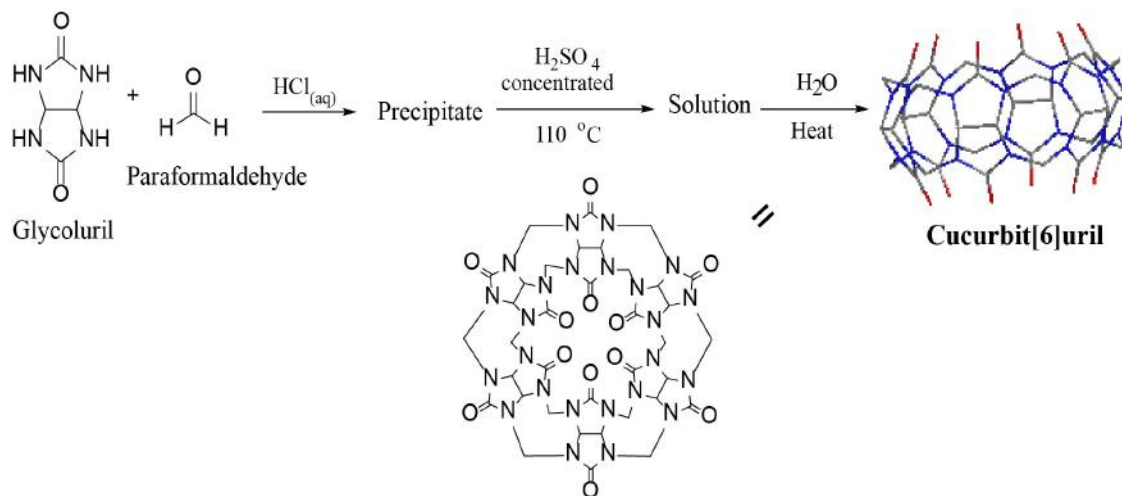


Figure 1.7: Robert Behrend's method for synthesis and crystallization of cucurbit[6]uril.

Kim *et al.* modified the reaction conditions [23] of Behrend's method to obtain the mixture of isolable CB5, CB6, CB7, CB8 and CB10 homologues (Figure 1.8).

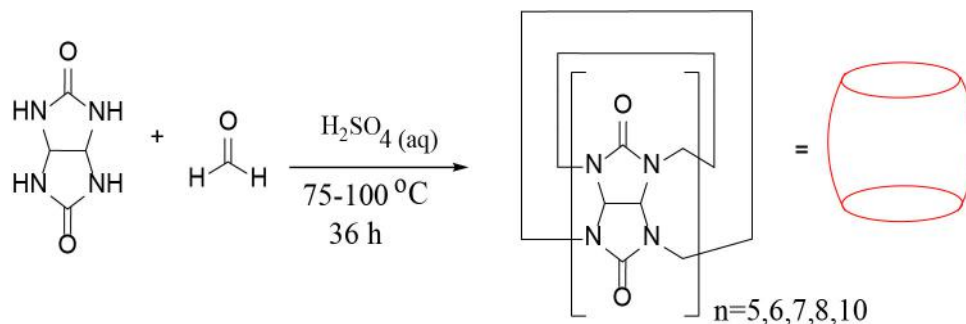


Figure 1.8: Kim's method for the synthesis of CB homologues.

Different methods were proposed to synthesize CBs based on Kim's [23], Day's [24] and Isaacs'[26] method. In general, glycoluril, formaldehyde or paraformaldehyde solution in water, and 5 M of HCl or H_2SO_4 are mixed and heated to 80–100

°C for 36 h. Solvent is evaporated and remained mixture is consecutively precipitated in water and methanol to yield mixture of CB5, CB6 (major product), CB7, CB8 and traces of CB10, iCB6, CB5@CB10 and other oligomers. Isolation of each of them relies on solubility difference in water, water/methanol and diluted hydrochloric acid solutions as shown in Figure 1.9. [27] To isolate CB7, which is the most water soluble one among other CB homologues, from the mixture of CBs, hot 20% aqueous solution of glycerol to extract is used.

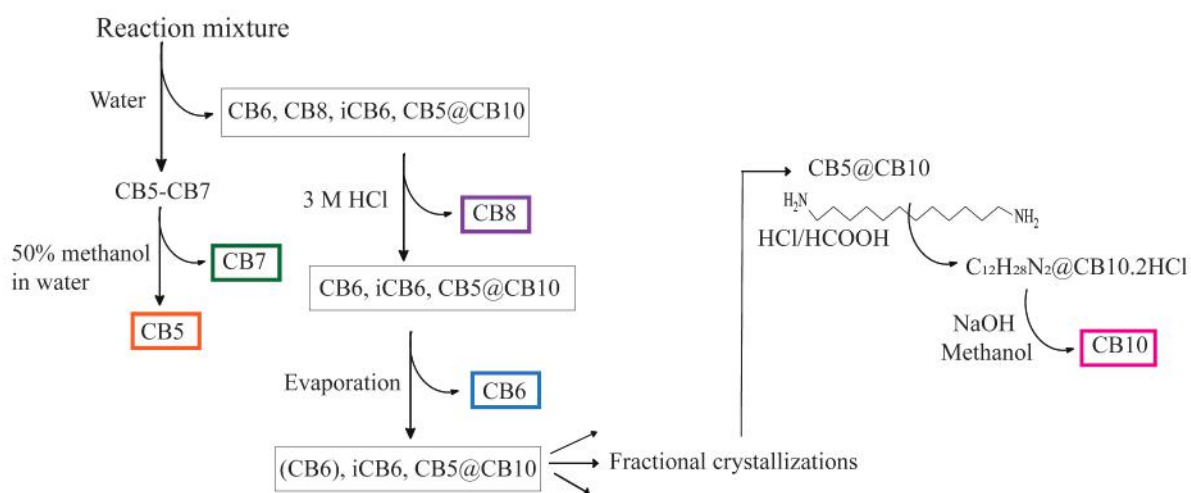


Figure 1.9: General isolation procedure of CBs.

Functionalization of CBs has been extensively studied for enhancing their solubility, stability or rendering them more suitable for the target applications. It is possible to design and prepare them using different strategies to bear different substituents on different regions of the molecule.

1.1.1.1.5.2 Structural and Physical Properties of CBs

CBs possess rigid and symmetrical structures verified by X-ray crystallography whereas larger homologues (CB10, CB13, CB14 and CB15) are flexible. X-ray crystal structures of common CB homologues are demonstrated in Figure 1.10. [28] These crystal structures reveal the structural parameters of CBs such as portal diameter, outer diameter, cavity diameter, cavity volume and height.

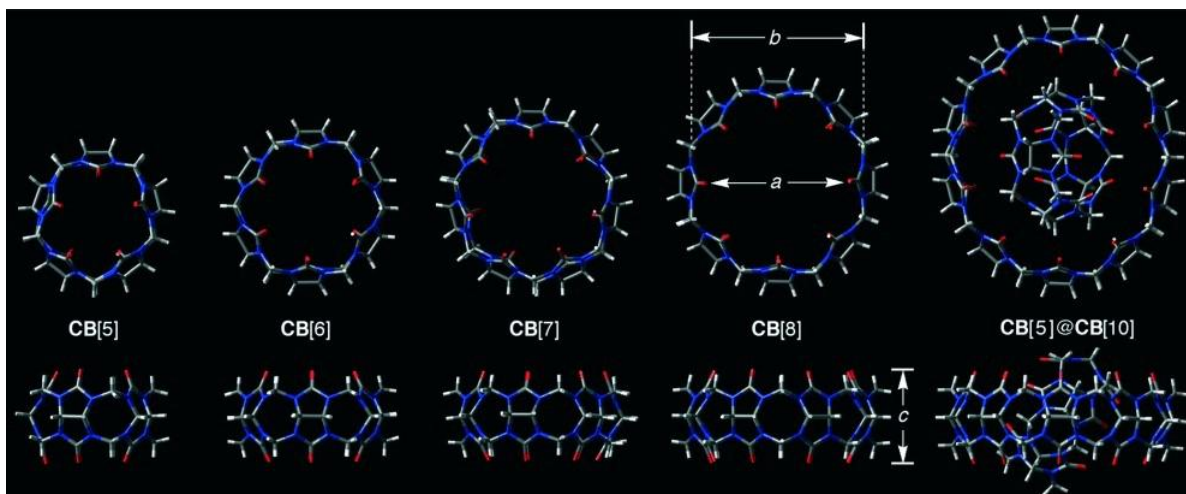


Figure 1.10: X-ray crystal structures of CBs (Reprinted with permission from ref.[28] Copyright, 2005 John Wiley & Sons, Ltd.).

Structural parameters of common uncomplexed CB homologues [23] and inverted CBs [29] are compiled in table 1.1

CB	M_w (g/mol)	a (Å)	b (Å)	c (Å)	d (Å)	V (Å ³)
CB5	830	2.4	4.4	9.1	13.1	82
CB6	996	3.9	5.8	9.1	14.4	164
CB7	1163	5.4	7.3	9.1	16.0	279
CB8	1329	6.9	8.8	9.1	17.5	479
CB10	1161	9.5-10.6	11.3-12.4	9.1	20.0	870
iCB6	996	4.3-3.9	3.8-5.8	9.1	10.7-14.4	-
iCB7	1163	6.7-5.4	5.4-7.3	9.1	11.2-16.0	-

Table 1.1: Structural parameters of common CB homologues and inverted CBs (M_w = molecular weight, a=portal diameter, b=cavity diameter, c=height, d=outer diameter, V=cavity volume).

CBs suffer from low water solubility compared to other macrocycles like cyclodextrins. CB5 and CB7 (odd numbers) have higher water solubility (\sim 20-30 mM) than that of CB6 and CB8 (0.018 mM and $<$ 0.01 mM respectively) since molecule-water interactions dominate molecule-molecule interactions. [30], [31] However, solubilities of CB6 and CB8 are considerably enhanced upon acid addition.

1.1.1.1.5.3 Thermodynamics of CB-Guest Binding

CBs are able to encapsulate wide range of guests inside their hydrophobic cavities. Via hydrophobic and electrostatic interactions, they bind to guest molecules with high binding affinities in aqueous media. Portals are considered as binding sites for cationic guest molecules and resulting complex is stabilized through ion-dipole interactions whereas outer surface are for large anionic guests. Host-guest complexes can form in several ways as shown in Figure 1.11.[32] Host-guest interaction and complexation mechanism can experimentally be investigated by absorbance, fluorescence ^1H -Nuclear Magnetic Resonance (NMR) spectroscopies and isothermal titration calorimetry (ITC). These methods can provide thermodynamic parameters such as binding affinity (K_a), binding stoichiometry (n) and enthalpy changes (ΔH). From these, Gibbs free energy changes (ΔG) and entropy changes (ΔS) can be calculated using the relation $\Delta G = -RT \ln K_a = \Delta H - T \Delta S$ where R stands for gas constant and T absolute temperature.

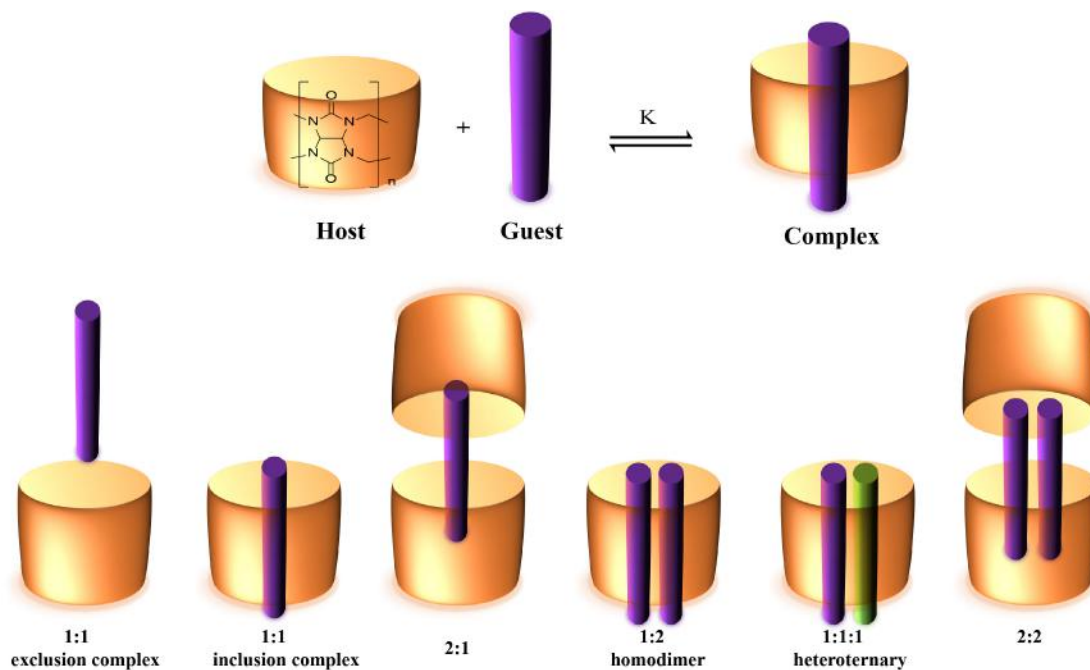


Figure 1.11: Host-guest complexes of CBs.

Ion-dipole interactions, hydrophobic interactions and host-guest packing coefficients are important parameters for complexation with high binding affinity. Hydrophobic interactions imply the interaction between guest and solvent molecules, cavitation energy and release of high-energy water from cavities. These supply driving force for host-guest complexation. [33],[34],[35]

Understanding thermodynamic aspects is essential for rational design of complexes with guests owning high binding affinities for CB receptors. Desirable binding properties enable CBs to be tailored towards target applications such as drug delivery, nanomedicine, sensing, catalysis etc.

1.1.1.1.5.4 CB-Based Molecular Recognition

Thermodynamics and kinetics of host-guest complexation by CBs have been widely investigated to demonstrate their specific binding properties for identification and characterization of suitable guests. Scherman *et al.* have reviewed specific binding properties of CBs and association constants of 412 different guests including organic molecules, gases and homodimers forming inclusion or exclusion complexes with CB homologues. [32] Owing to their rigid structure, hydrophobic inner cavities and ability to form dynamic self-assemblies, CB complexes are found to be extremely strong and stable in water. [36] By this time, there have been numbers of articles in which CBs have been integrated into various materials including polymers, [37] fullerenes, [38] nanosheets, [39] vesicles, [40] 2D films, [41] dendrimers, [42] hydrogels, [43] metal nanoparticles, [44] and so on to have unique recognition features. Contribution of CBs to self-assembled structures and nanomaterial engineering has been gaining keen attention. Herein, complexation of CBs with guest molecules only related to nanomedicine applications is focused and compiled in table A1 (Appendix).

1.2 Conjugated Compounds

As a term, “conjugated” was primarily used by German chemist Johannes Thiele for the compounds possessing alternating single and multiple bonds. Overlapping p-orbitals leads to system of delocalized π -electrons throughout the molecule resulting in lowering overall energy of the molecule and therefore enhancing stability. The examples conjugated systems are included in graphene, graphite, carbon nanotubes, conductive polymers, porphyrins and phthalocyanines.

1.2.1 Conjugated Polymers and Oligomers

π -conjugated polymers and oligomers own backbone with delocalized electrons and therefore their electrical conductivity is enhanced by electrochemical doping. [45] In contrast to conventional insulator polymers and oligomers, conjugated ones are conductive or semi-conductive owing to those delocalized electrons. Since they possess appealing electrical and optical properties, research efforts were directed towards conjugated compounds to utilize them in many application areas such as electronics, biomedicine, solar cells, chemical sensing, nanophotonics etc. In Figure 1.12, structures of some common conjugated polymers are given.

Conjugated polymers and oligomers can be synthesized with cross-coupling reactions including Suzuki-Miyaura coupling and Stille coupling. Suzuki-Miyaura and Stille coupling reactions are based on metal catalyzed (generally palladium-catalyzed) cross-coupling reaction to obtain conjugated systems of alkenes, alkynes, styrenes etc. Pd-catalyzed C-C coupling reactions are given in Figure 1.13.

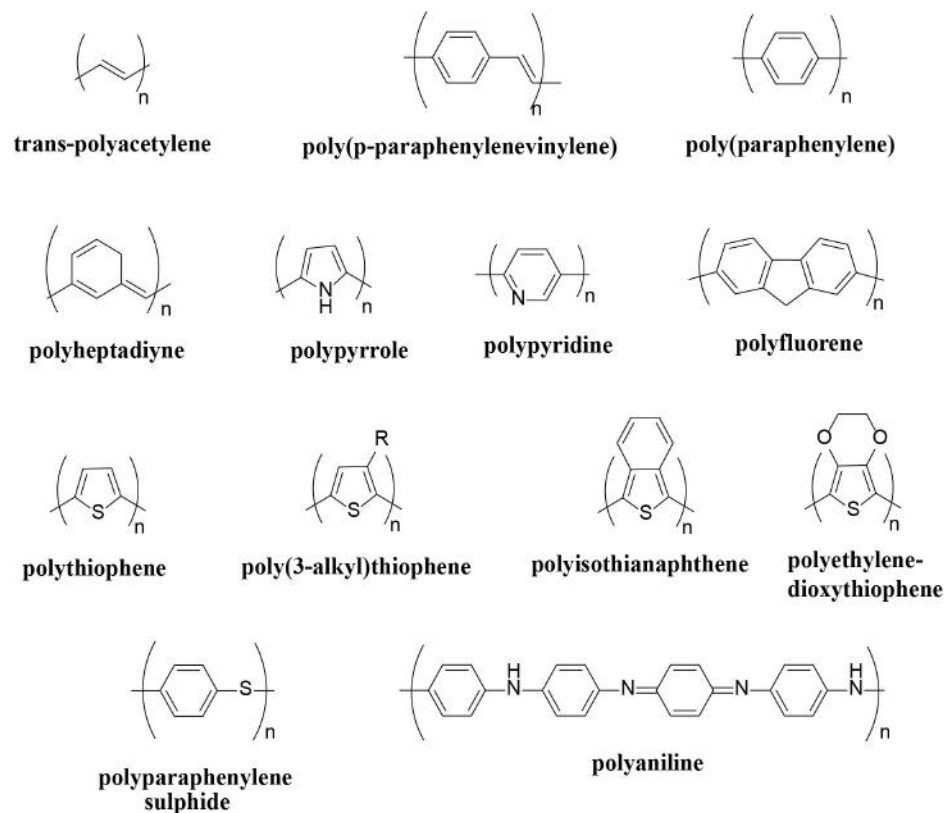


Figure 1.12: Common conjugated polymers.

1.2.1.1 Photoluminescence of Conjugated Polymers and Oligomers

Photoluminescence (PL), a general name of fluorescence and phosphorescence, describes the light emission from materials after absorbing photons. Owing to delocalized π -electrons, majority of conjugated polymers are colored and display interesting photophysical properties covering PL, photoconductivity etc.

Under light irradiation with sufficient energy, π -electrons of conjugated oligomers are excited from highest occupied molecular orbital (HOMO or ground state) to next available energy state called lowest unoccupied molecular orbital (LUMO). Due to extreme instability of LUMO state, excited electrons go back to stable HOMO state by either fluorescence or phosphorescence. Jablonski energy diagram given in Figure 1.14 explains those phenomena schematically.

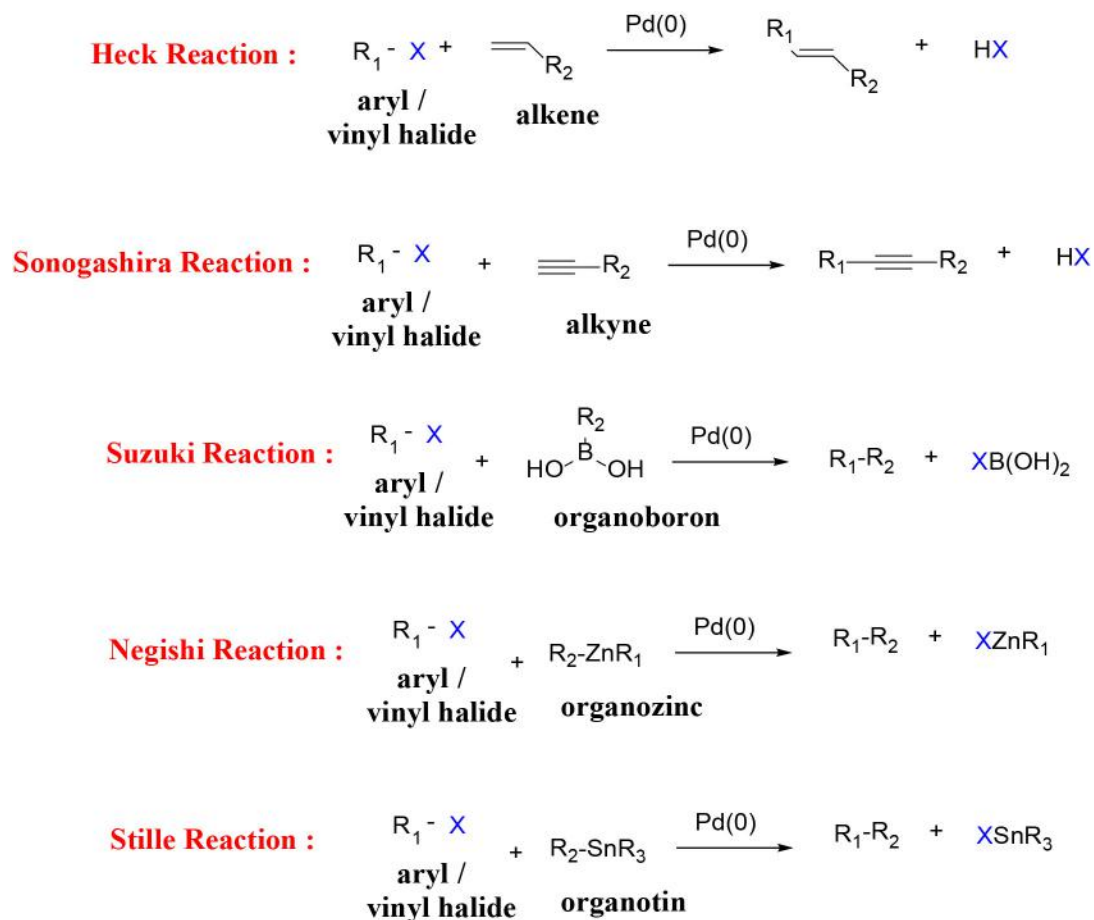


Figure 1.13: Palladium-catalyzed C-C coupling reactions.

Energy difference between HOMO and LUMO states is referred as band gap and it determines the optical and electrical properties of conjugated polymers. Since the band gap of conjugated polymers can be tuned, their optical and electronic properties are tunable rendering them quite appealing in multiple application areas.

1.2.1.2 Conjugated Polymer and Oligomer Nanoparticles

Nanoparticles based on conjugated polymers (CPNs) have been gaining keen attention having combined features of nanoparticles and conjugated polymers/oligomers such as high fluorescent quantum yield & molar absorptivity,

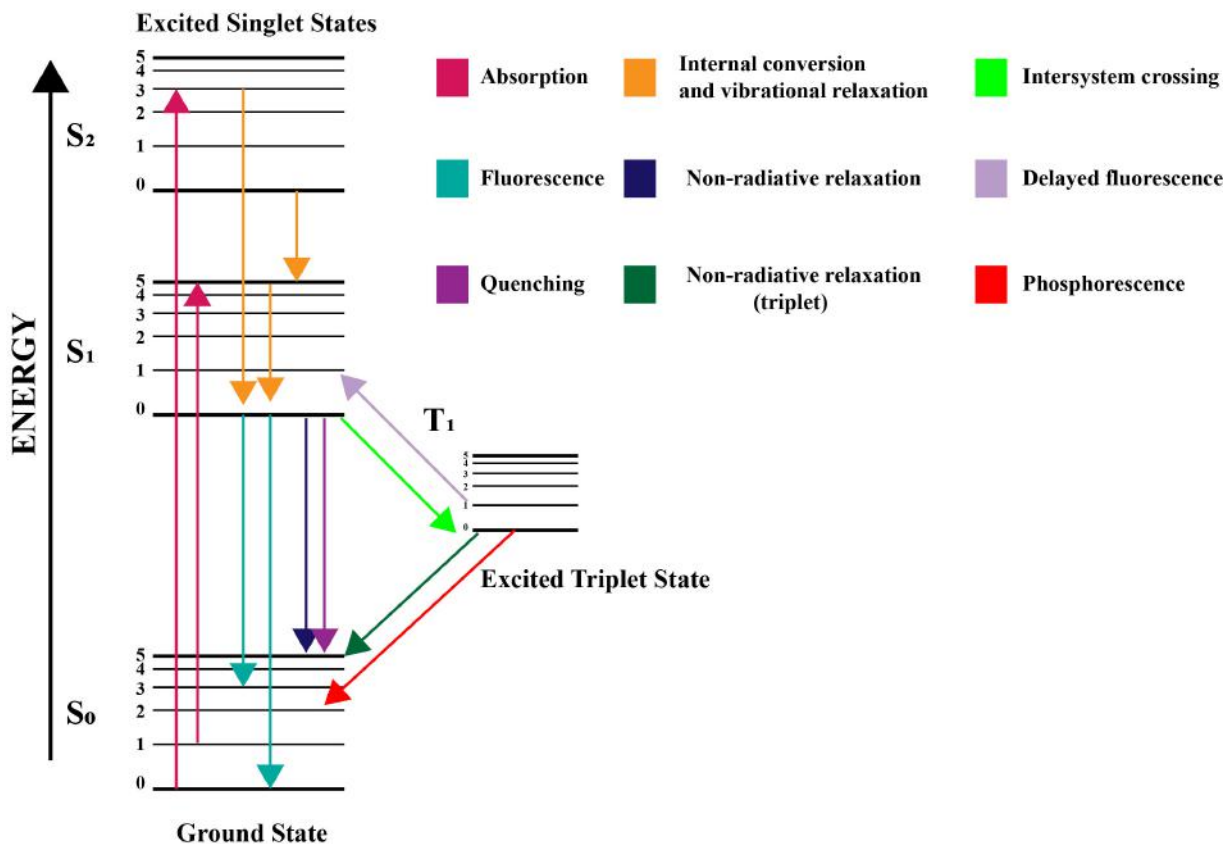


Figure 1.14: Jablonski energy diagram.

facile synthesis & functionalization, tunable properties, low cost and light-harvesting capabilities. Rational design of self-assembled conjugated oligomer-based nanoparticles (CONs) is also promising since they present extra advantages over CPNs such as having well-defined molecular weight and relatively smaller size which enables enhanced cell penetration, permeability and excretion ability for biological applications. CONs possess higher fluorescent quantum yield than CPNs and comparable stabilities and molar absorptivities with CPNs. [46], [47] Preparation methods of CPNs and CONs encompassing reprecipitation, mini-emulsion, pulsed-laser ablation and direct condensation of organic vapour are key to determine size and shape of nanoparticles. [48]

1.2.2 Porphyrins

Porphyrins are naturally existing macrocycles playing vital role in the metabolism of living organisms for example chemical structures of hemoglobin, protein of red blood cells, and chlorophyll, photosynthetic pigment, are based on porphyrin derivatives. Porphyrins are conjugated systems composed of four pyrrolic subunits connected via methine bridges (=CH-) at their α carbons. As given in Figure 1.15, they have 26 π -electrons in total but 18 of them forms continuous planar structured cycle making the compound aromatic. They appear intense purple as a result of owning strong absorption bands in the visible region of electromagnetic spectrum. Intense absorption peak around 405 nm is referred as Soret band and four relatively weak peaks between 500-630 nm are called Q-bands. Owing to that strong absorption of light, porphyrins are utilized in photodynamic therapy which will be introduced under section 1.4.3.

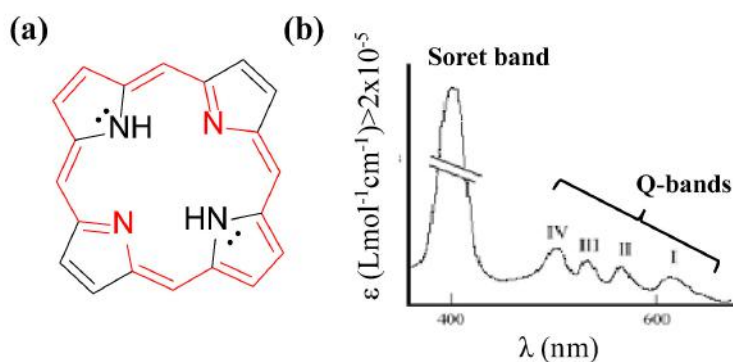


Figure 1.15: (a) Chemical structure of simplest porphyrin, porphine. (b) UV-vis absorbance spectrum of porphyrins.

1.2.2.1 Synthesis of Porphyrins

First description of porphyrin synthesis was introduced by Paul Rothmund in 1935 based on high temperature condensation of benzaldehyde and pyrrole in pyridine (Figure 1.16). [49]

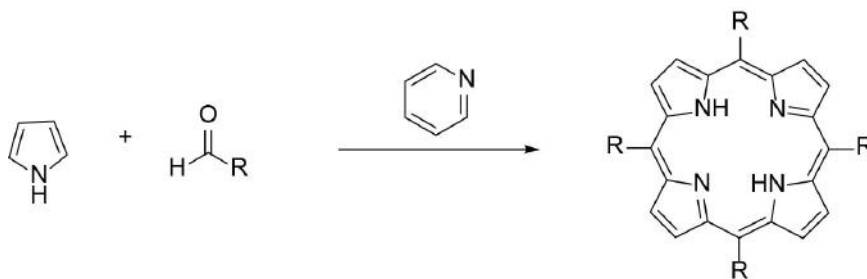


Figure 1.16: Porphyrin synthesis introduced by Rothemund.

Later on, Adler developed Rothemund's procedure in which benzaldehyde and pyrrole was refluxed in the presence of carboxylic acids functioning as solvent. [50] However, Adler's procedure was not suitable for aldehydes which have acid sensitive functional groups. [51],[52] For dealing with this problem, Lindsey reported an updated method. In this updated method, firstly porphyrinogen was obtained in the presence of trifluoro borane etherate ($\text{BF}_3 \cdot \text{OEt}_2$). Then porphyrinogen was irreversibly oxidized to tetraphenylporphyrin (TPP) by 2,3-dichloro-5,6-dicyano-1,4-benzoquinone (DDQ). [53] Later, Lindsey modified the method and dipyrromethane was obtained as a result of using trifluoroacetic acid (TFA) as catalyst. Dipyrromethane was then reacted with another aldehyde and underwent oxidation by DDQ or tetra chlorobenzoquinone (TCBQ). [54]

1.3 Supramolecular Constructs Based on Cucurbituril and Conjugated Compounds

Supramolecular assemblies of cucurbituril homologues with photoactive π -conjugated compounds covering small photoactive dyes, porphyrins, conjugated polymers and oligomers have been reported in the literature. [55] As mentioned in previous sections, conjugated compounds have been utilized in diverse applications of nanomedicine spanning biological/chemical sensing, [56],[57],[58],[59] cellular targeting, [60] fluorescence imaging, [61],[62] drug and gene delivery, [63],[64] biomedical implants, [65] tissue engineering and regenerative medicine, [66] chemotherapy, [67] photodynamic therapy [68] and photothermal therapy.

[69] However, to benefit from conjugated compounds in a broader context, some certain problems need to be eliminated such as low stability, solubility, weak optical properties (low quantum yields, low lifetime) because of aggregation. CB homologues have great potential to overcome such problems by enhancing stability and solubility. Conjugated compounds and CB homologues/derivatives can form supramolecular assemblies in the form of rotaxanes, nanoparticles, hydrogels, nanosheets, organic frameworks and so on. Within the scope of this thesis, as supramolecular architectures based on CB homologues and conjugated compounds, rotaxanes, nanoparticles and supramolecular assemblies have been constructed and utilized for nanomedicine applications.

1.3.1 Rotaxanes and Polyrotaxanes

The name of rotaxane was originated from Latin implying wheel (rota) and axle (axis). Rotaxanes are supramolecular entities based on mechanically interlocked macrocycles on a dumbbell-shaped molecule by bulky terminating groups on their ends. In such assembly, macrocycles can freely rotate. Rotaxanes own unique features and structures. Polyrotaxanes are defined as oligomeric or polymeric rotaxane species (linear segment is oligomer or polymer) and they are appealing due to ability of converting energy to mechanical movements. [70] Pseudorotaxanes and polypseudorotaxanes are intermediates of rotaxanes and polyrotaxanes respectively implying the absence of bulky stopper groups on their ends. Schematic representations of pseudorotaxane, polypseudorotaxane, rotaxane and polyrotaxane were depicted in Figure 1.17.

Nomenclature of rotaxanes are based on number of used units in construction. Generally, they are represented as [n]-(pseudo)rotaxane where n stands for number of used units. For example [2]-rotaxane implies one linear segment and one macrocycle with stopper groups whereas [3]-pseudorotaxane represents a construction containing two macrocycles threaded along a linear segment without stoppers. Rotaxanes are classified according to synthetic route, location of macrocycle and type of macrocycle. Rotaxanes can be synthesized by utilizing

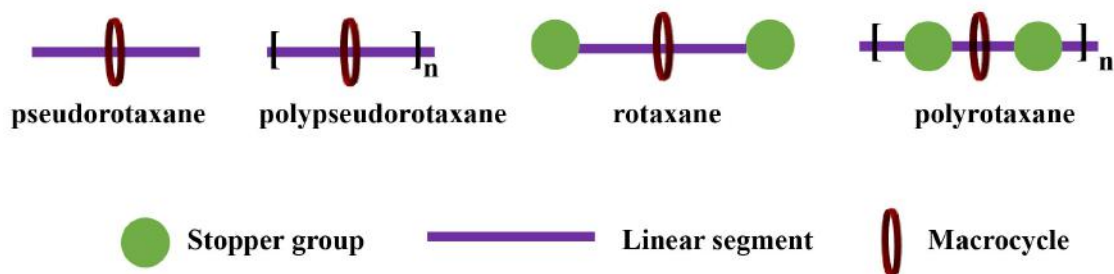


Figure 1.17: Schematic representations of pseudorotaxane, polypseudorotaxane, rotaxane and polyrotaxane.

four different ways; threading, trapping, clipping and slipping. Macrocycles can be located either on backbone or on side chain of linear segments, therefore they are classified as main chain and side chain rotaxanes respectively. Rotaxanes are also classified according to macrocycle type. In the literature, cyclodextrin, [71] crown ether, [72] cyclophanes [73] and cucurbituril [74] based rotaxanes have been reported. In this thesis, cucurbit[6]uril-based [5]-rotaxane was constructed.

1.4 Cucurbituril-Based Nanomedicine Applications

1.4.1 General View and Concepts

Nanomedicine is an interdisciplinary science based on the application of nanotechnology to medicine chiefly aiming at the development of promising techniques for modern medicine's unsolved problems regarding diagnosis, controlling, curing, preventing and eradication of diseases. [75], [76], [77]. It spans a quite broad field of study including but not limited to pharmaceutical formulations, drug delivery systems, [78] *in vivo* diagnosis (smart medical imaging technologies [79] containing computed tomography (CT), single photon emission computed tomography (SPECT), magnetic resonance imaging (MRI), positron emission tomography (PET), hybrid PET/MRI, optical coherence tomography (OCT), fluorescence imaging, photo-acoustic imaging), antibacterial agents, [80]

vaccine development, [81] infectious diseases, [82] targeting, [83] artificial tissues and organs, tissue repair, regeneration [84] and wound healing, [85] DNA analysis, [86] implants, [87] cancer therapy [88] (chemo-, radiation-, photodynamic-, photothermal-, hormone-, gene-, immuno-therapy and stem cell & bone marrow transplant).

Nanomaterials, key constituents of nanomedicine, possess high surface-to-volume ratio leading to have greater chemical reactivity. Size-, shape- and composition-engineering of nanomaterials enables tunable optical, electrical, magnetic, thermal, mechanical and structural properties as a result of quantum confinement effect. [89] Since the scale of nanomaterials are comparable to that of most biological molecules (nanoscale range: 1-100 nm), they have revolutionary potential in medicine. [90] Hereby, the maximum benefit from the advanced functionality of nanomaterials is gained for medical practice. They are designed and fabricated for desired, particular medical applications and offer some appealing possibilities such as high-throughput and high-sensitivity detection, sensing and screening of molecular changes, carriage of therapeutic materials across the biological barriers, providing access to specific molecules, building or strengthening molecular interactions, protein binding, targeting etc. [91],[92] Until 2017, approximately 50 nanotherapeutics were approved for clinical use and currently greater number of them are in various stage of clinical investigation. [93]

Advancements in supramolecular chemistry and functionalization approaches assure the controlled assembly of molecular or macromolecular building blocks (hosts or guests) to engineer nanomaterial surfaces. [94],[95] Over the last few decades, a set of macrocycles have been broadly and intensively studied involving crown ethers, calixarenes, cyclodextrins, pillararenes, cyclophanes, cucurbiturils and so forth as previously described in section 1.1.1.1. Different derivatives of those macrocycles are obtained by functionalizing them to provide biocompatibility, ability to respond to stimuli and convenience and efficacy for biological and medical applications. Among the same class of macrocyclic molecules, CBs have higher binding affinity and excellent water solubility. [96] Moreover, by virtue of their rigid structure and hydrophobic inner cavities, their complexes with guest molecules are extremely strong and stable in water. [36] They are able to form

assemblies of advanced nanomaterials. Therefore, they have attracted enormous attention and had wide range of remarkable potential in nanomedicine. In this thesis, utilization of CB-based supramolecular constructs in diverse nanomedicine applications namely drug delivery, cancer therapy (chemotherapy, photodynamic therapy and photothermal therapy), development of antimicrobial agents and cellular imaging was aimed to be presented.

1.4.2 Drug Delivery

The concept of drug delivery mainly covers the utilization of pharmaceutical formulation tactics, encapsulation methods, enhancement of drug loading efficiency of particular carriers and successive transportation of specific drugs which are sent to their targets. [97], [98] Efficient cancer therapy remains a challenge, despite the fact that numerous potent anticancer drugs have been discovered for over a century. Indeed, no drugs are effective by their nature. By efficiency of drugs, it is meant the way that they are controlled and transported. However, efficient drug delivery systems are still insufficient. Hydrophobic anticancer drugs suffer from low water solubility which restricts their use in biological media. Also, side effects may occur and impair normal cells. Supramolecular chemistry approaches using CBs enable developing effective drug delivery systems by their ability to encapsulate drugs and increasing their water solubility, improving physicochemical stability and well controlled/targeted transportation and release of drug to its target. [99] Up to now, complexation of enzyme inhibitors, ocular drugs, vitamins, hormones, neurotransmitters, neuromuscular blockers, local anesthetics, anti-pathogenic, anti-neoplastic, anti-tuberculosis and antagonist agents with CB derivatives have been reported in the literature. [100] In the table A1 (appendix) these guest molecules, their CB hosts and drug/material delivery are summarized.

1.4.3 Cancer Therapy

Cancer is global health challenge. Cancer morbidity and mortality mainly stems from metastasis. [101] Metastasis is defined as the spread of cancer cells from the location they initially formed to surrounding tissues and organs. As they depart from primary tumor, seep into blood and lymph system. Cell death appears in three distinct forms; apoptosis, autophagy and necrosis. Morphology of cells undergoing apoptosis, necrosis, autophagy and survival superiority of these processes were depicted in Figure 1.18.[102] Apoptotic cells swell and are densely packed with intracellular organelles. Necrotic cells generally owe expanded mitochondria and other organelles, ruptured membrane and some of organelles are leaked out from cytoplasm. Autophagic cells have double membranes and autophagosomal vacuoles with cytoplasmic contents.

Within the scope of this thesis, chemotherapy, photothermal therapy (PTT) and photodynamic therapy (PDT) will be covered.

1.4.3.1 Chemotherapy

With respect to fundamental anticancer treatment, traditional chemotherapeutic agents and cytotoxic drugs are primarily used therapeutics for combatting cancer. In chemotherapy, drugs are used to stop or slow the growing of tumor. [103] However, conventional chemotherapy has several deficiencies including weak solubility and stability of chemotherapeutic agents in physiological media, drug resistance, non-selective targeting, uncontrolled release and severe side effects considerably limiting efficacy of the therapy as mentioned in drug delivery section. Despite the drawbacks, chemotherapy is still considered to be one of the most effective cancer treatment method. Combining chemotherapy with other therapeutic strategies can afford more efficient and promising cancer therapy. In this context, supramolecular approach plays important role enabling integration of various functions in one platform. Supramolecular assemblies can directly be utilized in chemotherapy or function as drug delivery vehicles by encapsulating

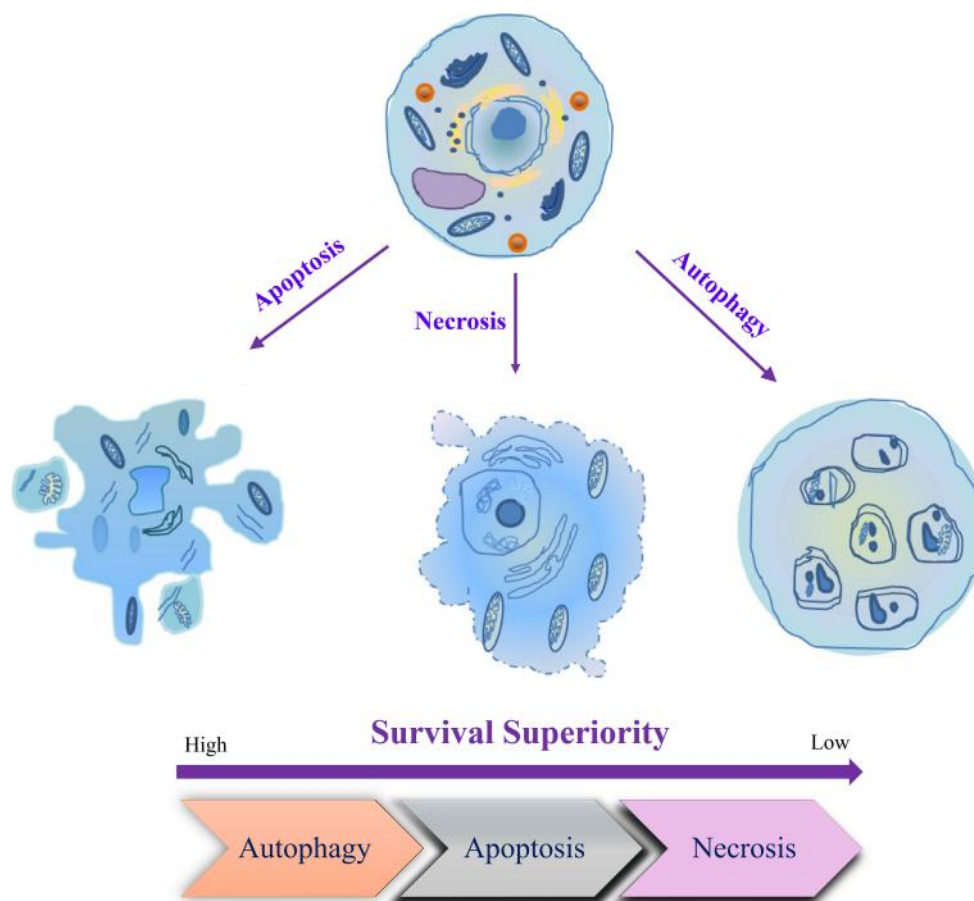


Figure 1.18: Morphology of cells after apoptosis, necrosis and autophagy and survival superiority (Reprinted with permission from ref.[102] Copyright, 2017 John Wiley & Sons, Ltd.).

anticancer drugs.

1.4.3.2 Photothermal Therapy (PTT)

Photothermal effect arises from the photoexcitation of material causing thermal energy (heat) generation. Photothermal therapy (PTT) is promising cancer therapy technique based on photothermal effect mainly irradiating ablation agents (or photothermal agents) by generally NIR-laser to convert light energy into thermal energy. Main benefit of PTT is its capability of wavelength-dependent selectivity. Thermal energy implies released heat causing rapid temperature increase which

generates local hyperthermia (41-48 °C) or irreversible injury (48-60 °C) resulting in tumor cell death. Elevated temperature kills cancer cells selectively without damaging normal cells, since normal cells own higher heat tolerance than that of cancer cells. In Figure 1.19, destruction of tumor cells by photothermal cancer therapy is shown. Similarly, photothermal therapy concept can be utilized for antimicrobial killing.

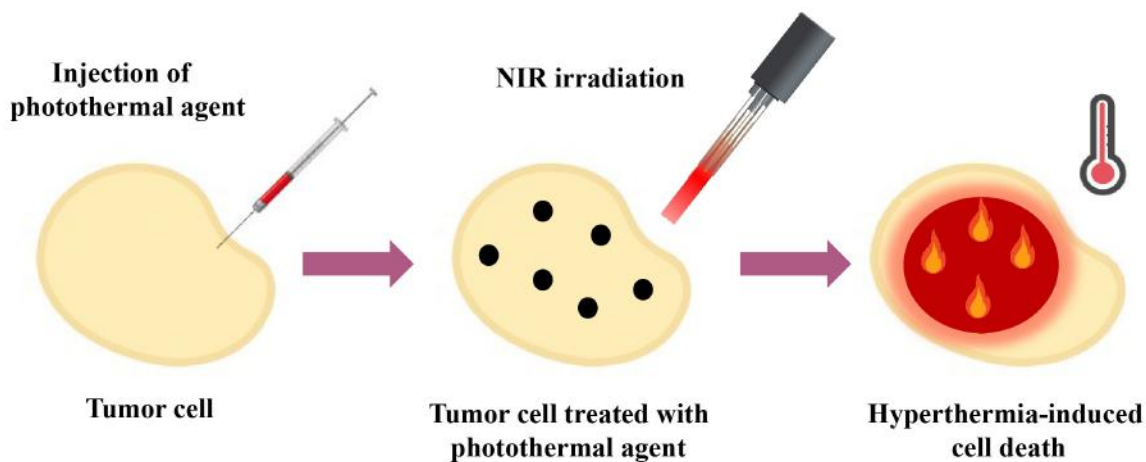


Figure 1.19: Photothermal cancer therapy.

Gold nanomaterials including gold nanoparticles, nanorods, nanocages and nanostars have been superior choice for photothermal therapy owing to considerable localized surface plasmon resonance (LSPR) effect in the near-infrared region (NIR) and this allows NIR light energy to be converted to thermal energy in high yield. They hereby potentiate PTT.

1.4.3.3 Photodynamic Therapy (PDT)

Photodynamic therapy (PDT) is a treatment modality combining photophysical and photochemical processes to obtain desirable therapeutic outputs. PDT is based on using light-activated drugs called photosensitizers (PS). [104] PDT has three basic components; PS, light and oxygen. When the proper PS is excited by the specific wavelengths of light, reactive oxygen species (ROS) including

peroxides, superoxide, hydroxyl radical and singlet oxygens are generated from the molecular oxygens to induce the cell and tissue death as given in Figure 1.20.

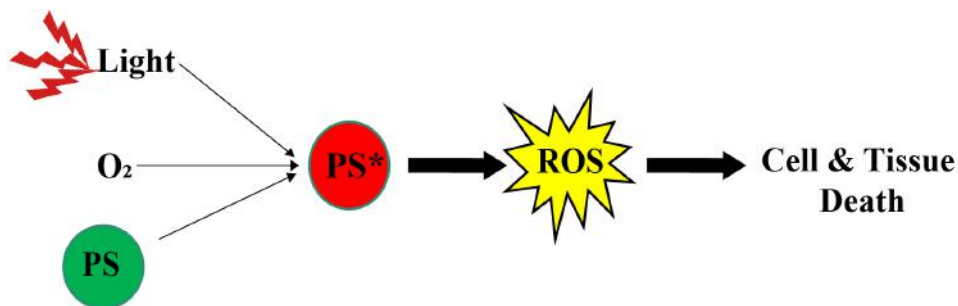


Figure 1.20: Activation of photosensitizer to produce ROS giving rise to cell and tissue death.

In the low-energy molecular orbital, the ground-state PS normally possesses two electrons in opposite spins. One of these electrons is excited to higher energy molecular orbital (singlet excited state) upon light absorption preserving its spin. PS in singlet excited state is not capable of undergoing reactions with cellular substrates due to its quite short lifetime ($\sim 10^{-9}$ - 10^{-12} s). Excited PS can relax back to its ground state by fluorescence or by non-radiative relaxation as shown in Jablonski energy diagram (Figure 1.14). Otherwise, the excited singlet state might immediately experience intersystem crossing in which the spin of the excited electron changes for forming excited triplet state whose lifetime is longer than that of excited singlet state ($\sim 10^{-6}$ - 10^{-3} s). The triplet state PS can also return to ground state through phosphorescence or non-radiative relaxation. In the course of PDT, the excited triplet state can either directly undergo reaction with cellular substrates resulting in generating of ROS species defined as Type-I reaction or transfer energy to molecular oxygen yielding highly reactive singlet oxygen ($^1\text{O}_2$) (Type-II reaction). $^1\text{O}_2$ is regarded as the most harmful species because of reacting with biomolecules such as proteins, lipids and nucleic acids. Therefore, PSs can destroy tumors via type-I reaction, type-II or both at the same time (Figure 1.21). Ideal PS should be able to generate high triplet quantum yield with longer lifetime and high singlet oxygen quantum yield. It should have well-defined chemical composition, good water solubility, stability and negligible dark cytotoxicity. Besides, PSs absorbing longer wavelengths (600-800

nm) can afford higher therapeutic efficacy since light penetrates in tissue more. Clinically applied PSs are porphyrin, phthalocyanine and chlorine species.

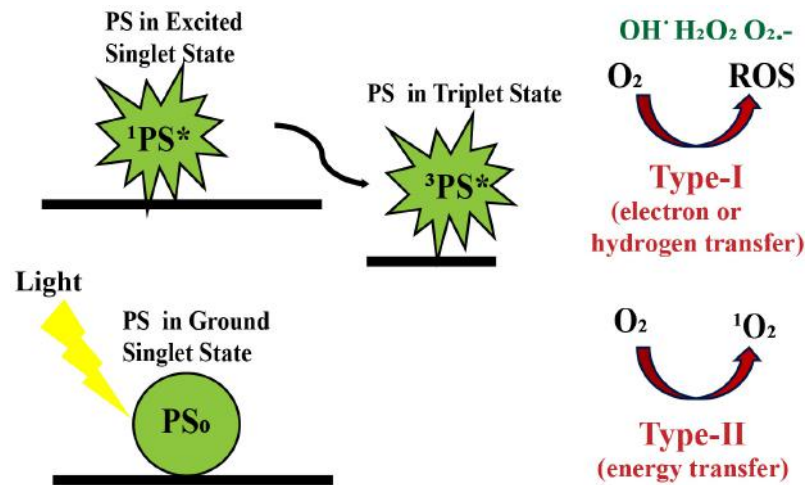


Figure 1.21: Type-I reaction (electron or hydrogen transfer) and type-II reaction (energy transfer) in PDT.

Clinically, PDT is employed as depicted in Figure 1.22. After the administration of PS, it accumulates throughout the body. Then it selectively accumulates on target tissue and when it is irradiated by light, it will destroy target tumor. Destruction of cells are mainly based on apoptosis in PDT.

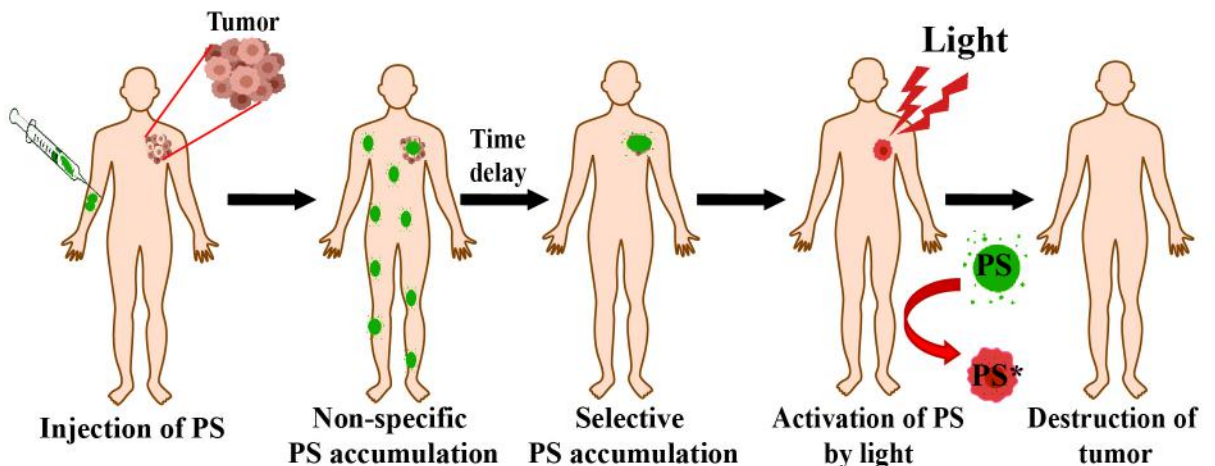


Figure 1.22: PDT in clinical practice.

PDT has been gaining keen attention as clinically approved antimicrobial and antitumor strategy offering minimal invasiveness, enhanced targeting properties and reduced side effects in comparison with the other conventional therapies. [105], [106], [107] On the other hand, PDT has several limitations including restricted light penetration depth rendering PDT challenging for superficial tumors, oxygen-dependence making it unavailable for hypoxic tumors and self-catalysation of conventional PSs. To overcome these drawbacks and enhance therapy efficiency, therapeutic strategies are combined.

1.4.3.4 Combination of PDT with Other Therapies

Cancer includes many complicated pathological phases. Thus, achievement of effective cancer therapy with mono-therapeutic strategy might be challenging. [108] In addition, individual treatment modalities have their own limitations and deficiencies. To address insufficiencies and obtain more desirable therapeutic outcomes, PDT has been combined with chemotherapy, radiotherapy, PTT, immunotherapy etc. In this thesis, PDT is combined with chemotherapy and PTT. Combining PDT and chemotherapy has been extensively conducted to achieve synergistic therapeutic effect. Combination strategy relies on the co-delivery of PS and chemotherapeutic agent. Combination may not always yield synergistic effect, it might be additive effect, synergistic effect or antagonistic effect. Synergistic effect refers to working together and is the most desirable effect. When the therapeutic effect is greater than the sum of individual therapies, it is synergism. When the therapeutic effect is the sum of individual effects, it is additive effect and when combination of two or more therapies causes less effect than the sum of individual treatments, it is referred as antagonistic effect. In the literature, combination of PDT and chemotherapy based on additive, synergistic and antagonistic effects have been reported. Multimodal synergistic therapy strategies aim to enhance therapeutic outputs of individual therapies by cooperatively integrating them into a single theranostic platform. In the literature, it has been shown that the logical combination of PDT with PTT could afford efficacious

cancer treatment since photodynamic and photothermal properties are synergistically exploited. In theory, hyperthermia caused by photothermal conversion accelerates intratumoral blood flow leading increasing oxygen demand for more efficient photodynamic effect. [109],[110] Other advantage of implementing synergistic PDT and PTT is that, the temperature elevation by photothermal effect could promote the enhanced permeability of tissues for improving the delivery efficiency and cellular uptake of injected PSs. [111],[112]

1.4.4 Development of Antimicrobial Agents

Although the first antibiotic, penicillin, was discovered more than 90 years ago, antibiotics are still considered the most potent way for infection treatment and bacterial biofilm disruption. On the other hand, overuse/misuse of antibiotics leads to rapid evolution of resistant bacteria which endangers the usefulness of antibiotics. [113] For that purpose, alternative strategies such as smart antibacterial and anti-biofilm surfaces to combat bacterial infections and biofilm formation are being developed. [114] Supramolecular approach is also useful in this regard, since supramolecular materials have unique properties like flexible and tunable interactions with biomolecules and having high potential to assemble wide range of agents. [115] PDT and PTT approaches are also useful to provide microbial killing. Antimicrobial PDT has been applied to pathogens including viruses, bacteria, parasites and fungi (Figure 1.23).

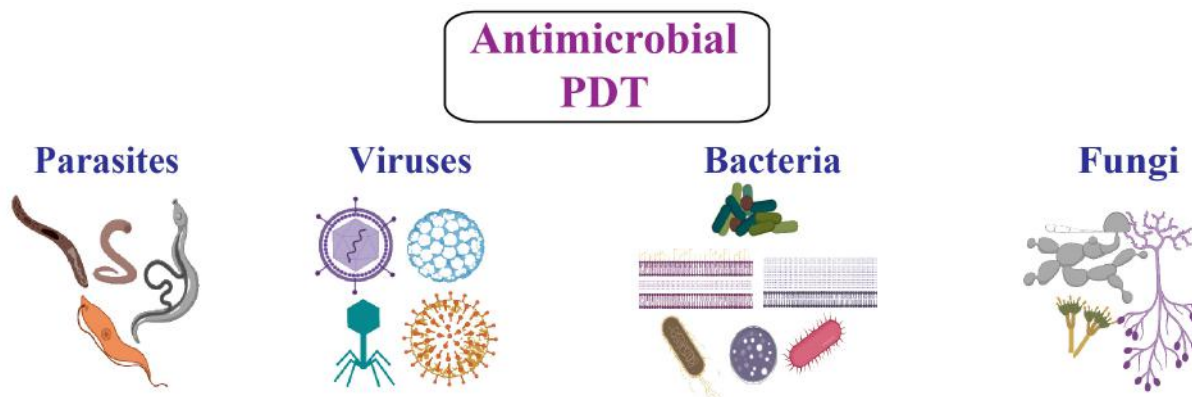


Figure 1.23: Pathogen species inactivated by PDT.

Recently, CB-based supramolecular constructs have been reported in the literature as photoactive antibacterial agents [116], [117]. In these constructs, CB7 formed host-guest interactions with photoactive porphyrin derivatives. Controllable antimicrobial activities of resulting supramolecular photosensitizers were demonstrated. Dark cytotoxicity caused by cationic porphyrin derivatives were eliminated and light-triggered inhibitory effects were completely preserved upon CB7 binding. These systems were promising improvements to combat infectious diseases caused by bacteria. Alongside of controllable antimicrobial behaviour, further utilization of supramolecular chemistry of CBs to design multifunctional platforms will be focused in this thesis.

Chapter 2

Experimental

Some parts of this chapter were reported in the following publications: [118], [119], [120]

•**M.Özkan**, Y. Keser, S.E. Hadi and D.Tuncel, [5]Rotaxane- Based Photosensitizer for Photodynamic Therapy. *Eur. J. Org. Chem.* 2019, 3534-3541.

•**M.Özkan**, Y.Kumar, Y.Keser, S.E. Hadi and D.Tuncel, Cucurbit[7]uril-Anchored Porphyrin-Based Multi-Functional Molecular Platform for Photodynamic Antimicrobial and Cancer Therapy.*ACS Appl. Bio Mater.* 2019, 2, 11, 4693-4697.

•**M.Özkan**, S. E. Hadi, I. Tunc, Y. Midilli, B. Ortac and D. Tuncel, Cucurbit[7]uril-Capped Hybrid Conjugated Oligomer-Gold Nanoparticles for Combined Photodynamic-Photothermal Therapy and Cellular Imaging. *ACS Appl. Polym. Mater.* 2020, DOI:10.1021/acsapm.0c00540.

2.1 Materials

All chemicals used in the chemical syntheses were of analytical grade and used as received. Milli-Q water (18.2 M Ω cm at 25 °C) was used when needed. Solvents were dried and distilled before use and all reactions were run under air unless otherwise stated. Column chromatography was run by silica gel purchased from Sigma-Aldrich (high-purity grade, with pore size of 60 Å, 70-230 mesh, 63-200 pm) or Sephadex G-15 medium. Reaction steps were followed by thin layer chromatography (TLC) using silica-coated (Merck TLC Silica Gel F254) TLC plates, visualizing by shortwave (254 nm) or longwave (365 nm) LTV light. All deuterated solvents (CDCl₃ and D₂O) used in NMR spectroscopy were purchased from Merck.

In the bacterial assays, *E. coli* DH5- α strain (gram-negative) and *B. subtilis* MTCC 441 strain (gram-positive) were used. For the preparation of liquid Luria-Bertani (LB) as growing medium and semi-solid LB agar, sodium chloride, tryptone, yeast extract and agar powder were purchased from Sigma-Aldrich. For agar disk diffusion assays, Whatman qualitative filter paper Grade 3 were used and ampicillin was purchased from Sigma-Aldrich. In SEM imaging of *E. coli*, glutaraldehyde solution was purchased from Merck.

For mammalian cell culture, Dulbecco's Eagle Medium (DMEM), L-glutamine and sodium pyruvate were purchased from Sigma-Aldrich, fetal bovine serum (FBS) penicillin/streptomycin (Pen-strep) were from Thermo Fischer Scientific and MEM non-essential amino acids solution was from Merck. For passaging cells, Gibco Trypsin-EDTA (0.25%) was used. PBS (10X) was purchased from Sigma-Aldrich and diluted by distilled water 10-fold and autoclaved when 1X PBS is needed. For the measurement of cell viability, MTT from Sigma-Aldrich was used. For labeling nuclear DNA for confocal laser scanning microscopy imaging, paraformaldehyde was purchased from Carlo Erba Reagents, Triton X-100 detergent from Merck and DAPI from Thermo Fischer Scientific.

2.2 Instrumentation

2.2.1 ^1H and ^{13}C Nuclear Magnetic Resonance (NMR) Spectroscopy

Chemical structures of compounds were characterized by using Bruker AVANCE DPX-400 NMR spectrometer operating at 400 MHz and at 100 MHz for ^1H -NMR and for ^{13}C -NMR respectively. All the spectra were recorded at 25°C dissolving products in deuterated solvents. Chemical shifts were written in ppm relative to the internal standard tetramethylsilane (TMS). Spin multiplicities are abbreviated as: s (singlet), d (doublet), t (triplet), q (quartet), m (multiplet).

2.2.2 Electrospray Ionization-Mass Spectrometry (ESI-MS)

Molecular weight analyses of products were performed using Agilent 6224 Accurate-Mass Time-of-Flight (TOF) LC/MS and Agilent 6530 Accurate-Mass Q-TOF LC/MS systems.

2.2.3 UV-Visible (UV-Vis) Absorbance Spectroscopy

Absorption spectra of compounds were recorded in solution using quartz cuvette with 10 mm path length using Cary 300 UV-Vis spectrophotometer equipped with Xenon flash lamp. For nanoparticles, UV-vis-NIR absorbance spectrum were recorded in the spectral range of 250–1100 nm.

2.2.4 Fluorescence Spectroscopy

Photoluminescence spectra were obtained in solution phase using quartz cuvettes with 10 mm path length on Varian Cary Eclipse fluorescence spectrophotometer.

2.2.5 Fourier-Transform Infrared (FT-IR) Spectroscopy

Bruker Alpha-II Platinum ATR FT-IR spectrometer was used for the determination of the chemical functional groups of compounds. The spectra were recorded in the spectral range of 400-4000 cm^{-1} with resolution of 2 cm^{-1} .

2.2.6 Time-Resolved Fluorescence (TRF) Spectroscopy

TRF measurements were performed by Pico Quant FluoTime 200 spectrometer. Materials were introduced in solution phase and excited by a picosecond pulsed laser at a wavelength of 375 nm. Obtained fluorescence decay curves were recorded on TimeHarp time-correlated single-photon counting unit then fitted to multiexponential decays using FluoFit software.

2.2.7 Dynamic Light Scattering (DLS) and Zeta Potential

Sizes and zeta potentials of the nanoparticles was examined on Malvern Zetasizer Nano ZS equipped with 663 nm laser at 25°C. DLS measurements were taken using standard fluorescence cuvette whereas zeta potential measurements were taken using folded capillary zeta cell.

2.2.8 Scanning Electron Microscopy (SEM)

Morphological changes of bacteria treated with samples were visualized using Quanta 200 FEG Thermo Fisher Scientific and instrument operated at environmental scanning electron microscopy mode.

2.2.9 Confocal Laser Scanning Microscopy (CLSM)

CLSM images were captured by Leica TCS SP8 X multiphoton system by using 20X objective.

2.2.10 Isothermal Titration Calorimetry (ITC)

ITC was recorded on MicroCal VP-ITC Malvern Panalytical.

2.2.11 Microplate Reader

Optical density at 600 nm (OD_{600}) of bacteria and the absorbance for MTT analysis (at 570 nm) were recorded on SpectraMax M5 multi-detection microplate reader system.

2.2.12 Critical Point Dryer (CPD)

Samples were dried by Autosamdri-934 Tousimis CPD in cleanroom using CO_2 at 7.4 MPa, 30° and ethanol as intermediate fluid.

2.2.13 Thermal Imaging Camera

In photothermal conversion analysis, temperature changes were recorded by using FLIR Thermovision A40 Thermal Imaging Camera.

2.3 Syntheses

2.3.1 [5]-Rotaxane

2.3.1.1 Synthesis of Cucurbit[n]urils (1) and (2)

CB6 (1) and CB7 (2) were synthesized according to the literature procedure. [23], [24]

2.3.1.2 Synthesis of 5,10,15,20-tetrakis(α -bromo-*p*-tolyl)porphyrin (TPP-Br) (3)

Compound (3) was obtained according to the procedure reported in the literature. [121] 1.50 g (7.5 mmol) of α -bromo-*p*-tolualdehyde and 0.525 g (7.5 mmol) of pyrrole were added to 0.75 L of chloroform. During stirring, 0.355 g (2.5 mmol) of Et₂.BF₃ was added to the mixture. Stirring was continued for 1 hour more at RT followed by the addition of 0.305 g (3.0 mmol) of Et₃N and 1.385 g (5.65 mmol) of tetrachloro-*p*-benzoquinone (TCBQ). Then, the temperature was increased to reflux and kept under reflux for 1 h under N₂. The volume of the mixture was then reduced to 200 mL and filtered through silica gel (neutral). After the filtrate was dried under reduced pressure, the purple precipitate was dissolved in toluene. The solution was passed over silica gel, eluting with toluene. After toluene was removed, the sediment was washed with methanol, giving shiny purple fine crystals. The product was dried at 100°C under vacuum.

Yield: 794 mg, 43%.

¹H-NMR (400 MHz, CDCl₃, RT) δ (ppm): 8.867 (s, 8 H), 8.205 (d, 8 H), 7.811 (d, 8 H), 4.884 (s, 8 H), -2.783 (s, 2 H).

2.3.1.3 Synthesis of Prop-2-ynyl-4-[10,15,20-tris-(4-prop-2-ynylaminomethyl-phenyl)-porphyrin-5-yl]-benzyl-amine (alkyne-substituted porphyrin) (4) and (5)

To obtain (4) and convert it into (5), literature procedure was adapted. [122] Excessive-amount of propargylamine (2.0 mL, 30 mmol) was added in a one-necked round-bottomed flask. After compound (3) (146 mg, 0.15 mmol) was dissolved in DCM, it was added dropwise to the flask containing propargylamine. The mixture was stirred for 72 h at RT. To monitor the reaction TLC was used (DCM: methanol, 7:1, v/v). After the completion of reaction, NaOH solution (0.1 N, 10 mL) was added to the reaction mixture while stirring (1h at RT). Then DCM was added to separate the dark red organic layer. Solvent was evaporated under reduced pressure to obtain purple sediment (4). For the purification of purple solid, column chromatography was utilized (DCM: methanol mixture, 10:1, v/v as eluent). For the protonation of (4), aqueous HCl (0.1 N, 5 mL) was added to convert (4) to (5). Protonation was observed from the color change from dark reddish purple to green. After stirring mixture for 8 h at RT, the solvent was evaporated under reduced pressure and green solid (5) was purified through recrystallization in water–acetone mixture. Green powder was dried for 12 h at 40 °C.

Yield: 120 mg, ~80%.

¹H-NMR (400 MHz, CDCl₃, RT) δ (ppm): 8.9 (s, 8 H), 8.7 (d, 8 H), 7.7 (d, 8 H), 4.3 (s, 8 H), 3.7 (d, 8 H), 2.4 (t, 8H) -2.7 (s, 2 H).

2.3.1.4 Synthesis of [5]-rotaxane (**6**)

To the solution of compound (**5**) (50 mg, 0.049 mmol) in DI water (5 mL), compound (**1**) (214 mg, 0.215 mmol) was added. The stirring of resulting mixture for 1 h (to dissolve (**1**)) yielded a green solution. *tert*-butylazidoethylamine (38.3 mg, 0.215 mmol) was added to the mixture and it was stirred for 24 h at RT. Once reaction was complete, the reaction mixture was poured into a dialysis membrane (regenerated cellulose, MW cut-off 12 kDa) and dialyzed against water for 24 h for the removal of excessive (**1**) and unreacted monomers. Dialysate was freeze-dried to obtain a fluffy burgundy-colored powders (**6**).

Yield: 245 mg, 87%

UV/Vis (H₂O): λ_{max} : 415 nm (35 × 10⁴), 517 (14 × 10³), 553 (8.5 × 10³), 582 (6.2 × 10³), 636 (4.2 × 10³).

¹H-NMR (400 MHz, D₂O, RT) δ (ppm): 1.61 (s, 36H, o), 3.81 (t, 8H, ³J_{HH} = 7.95 Hz, m), 4.13 (t, 8H, ³J_{HH} = 8.15 Hz, l), 4.25 (48 H, CB), 4.39 (s, 8H, i), 4.86 (s, 8H, h), 5.52 (48H, CB), 5.75 (48H, CB), 6.62 (s, 4H, k), 8.52 (d, 8H, ³J_{HH} = 9.9 Hz, e), 8.79 (d, 8H, ³J_{HH} = 10.1 Hz, f), 9.09 (s, 8H, a).

2.3.2 CB7-Porphyrin Conjugate (TPP-4CB7) (**7**)

CB7-porphyrin conjugate (TPP-4CB7) (**7**) was obtained according to the literature procedure. [123]

2.3.3 Red-Emitting Conjugated Oligomer Nanoparticles (COL NPs)

2.3.3.1 Synthesis of Red-Emitting Conjugated Oligomer (8)

3,3',3'',3'''-[(1E,1'E)-2,1,3-Benzothiadiazole-4,7-diylbis(ethene-2,1-diyl)]-bis(9H-fluorene-9,9,2-triyl)-tetrakis(N,N-dimethylpropan-1-amine) (Red-emitting conjugated oligomer (COL)) was synthesized according to the literature procedure.[64]

2.3.3.2 Synthesis of COL and Hybrid Core-Shell COL-Au (COL: Au , 2:1) nanoparticles (9) and (10)

To prepare COL NPs (9), (8) (5 mg, 5.8 μmol) was dissolved in 5 mL of THF. 2 mL of (2.35 μmol) solution of (8) was added to 15 mL of Milli-Q water while sonicating for 30 min at medium intensity. THF was evaporated by using rotary evaporator under reduced pressure. Hybrid COL-Au nanoparticles (COL-Au NPs) (9) were obtained by injecting the 2 mL of THF solution of (8) (2.35 μmol) into 20 mL aqueous solution of AuCl_3 (1.18 μmol) dropwise. The mixture was sonicated for 30 min at 25 °C and then THF was removed under reduced pressure to obtain stable (10) dispersion in water which was further poured into a regenerated cellulose membrane (MW cut-off 12 kDa) and dialyzed against water for 6 hours to remove unreacted Au ions.

2.3.3.3 Capping (9) and (10) by (2)

The aqueous solution of (2) was added to prepared (9) and (10) by keeping the concentration ratio 1:4 ((8): (2)) and mixed gently. Then mixtures were poured into a regenerated cellulose membrane (MW cut-off 12 kDa) and dialyzed against water for 6 hours to remove excess (2). Capping (9) by (2) yielded CB7@COL-NP (11) and capping (10) by (2) yielded CB7@COL-Au-NP (12).

2.4 Reactive Oxygen Species (ROS) Detection

To detect ROS generation capacity of prepared photosensitizers **(6)**, **(7)**, **(9)**, **(11)**, DCFH-DA assay was utilized by adapting literature procedure. [117] 40 μM solution of 2,7-dichlorofluorescein (DCFH) was prepared from the hydrolysis of dichlorofluorescein diacetate (DCFH-DA) in alkaline media. DCFH in sodium phosphate buffer (pH 7.4) was maintained in cold ($2\text{ }^{\circ}\text{C}$) and dark-medium. Fluorescent DCF (excitation wavelength 488 nm, emission wavelength 524 nm) formed in the presence of reactive oxygen species (ROS) with 90% quantum yield. ROS generation ability of photosensitizers were examined, by initially performing the blank measurements: 0.5 mL of 40 μM DCFH was diluted by 1 mL of water and excited at 488 nm. The emission intensity at 524 nm was recorded (0 min) then the solution was exposed to white light ($1\text{ mW}/\text{cm}^2$) for 4 minutes, and the emission intensity of the blank solution was recorded after every minute. After blank measurements, 100 μL of 5 μM of photosensitizer solutions were placed to the blank DCFH solution, irradiated by white light ($1\text{ mW}/\text{cm}^2$) for 4 minutes and emission intensities at 524 nm were measured each minute.

2.5 Determination of Photothermal Conversion Efficiency and Thermal Stability

The photothermal properties **(9)**, **(10)**, **(11)** and **(12)** nanoparticles were determined by measuring the temperature elevation upon NIR-laser irradiation. 1 mL solutions of each sample were placed in an Eppendorf tube and exposed to NIR-irradiation (915 nm) for 10 min. After irradiation period, for observing thermal reversibility, laser was shut off and temperature decrease was recorded for 10 min. by IR camera. For the analysis of concentration- and laser intensity-dependence of photothermal performance, the same protocol was followed by varying nanoparticle concentrations and laser dosage.

2.6 Isothermal Titration Calorimetry (ITC)

The complexation between **(2)** and doxorubicin (DOX) was examined by performing ITC titration of 0.1 mM **(2)** with 1 mM DOX in DMEM. 200 μL of **(2)** solution was in the sample cell while 40 μL of DOX was in the syringe. Stirring speed was set to 300 rpm. In total, 40 injections of 1 μL aliquots each separated by 240 s spacing were performed. Temperature was adjusted to 25 $^{\circ}\text{C}$. The measurement was taken at least two times with different **(2)** and DOX solutions in DMEM. The heat of dilution of **(2)** and DOX in DMEM were subtracted from the heat of complexation.

2.7 Bacterial Experiments

2.7.1 Preparation of *E. coli* and *B. subtilis* Suspensions

A single colony of *E. coli* and *B. subtilis* from semi-solid Luria-Bertani (LB) agar plate was placed to 5.0 mL of liquid LB culture medium and incubated (37 $^{\circ}\text{C}$, 200 rpm, 14 hours). They were harvested by centrifugation (2 min, 4 $^{\circ}\text{C}$, 7000 rpm). Centrifugation was followed by sequential washing by fresh 1X Phosphate-buffered saline (PBS) three times. After discarding supernatant, residues of *E. coli* and *B. subtilis* were resuspended in PBS and then diluted until the value of optical density at 600 nm (OD_{600}) of the bacterial suspensions reaches ~ 1.0 .

2.7.2 Determination of Minimum Inhibitory Concentration (MIC Assay)

Broth microdilution method was used to determine the respective MIC values of photosensitizers. A single colony of *E. coli* from semi-solid Luria-Bertani (LB) agar plate was placed to 5.0 mL of liquid LB culture medium and incubated (37

°C, 200 rpm, 14 hours). Bacterial suspension was diluted with pure LB medium till the initial OD₆₀₀ value reaches to ~1.0. Different concentrations of (6), (7), (9) and (10) were prepared. Each well of 96-well plate were inoculated with 100 μL of bacterial suspension and then mixed with 10 μL of each concentration. Control groups were treated with 10 μL of Gibco 1X PBS. Control and photosensitizer-treated groups were irradiated with white light (22 mW/cm²). The same experiment was carried out in the dark medium as well. Then 96-well plates were incubated (37 °C, 100 rpm, 14 hours). After the incubation period, OD₆₀₀ was measured on microplate reader. The experiment was repeated in triplicate for nanoparticle-treated *E. coli* and one time for control group.

2.7.3 Photodynamic Inactivation of Bacteria

2.0 mL of dilute suspensions of *E. coli* were incubated with various concentrations of (6), (7), (9) and (10) (37 °C, 200 rpm, 15 min), whereas the control group was treated with the equal volume of PBS. Then both treated and control groups were exposed to white light (22 mW/cm²). Bacterial suspensions of each group were serially diluted (10⁵ fold) by PBS. 50 μL-portions from the diluted bacterial mixtures were spread on the semi-solid LB agar plates and incubated (16 h, 37 °C). After incubation period, colony forming units (CFUs) were quantified. The same experiment was performed in the dark. Mean *E. coli* log₁₀ colony forming units (CFU) reduction graph upon treatment with photosensitizers in the dark and under white light was plotted. log reduction was calculated as log₁₀ reduction=log₁₀(C/T) where C and T are CFU of control and treated groups respectively.

2.7.4 ζ-Potential Measurements

Bacterial solutions (200 μL, OD₆₀₀~1.0) in 1 mL of PBS were incubated with photosensitizers (37 °C, 200 rpm, 1 min). *E. coli* and *B. subtilis* were harvested by centrifugation (2 min, 7000 rpm) and supernatant was decanted. Residues

were washed with water and resuspended in 1 mL of water. Bacterial suspensions were placed in ice box for ζ -potential measurements. Measurements were taken at RT.

2.7.5 Imaging of Antibacterial Activity by SEM

1 cm x 1 cm-sized silica wafers were incubated with isopropanol and ethanol for 30 min each to clean up organic contamination and they were completely dried at 37 °C incubator. Clean silica wafers were placed to 12 well-plate. Each photosensitizer was added to suspensions of *E. coli* (100 μ L, OD₆₀₀~1.0) in 1 mL of PBS (37 °C, 200 rpm, 15 min) and then irradiated upon white light (22 mW/cm²). Control groups were treated with the equal volume of PBS. The same procedure was followed in the dark. 10 μ L from each group were fixed onto silica wafers by 2.5 % glutaraldehyde solution in PBS (4 °C, 14 h). Next day, wafers with *E. coli* were sequentially washed with 1X PBS, autoclaved distilled water, 25 %-, 50%-, 75%- and 100% (v/v) ethanol for 2 min each. Washing steps were followed by critical point drying (CPD) in clean room. Dry samples were coated 5 nm with Au/Pd alloy and analysed at 15 kV.

2.7.6 Agar Disk Diffusion Assay

The antibacterial PDT and PTT efficacies of **(9)**, **(10)**, **(11)** and **(12)** towards *E. coli* and *B. subtilis* bacteria were analysed by agar disk diffusion assay. Both *E. coli* and *B. subtilis* strains were inoculated in LB and grown (37 °C, 200 rpm, 14 hours). Bacterial cultures were diluted 100-fold by fresh LB and grown to mid-log phase (OD₆₀₀~ 0.5–0.6). From each strain, 150 μ L of cultures were spread evenly throughout the agar plates. 10 μ L from each nanoparticle and test antibiotic (ampicillin) were placed on circular filter papers (5 mm in diameter). The UV sterilized dry disks were placed on the agar plates at RT. Agar plates were incubated for 14 h at 37 °C. The antibacterial activities of nanoparticles were visualized by measuring radii of inhibition zones after 3 min white light exposure

(22 mW/cm²) for PDT, 3 min laser exposure (915 nm, 7W/cm²) for PTT and consecutive white light and laser exposure for combined PDT/PTT evaluations.

2.8 *In vitro* Experiments

To determine *in vitro* cell viability, methyl thiazolyl tetrazolium (MTT) assay was used.

2.8.1 Cell culture

MCF-7 cells were cultured in DMEM supplemented with 10% fetal bovine serum, 1% penicillin/streptomycin, 1% L-Glutamine, 0.1 mM non-essential amino acids, 1 mM sodium pyruvate at 37°C, 5% CO₂-humidified atmosphere in the dark. Cells were grown in 75 cm² canted-neck tissue culture flasks and passaged each 3 days using Trypsin/EDTA at ~70-80 % confluency.

2.8.2 Cytotoxicity and photo-cytotoxicity

2×10³ cells were seeded in 96-well tissue culture plates for 24 h. Next day, cells were treated with various concentrations of photosensitizers and DMEM control each with three replicas. After 72 h, culture media was vacuumed and 10 μL of filtered MTT stock solution (12 μM in PBS) was added to 100 μL fresh medium in each well. Plates were incubated 4 h and after incubation period, the purple formazan product was dissolved in 110 μL of SDS-HCl solution (1 g of SDS in 10 mL of 10 mM HCl) and kept in a 37 °C incubator for 16 h. Colour absorbance was measured on microplate reader at 570 nm. For photo-cytotoxicity determination, MCF-7 cells were seeded and treated as described above. After 48 h from the treatment with nanoparticles, each group was exposed to white light (20 mW/cm²) and then incubated further for 24 h in the dark at 37 °C.

The same MTT addition and absorbance reading procedures were followed for dark-treated groups as well. Results were normalised to DMEM control group. The concentrations of **(6)** used for MTT assays conducted for measuring relative cell viability are given in table 2.1 (in the dark) and 2.2 (under light) (FC=Final Concentration, [5]-rotaxane stock solution=1 mM, FV/well=Final Volume per well) and the concentrations of **(9)**, **(10)**, **(11)** and **(12)** are given in table 2.3.

Dark	FC (μM)	[5]-Rotaxane(μL)	PBS (μL)	DMEM (μL)	FV/well (μL)
Conc.1	0	0	30	70	100
Conc.2	10	1	29	70	100
Conc.3	30	3	27	70	100
Conc.4	50	5	25	70	100
Conc.5	75	7.5	22.5	70	100
Conc.6	100	10	20	70	100
Conc.7	125	12.5	17.5	70	100
Conc.8	150	15	15	70	100
Conc.9	175	17.5	12.5	70	100
Conc.10	200	20	10	70	100
Conc.11	250	25	5	70	100
Conc.12	300	30	0	70	100

Table 2.1: Concentrations used MTT assay for [5]-rotaxane in the dark.

Light	FC (μM)	[5]-Rotaxane(μL)	PBS (μL)	DMEM (μL)	FV/well (μL)
Conc.1	0	0	10	90	100
Conc.2	2	0.2	9.8	90	100
Conc.3	5	0.5	9.5	90	100
Conc.4	10	1	9	90	100
Conc.5	20	2	8	90	100
Conc.6	30	3	7	90	100
Conc.7	40	4	6	90	100
Conc.8	50	5	5	90	100
Conc.9	65	6.5	3.5	90	100
Conc.10	80	8	2	90	100
Conc.11	90	9	1	90	100
Conc.12	100	10	0	90	100

Table 2.2: Concentrations used MTT assay for [5]-rotaxane under light.

Dark/Light	FC ($\mu\text{g}/\text{mL}$)	NP(μL)	PBS (μL)	DMEM (μL)	FV/well (μL)
Control	0	0	100	400	500
Conc.1	1.5	0.9	99.1	400	500
Conc.2	4.4	2.6	97.4	400	500
Conc.3	13.1	7.7	92.3	400	500
Conc.4	39.4	13	87	400	500
Conc.5	118	69	31	400	500

Table 2.3: Concentrations used MTT assay for nanoparticles in the dark and under light.

2.8.3 Drug Loading

In vitro anti-cancer activities of Doxorubicin (DOX), cytotoxic activities of **(7)** and their combined anti-proliferative activities on MCF-7 breast cancer cell line was determined by MTT cell viability assay using similar method as described above. Concentrations of **(7)** and drug (DOX) used in the MTT cell viability assays are tabulated in Table 2.4 (FC=Final concentration (μM), V=required volume from 1mM of stock solution (μL), PBS, DMEM and final volume/well in μL).

DOX+(7)	FC (7)	FC DOX	V (7)	V (DOX)	PBS	DMEM	FV/well
Conc.1	0	0	0	0	50	450	500
Conc.2	1	2	0.5	1	49.5	449	500
Conc.3	2	5	1	2.5	49	447.5	500
Conc.4	4	10	2	5	48	445	500
Conc.5	8	15	4	7.5	46	442.5	500
Conc.6	10	20	5	10	45	440	500
Conc.7	15	25	7.5	12.5	42.5	437.5	500
Conc.8	20	30	10	15	40	435	500
Conc.9	25	35	12.5	17.5	37.5	432.5	500
Conc.10	30	40	15	20	35	430	500
Conc.11	50	50	25	25	25	425	500
Conc.12	100	60	50	30	0	420	500

Table 2.4: Concentrations used MTT assay for TPP-4CB7 and DOX in the dark and under light.

2.8.4 Statistical Analysis

Differences in MTT relative cell viability were normalized according DMEM control group. Analysis was performed for each concentration for the dark and for the light conditions separately using one-way ANOVAs followed by multiple comparisons (Tukey 's at $\alpha=0.05$; Graphpad). ****P<0.0001 represents the difference is non-significant (ns).

2.8.5 Preparation of Cell Fixative Solution

20 mL of 1X PBS was heated to 60 °C while stirring in a round bottom flask and 1g of paraformaldehyde powder was transferred to the flask. 1N of NaOH was added dropwise until solution becomes clear. After complete dissolution of paraformaldehyde, solution was cooled down to RT and then filtered. Total volume was adjusted to 25 mL by adding 1X PBS. Dilute HCl solution was added to bring the final pH to 6.9. Solution was stored at 4 °C in the dark.

2.8.6 CLSM Experiments

MCF-7 cells were cultured on 6-well tissue culture plates at a density of 5×10^5 per well in DMEM as described above. 24 h later, cells were treated with $1 \mu\text{M}$ of each nanoparticle group for comparison with the non-treated control group. After 48 h, light group was exposed to white light for 20 min while dark group was kept in incubator. Next day, medium was aspirated, cells were rinsed with PBS three times (5 min each) and fixed 10 min in 4% paraformaldehyde. Fixative was aspirated and cells were rinsed with PBS three times (5 min each) Then cells were permeabilized in 0.1% Triton X-100 for 5 min. After aspirating the Triton, cells were rinsed with PBS three times (5 min each). DAPI stock solution (1 mg/mL) was diluted 1000-fold in PBS and cells were incubated with diluted DAPI solution at RT for 5 min. DAPI was aspirated and cells were rinsed with PBS three times.

Chapter 3

Results and Discussions

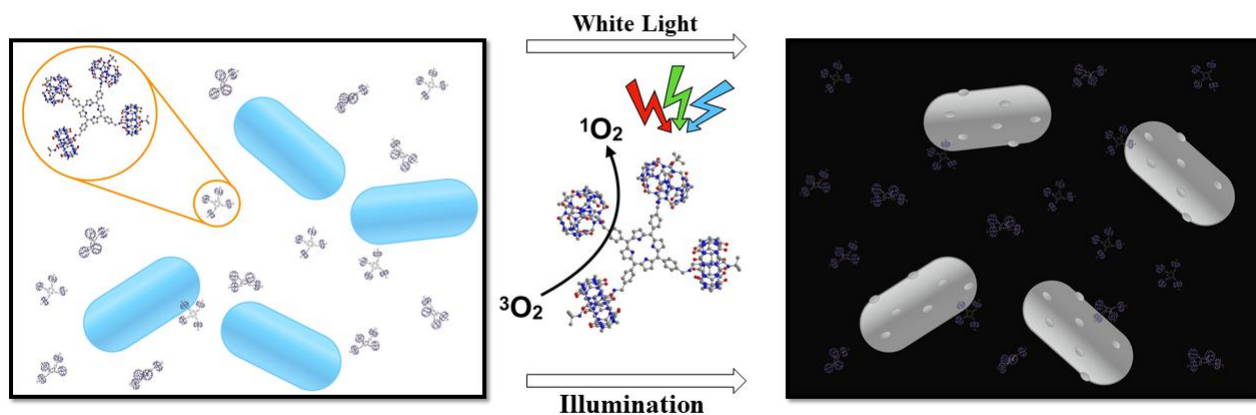
3.1 Introduction

This chapter covers three main sections. In section 3.2, preparation and characterization of porphyrin and CB6-based rotaxane, namely, [5]-rotaxane is discussed. Besides, its ROS generation capacity and utilization of this capacity in photodynamic therapy applications for bacteria and cancer cells are considered. Section 3.3 introduces a supramolecular CB7-porphyrin conjugate (TPP-4CB7) in which CB7 serves as a host receptor to carry anti-cancer drug (DOX). Owing to porphyrin derivative, TPP-4CB7 is also able to generate singlet oxygen in high yield and this multifunctional platform offers effective combined chemo- and photodynamic cancer therapy. In section 3.4, CB7-capped hybrid core-shell nanoparticles based on red-emitting conjugated oligomer and gold is introduced (CB7@COL-Au-NP). Photodynamic and photothermal activities of these nanoparticles against both Gram-positive and Gram-negative bacterial strains are shown. Since they are intrinsically fluorescent, they are exploited in cellular imaging applications as well.

3.2 Cucurbituril and Porphyrin-Based Rotaxane

This work has been partially reported in the publication below [118]:

•M.Özkan, Y. Keser, S.E. Hadi and D.Tuncel, [5]Rotaxane- Based Photosensitizer for Photodynamic Therapy. *Eur. J. Org. Chem.* 2019, 3534-3541.



3.2.1 Aim of the Study

Main objective of this study is to prepare [5]-rotaxane ((**6**)) and employ it as photosensitizer in antibacterial and anticancer PDT. (**6**) was obtained via catalytically self-threading reaction. In this reaction, CB6 behaves as a macrocycle and also catalyst for the catalysation of the 1,3-dipolar cycloaddition reaction between the alkyne-functionalized porphyrin core and azide-substituted stopper groups by forming triazole. Resulting rotaxane is made up of tetraphenyl porphyrin core

which is surrounded by four CB6 molecules and it is therefore called [5]-rotaxane. Tetraphenyl porphyrin was deliberately chosen since porphyrin derivatives are good photosensitizers owing to their high absorption in the visible range of the electromagnetic spectrum, long-lived triplet excited state, high molar extinction coefficient and also their capability of generating singlet oxygen when they are excited by visible light. Application of **(6)** as a photosensitizer in photodynamic therapy against cancer cells and bacteria inactivation was also discussed. **(6)** was found to be highly soluble in water and stable in physiological media pH (7.4) for prolonged time.

3.2.2 Preparation and Characterization of [5]-rotaxane

3.2.2.1 Preparation of 5,10,15,20-tetrakis(α -bromo-*p*-tolyl)porphyrin (TPP-Br) (**3**)

TPP-Br (**3**) was obtained from the condensation reaction of α -bromo-*p*-tolualdehyde (electrophile) and pyrrole (nucleophile) and $\text{Et}_2\text{O} \cdot \text{BF}_3$ catalyzed the reaction as Lewis acid (Figure 3.1). Catalytic activity of $\text{Et}_2\text{O} \cdot \text{BF}_3$ relies on the fact that it increases the electrophilicity of α -bromo-*p*-tolualdehyde rendering it more suitable for nucleophilic attack of pyrrole. Besides, it prevents pyrrole from undergoing self-polymerization reaction. $\text{Et}_2\text{O} \cdot \text{BF}_3$ catalyzed condensation of α -bromo-*p*-tolualdehyde and pyrrole yields a stable intermediate, porphyrininogen. Once porphyrinogen forms, triethylamine (Et_3N) was placed to the reaction mixture for the deprotonation of pyrrolic -NH groups. Then, mixture was treated with tetrachloro-1,4-benzoquinone (TCBQ) to yield **(3)**. **(3)** was obtained with 43% yield.

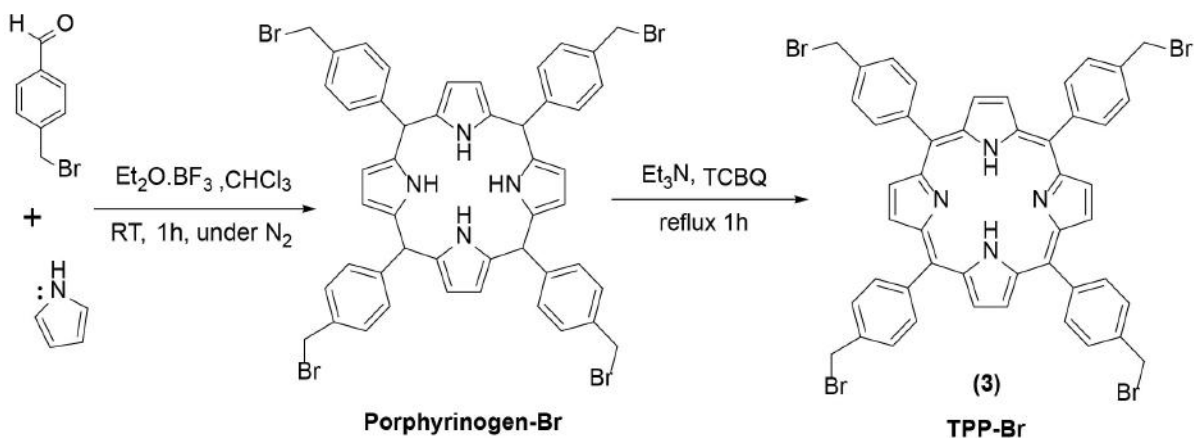


Figure 3.1: Synthetic route for the preparation of TPP-Br.

Structure of **(3)** was only confirmed by $^1\text{H-NMR}$ spectroscopy and shown in Figure 3.2. Its spectrum looks quite clean and all the chemical shifts and integrations were matching with the structure well. Singlet resonance in the upfield region (peak (a) at -2.7 ppm) was assigned to the inner pyrrolic -NH hydrogens and found to be extremely shielded since they are inside the macrocycle. All the other protons of pyrrolic units (b) were chemically equivalent and de-shielded, appearing as a singlet peak at 8.8 ppm. Each of aromatic protons of para-substituted benzene ring (c) and (d) formed doublet peak at 8.2 and 7.8 ppm, respectively. (d) was observed to absorb at higher magnetic field than (c) because the protons (c) were closer to the electron withdrawing porphyrin ring than the protons (d). The singlet at 4.8 ppm was coming from benzylic protons (e). Due to benzene ring adjacent to methylene as an electron withdrawing group, density of σ -electrons around methylene protons is less which makes it more de-shielded than normal alkyl bromide. Integration of this singlet revealed the presence of eight protons confirming that four α -bromo-*p*-tolualdehyde molecules were properly attached to a porphyrin ring.

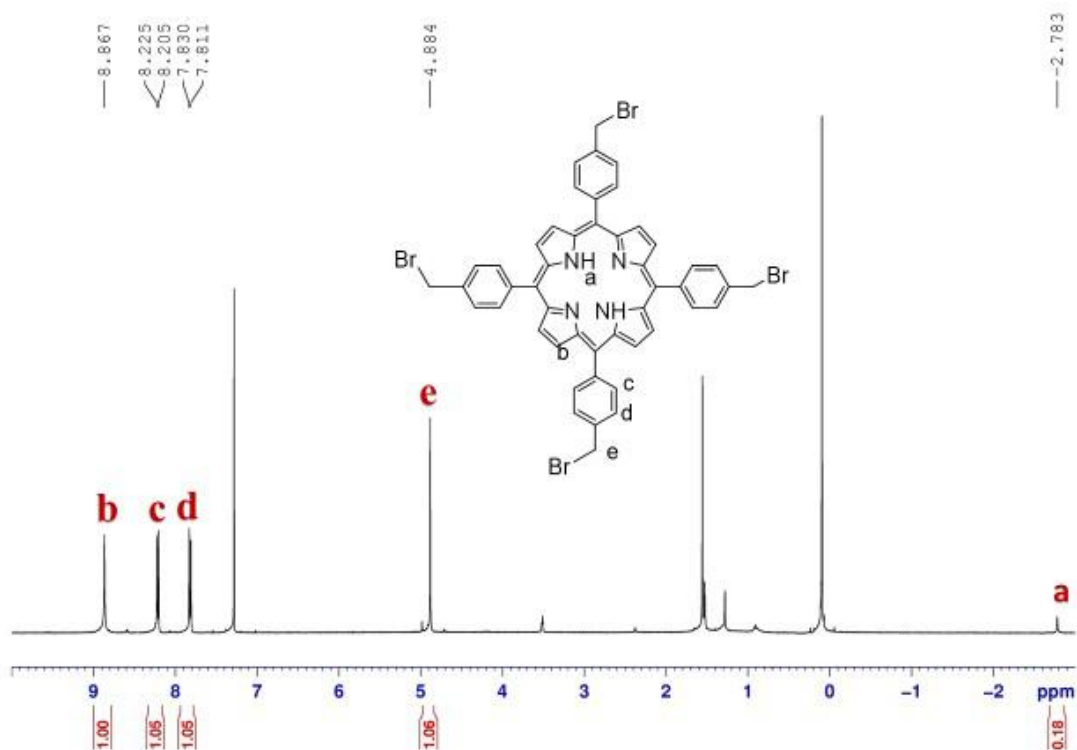


Figure 3.2: ¹H-NMR spectrum of (3) (400 MHz, CDCl₃, 25 °C).

3.2.2.2 Preparation of alkyne-substituted porphyrin (4) and (5)

Once TPP-Br (3) was obtained as precursor, alkyne-substituted porphyrin (4) was prepared through nucleophilic substitution reaction as shown in Figure 3.3. The non-bonding nitrogen of propargylamine electrons attack the benzylic carbon of (3). Bromide is a good leaving group and the hydrogen bromide salt of the propargylamine is expected to form. For the converting of ammonium salt to free base, 0.1 N of NaOH solution was added. After extracting organic phase by CHCl₃, excessive amount of propargylamine was evaporated under reduced pressure. Resulting purple solid was purified by column chromatography to obtain free base (4) in 80% yield.

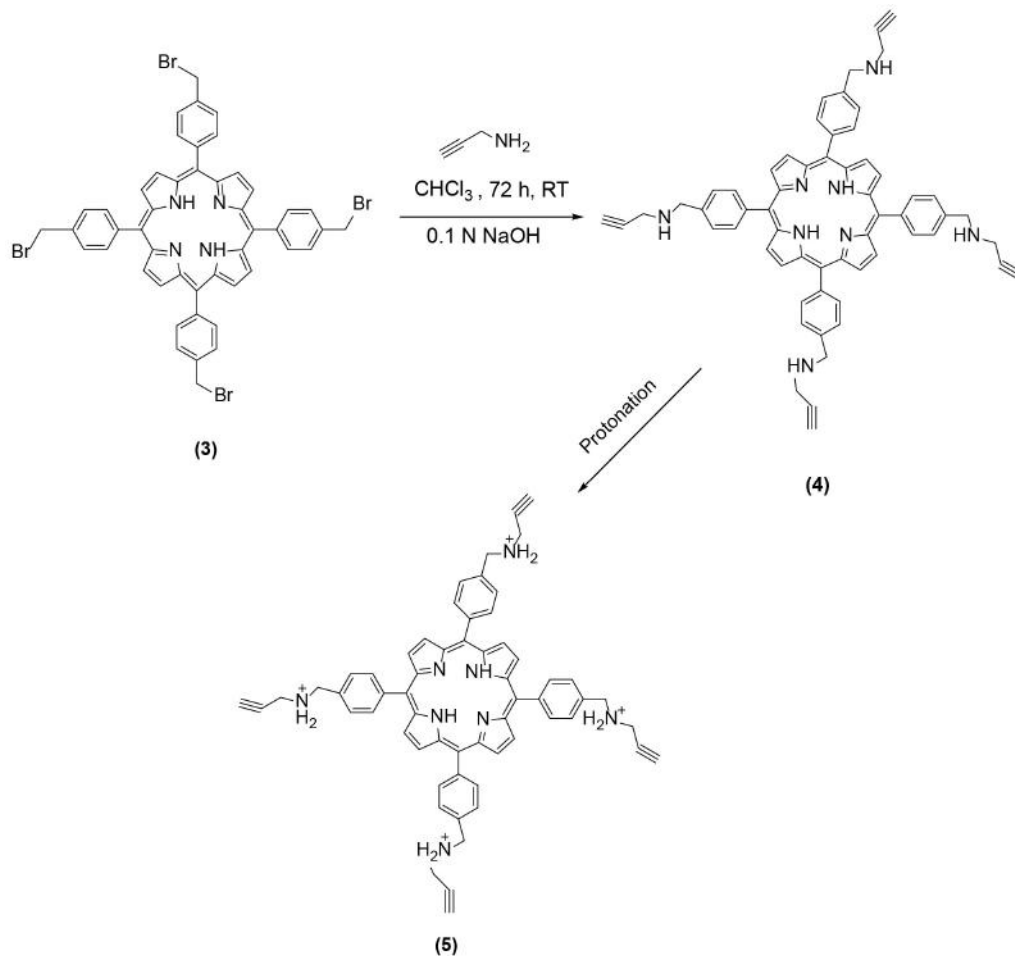


Figure 3.3: Synthetic route for the preparation of alkyne-substituted porphyrin.

Structure of (4) was characterized by ¹H-NMR (Figure 3.4) and ¹³C-NMR (Figure 3.5) spectroscopies and molecular weight of it was analyzed using ESI-MS (Figure 3.6).

The structural characterization of (4) was firstly performed using ¹H-NMR spectroscopy. There were nine different hydrogen environments as expected. At -2.7 ppm, a singlet resonance was assigned as (i) as a result of two aminal protons within the porphyrin ring. The broad singlet at 1.6 ppm (d) came from the protons of the secondary amine. As moving towards downfield region, at 2.4 ppm, triplet was observed (a). From its integration intensity, it is deduced that there are four equivalent terminal alkyne protons indicating that porphyrin core

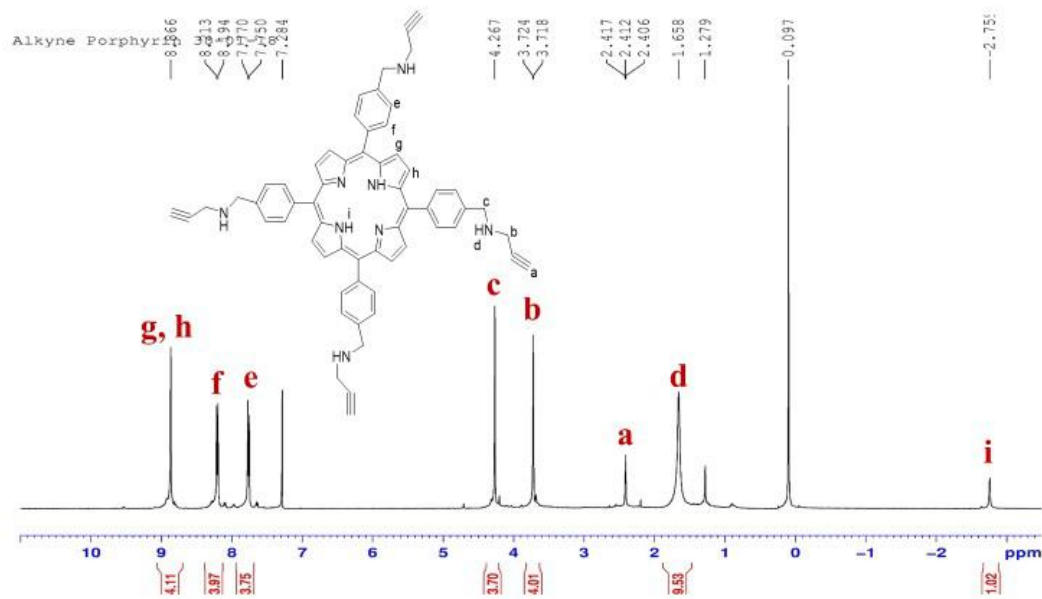


Figure 3.4: ¹H-NMR spectrum of (4) (400 MHz, CDCl₃, 25 °C).

was successfully functionalized by propargylamine. Alternating delocalized π -electrons generate magnetic field and this magnetic field leads to shielding of the protons of the terminal alkyne. Therefore, those protons require higher external field to come in resonance explaining the reason of having a chemical shift in the upfield region. The methylene protons of propargylamine (b) came out as doublet at 3.7 ppm whose integration intensity proves the presence of eight methylene protons. At 4.20 ppm, benzylic protons created a singlet peak (c). Observing higher magnetic field strength for (b) (3.7 ppm) than (c) (4.20 ppm) was expected, since alternating π -electrons of benzene ring creates more de-shielded protons. Absorption of aromatic protons within the para-substituted benzene ring appears in the downfield region at 7.7 (e) and 8.2 ppm (f) as doublets. The most downfield part of the spectrum contains peak at 8.8 ppm caused by non-equivalent -pyrrolic protons of porphyrin ring (g) and (h). ¹³C-NMR spectrum of porphyrin (4) is shown in Figure 3.5. Peaks at 29.7 ppm and 37.8 ppm appeared as a result of aliphatic carbons assigned as (h) and (g) respectively. They are the most shielded carbons of the whole structure. (h) carbon was attached to alkyne whereas (g) is benzylic carbon. Since (h) is closer to the terminal alkyne, it shifts to upfield region more as expected. Other carbon atoms are either included within aromatic

system or non-aromatic system.

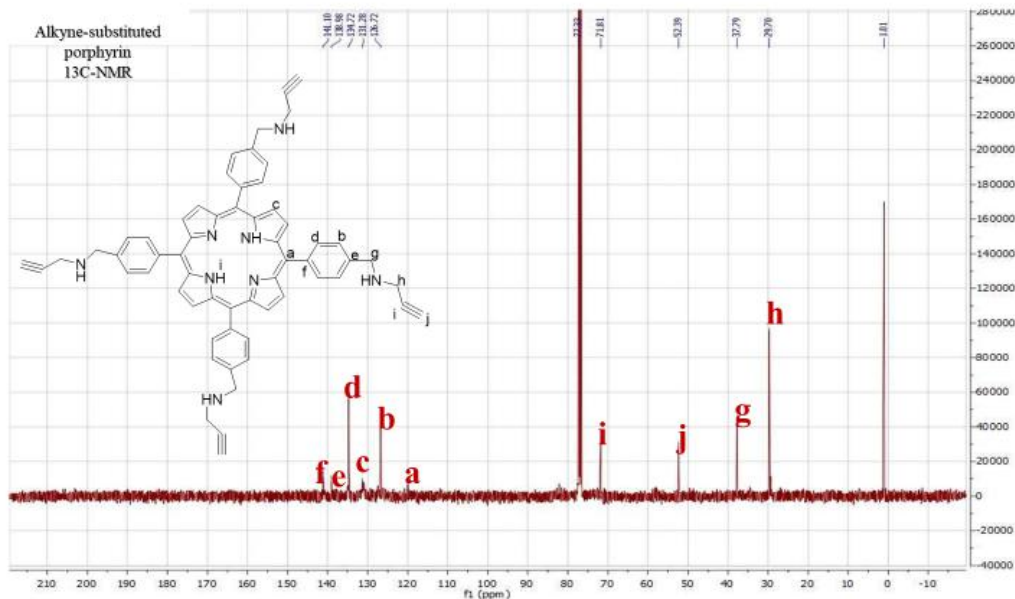


Figure 3.5: ¹³C-NMR spectrum of (4) (CDCl₃, 25 °C).

In Figure 3.6, positive mode ESI-MS spectrum of (4) was demonstrated. Its mass to charge ratio was found to be 883 which was in a good agreement with theoretical values. Theoretically six peaks were expected at m/z : 882.42 (100.0%), 883.42 (64.9%), 884.42 (20.7%), 885.43 (3.5%), 883.41 (3.0%), 884.42 (1.9%).

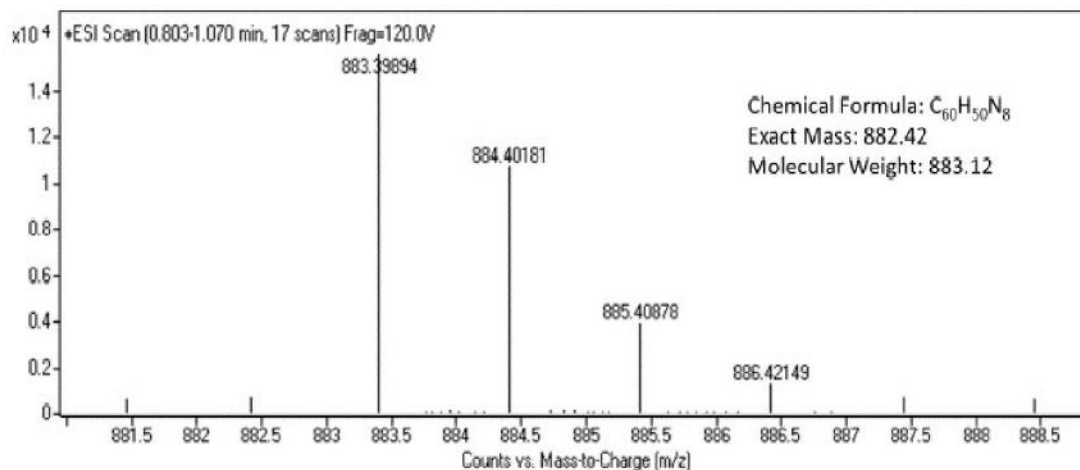


Figure 3.6: +ESI-MS spectrum of (4).

Protonation of (4) with 5 mL of 0.1 N HCl yielded prop-2-ynyl-4-[15-(4-prop-2-ynylaminomethyl-phenyl)-porphyrin5-yl]-benzyl-amine dihydrochloride (5).

3.2.2.3 Preparation of [5]-rotaxane (6)

[5]-rotaxane (6) was synthesized as shown in Figure 3.7. The precursor protonated alkyne-substituted porphyrin (5) (1 equiv.) was dissolved in water, CB6 (4.4 equiv.) and tert-butyl azidoethylammonium chloride (4.4 equiv.) was added to it. The reaction mixture was stirred at RT for 24 h to yield clear green coloured mixture. Then mixture was poured into dialysis tube and dialyzed overnight against water to remove excess CB6 and unreacted monomers. Resulting solution was freeze dried and burgundy powders were obtained in 87% yield.

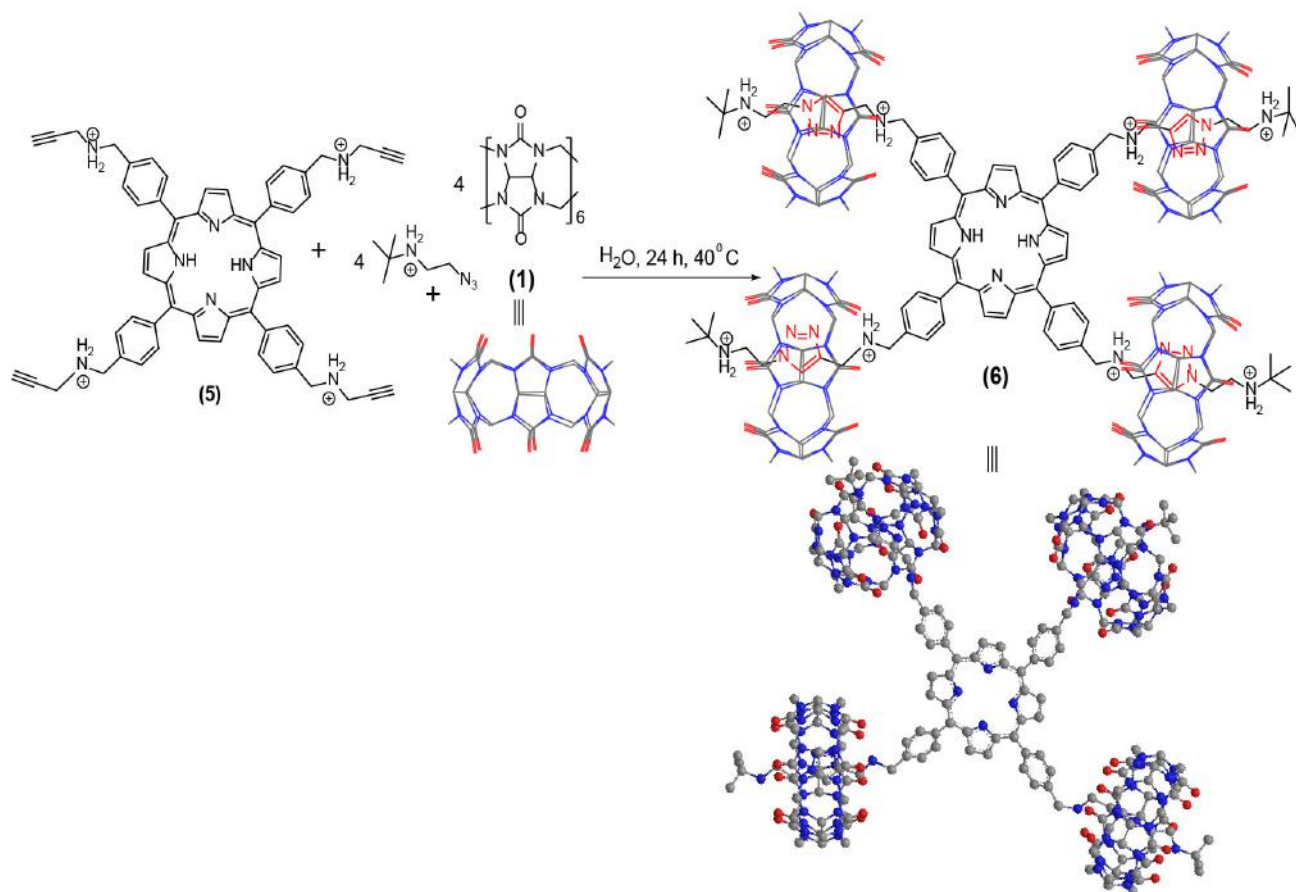


Figure 3.7: Preparation of (6).

(6) was firstly characterized by $^1\text{H-NMR}$ (Figure 3.8). Spectrum appears very clean and peaks are well-matched with the structure of (6). From the sharp and well-resolved peaks, it can be clearly stated that there is no aggregation caused by porphyrin-porphyrin interaction. Those interactions were probably prevented by four bulky (1) surrounding porphyrin core and creating steric hindrance. In the most upfield region of the spectrum, singlet at 1.60 ppm (a) was observed and assigned as tert-butyl protons. On the other hand, protons belonging to ethyl group were found to be as triplets and assigned as (b) at 3.8 ppm and (c) at 4.2 ppm. Aliphatic methylene protons appeared as singlets and assigned as (e) and (f) at 4.4 and 4.9 ppm respectively. Expectedly, aromatic protons gave signals in the downfield region of the spectrum. Singlet at 6.6 ppm (d) is the most important signal of the molecule in terms of the characterization of the compound. Because it comes from the triazole hydrogens proving the formation

of triazole. This observation confirms that 1,3-dipolar cycloaddition reaction was successfully completed between the protonated alkyne substituted porphyrin core (**5**) and azide substituted stopper groups. The protons of para-substituted benzene ring exhibited adjacent doublets at 8.5 (g) and 8.7 ppm (h). The signal occurring as singlet at 9.0 ppm in the most downfield region of the spectrum (i) proved the presence of eight β -hydrogens of porphyrin core.

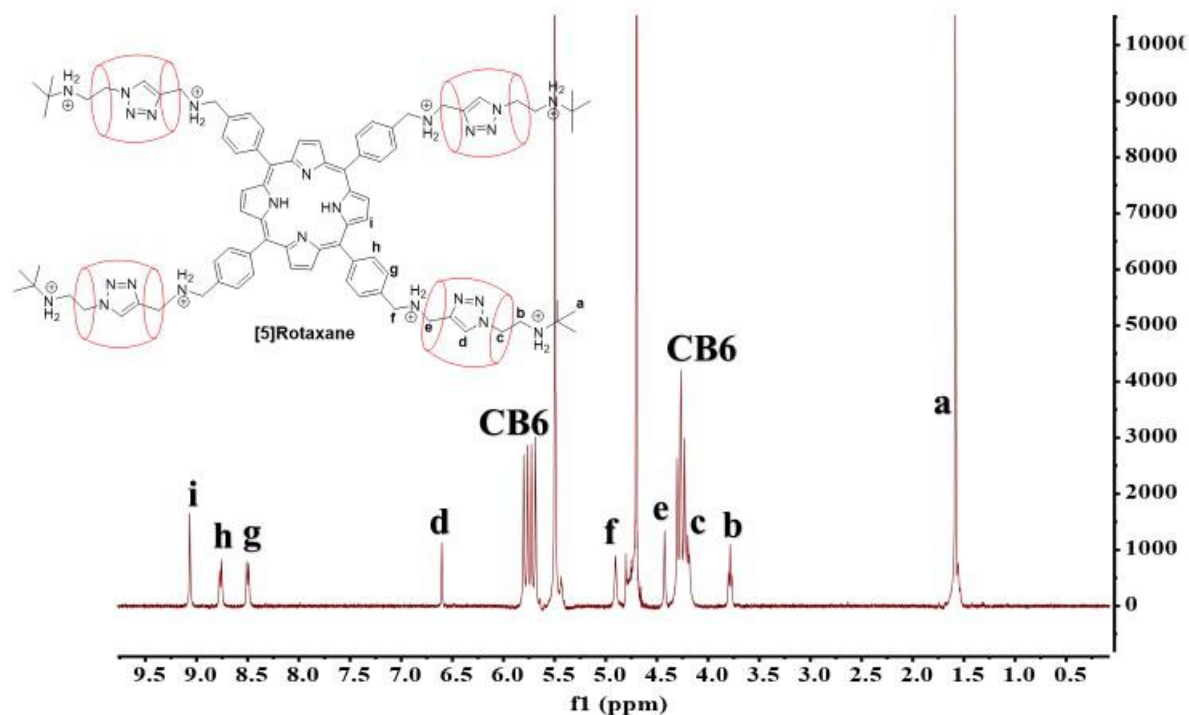


Figure 3.8: ^1H -NMR spectrum of (**6**) (400 MHz, D_2O , 25 $^\circ\text{C}$).

In the FT-IR spectrum of (**6**) (Figure 3.9) no peak was observed at about 2000 cm^{-1} arising from azide functionalization showing the consumption of monomers for the formation of triazole rings. The signals due to carbon-nitrogen stretching of triazole was expected to come at around 1600 cm^{-1} , however they were not obviously observed in the spectrum. The reason behind this might be the overlapping between the $-\text{C}=\text{O}$ peak of the (**1**) at around 1800 cm^{-1} since triazole groups were encapsulated within the cavity of (**1**). O-H stretch was seen in the spectrum because (**6**) was dissolved in water.

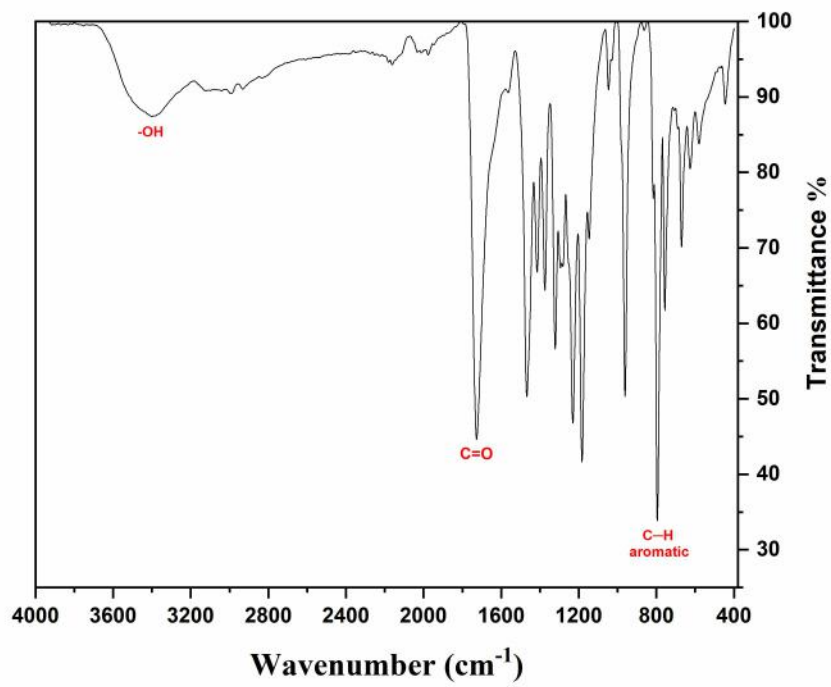


Figure 3.9: FT-IR spectrum of (6).

ESI-MS spectra of (6) were given below in Figure 3.10 for hydrogen and sodium adduct.

Calculated for $C_{228}H_{258}Cl_8N_{120}O_{48}$; Mass: 5730.964

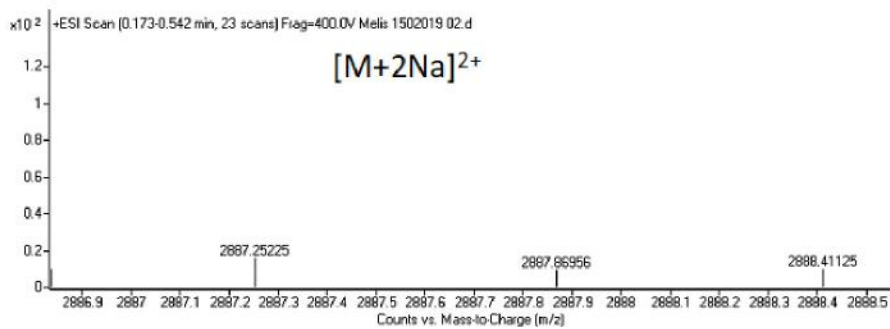
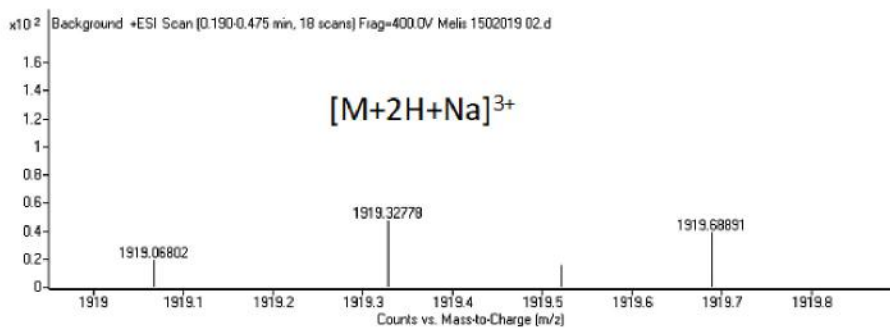
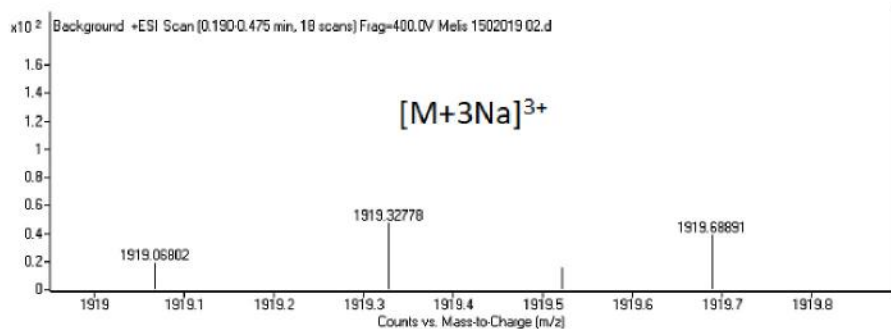
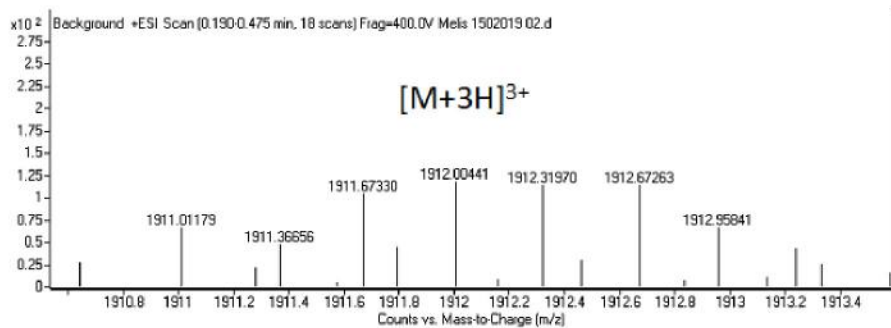


Figure 3.10: ESI-MS spectrum of (6).

Once the structure and molecular weight of the desired (**6**) were verified, its photophysical properties and ability to be employed as a photosensitizer were examined. In the Figure 3.11 the UV-vis absorption and fluorescence spectra of (**6**) at the concentrations of 5, 10 and 20 μM in water were demonstrated. A sharp Soret band (λ_{max} at 415 nm) and four weak Q-bands (at 517, 553, 582, and 636 nm) in the spectrum exhibits the characteristic absorption peaks of free base porphyrins. It was clearly deduced that the presence of four bulky (**1**) groups prevented the interactions between porphyrin units and consequently, aggregate formation was averted as in the case of $^1\text{H-NMR}$ spectrum. Besides, the photophysical properties of porphyrin core was well-maintained in water. The excitation of (**6**) in aqueous media at 415 nm gave fluorescence emission above 600 nm as characteristic feature of porphyrin core with two vibrational bands at 646 and 707 nm (Figure 3.11). As shown in the PL spectrum, as the concentration of (**6**) increases, its emission intensity decreases and self-quenching due to short-range interactions between the fluorophores might be the cause of this observation.

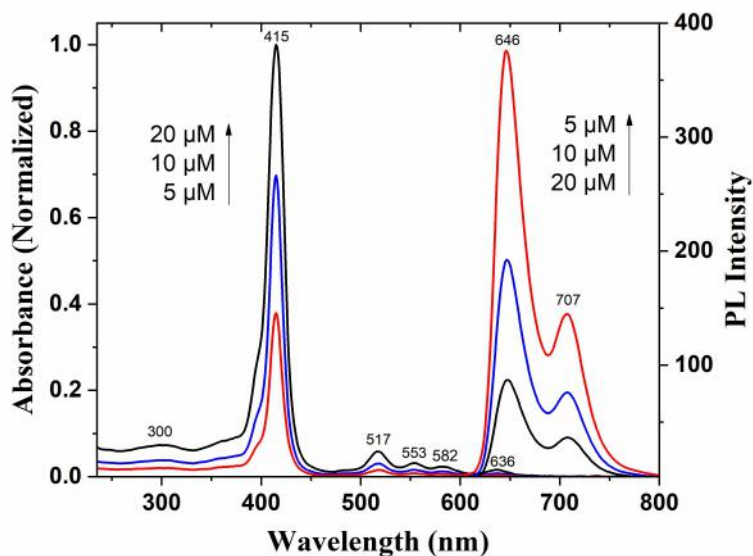


Figure 3.11: UV-vis absorption and fluorescence spectra of (**6**) in water at the concentrations of 5, 10 and 20 μM .

Fluorescence quantum yield and life time of (**6**) were recorded as 10% and 7.5

ns, respectively in water ($5 \mu\text{M}$) (Figure 3.12).

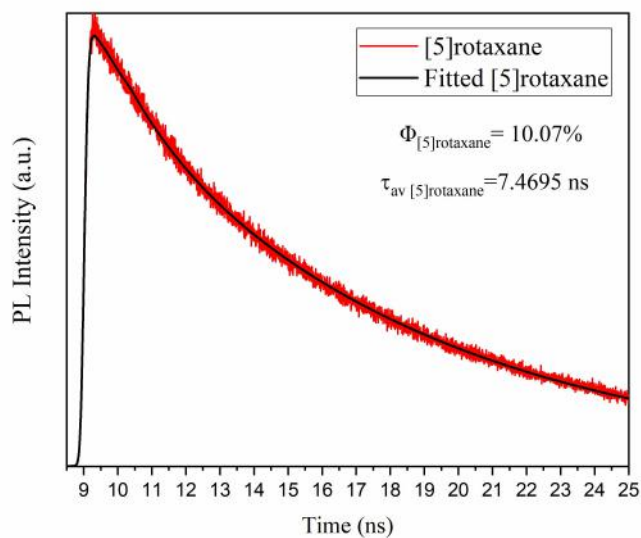


Figure 3.12: TRF measurement of (6).

3.2.3 Evaluation of ROS Generation Performance of (6)

Light-induced reactive oxygen species (ROS) generation capacity of photosensitizer (6) was evaluated by using a probe, 2,7-dichlorofluorescein diacetate (DCFH-DA). 2,7-dichlorofluorescein (DCFH) was obtained by a hydrolysis of DCFH-DA in the alkaline medium which is quite sensitive to ROS and could be rapidly converted into highly fluorescent 2,7-dichlorofluorescein (DCF) (Figure 3.13) resulting in considerable rise of the fluorescence intensity at 524 nm.

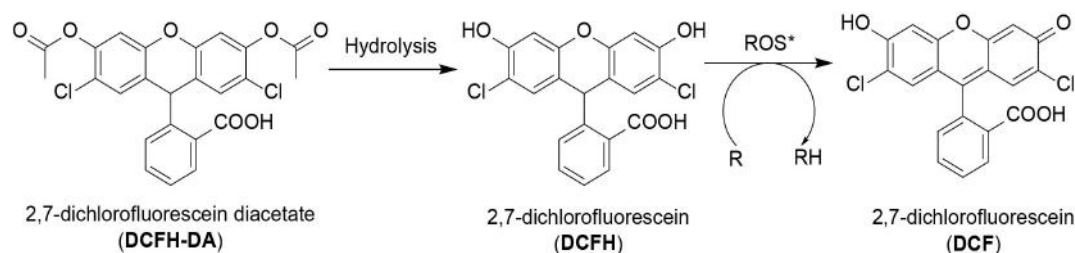


Figure 3.13: Molecular structures of 2-7 Dichlorofluorescein diacetate (DCFH-DA), 2,7-dichlorofluorescein (DCFH) and the reaction of DCFH with ROS to yield highly fluorescent 2,7-dichlorofluorescein (DCF).

As given in Figure 3.14a, ROS generation performance of **(6)** was probed by exposing to the white light having intensity of 1 mW/cm². Once only DCFH was illuminated (without **(6)** addition), very weak emission band at 524 nm was seen caused by the autooxidation of DCFH to DCF. Addition of **(6)** to the solution before irradiating with white light did not affect the intensity of peak at 524 nm and it was corrected as blank for four minutes as shown in Figure 3.14b. However, upon exposing to the white light, the peak intensity increased significantly and continuously. Within four minutes, intensity of the peak reached to 1000. These findings reveal that **(6)** possess a remarkable light-activated ROS production ability.

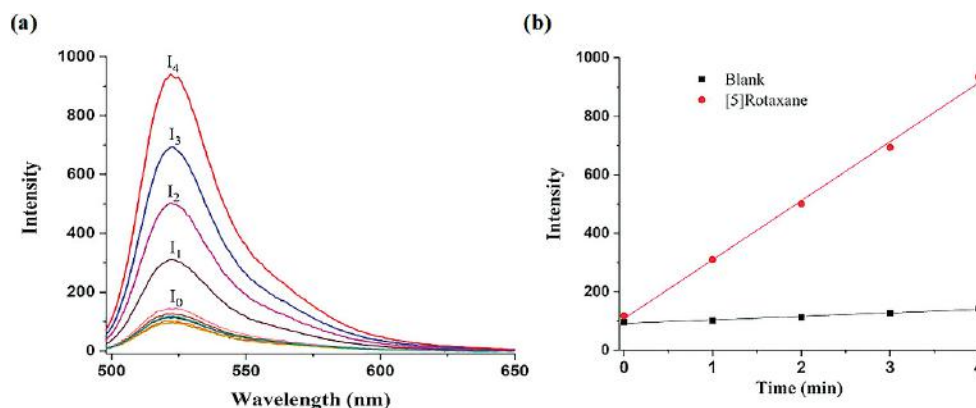


Figure 3.14: (a) Fluorescence intensity of DCF at 524 nm as blank and in the presence of 5 μM of **(6)** under continuous white light illumination. I₀, I₁, I₂, I₃, I₄ correspond to blank and white light irradiated duration for 1, 2, 3, 4 minutes measurements, respectively. (b) Time response curve of DCFH oxidation in the presence of **(6)** and without **(6)** (R² = 0.986 for blank, R²=0.9976 in the presence of **(6)**).

3.2.4 Examination of Cytotoxicity and Phototoxicity on *E. coli* and *B. subtilis*

After revealing that **(6)** is able to produce ROS in a high yield, as the next step, its light-induced biocidal activity was examined. To this end, *E. coli* (gram-negative bacteria) was chosen as representative organisms since they account for the great majority of the infectious diseases. In order to be able to consider **(6)** as broad-spectrum antibacterial agent, *B. subtilis* (gram-positive bacteria) was also regarded. Interactions between **(6)** and *E. coli* and *B. subtilis* were studied. Firstly, to find out the optimal concentration range of **(6)** for the inactivation of *E. coli*, minimum inhibitory concentration (MIC) value was determined in the dark (Figure 3.15) and upon white light irradiation with the flux of 22 mW/cm² (Figure 3.16 and 3.17) treating *E. coli* with the concentrations varying from 0.5 μ M to 4.7 μ M. After keeping **(6)**-treated bacteria and non-treated control group under light and in the dark, their optical density at 600 nm (OD₆₀₀) was measured. From the OD₆₀₀ data, information about the growth of microorganisms is obtained. It is type of turbidity measurement and measures the scattered light based on absorbance detection mode. The more bacteria are present in the solution, the more light will be scattered by them. MIC value is defined the lowest concentration of an antimicrobial agent preventing visible growth of microorganism. MIC determination experiments to reveal the effect of **(6)** dosages on the inhibition efficiency toward *E. coli* in the dark did not play important role. That is, there is no significant difference between the effect of 0.5 μ M and 4.74 μ M of **(6)** in the dark. This observation was expected since as a photosensitizer, **(6)** is activated by light illumination. On the other hand, under photoirradiation, results indicated that the antimicrobial efficiency was considerably enhanced as concentration of **(6)** increases and reaches a plateau after 3.5 μ M which was determined as MIC value of **(6)** on *E. coli*.

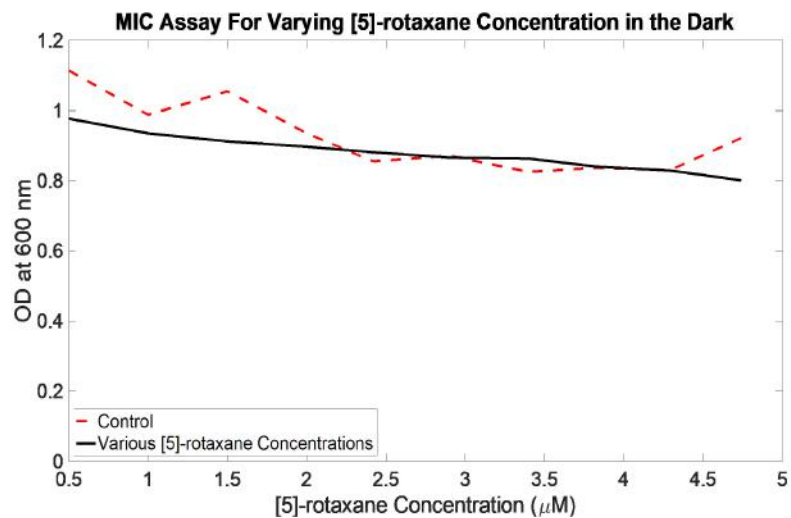


Figure 3.15: MIC Assay for (6): concentrations between 0.5 μM and 4.74 μM in the dark.

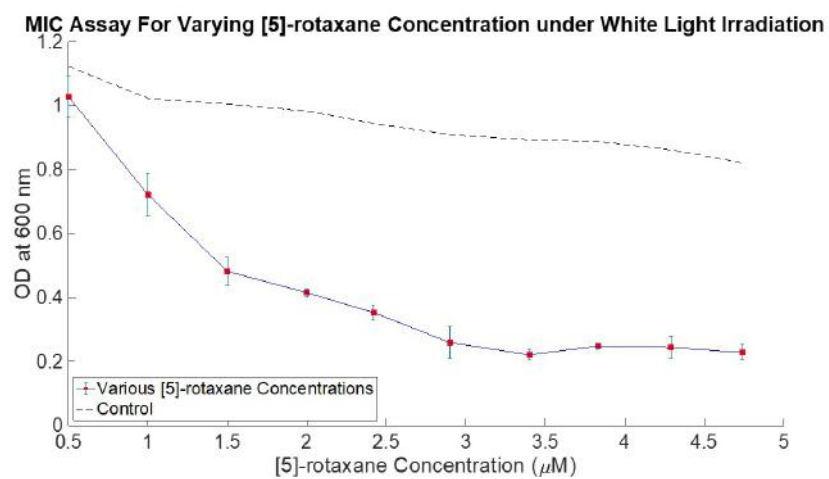


Figure 3.16: MIC Assay for (6): concentrations between 0.5 μM and 4.74 μM under white light irradiation (22 mW/cm^2).

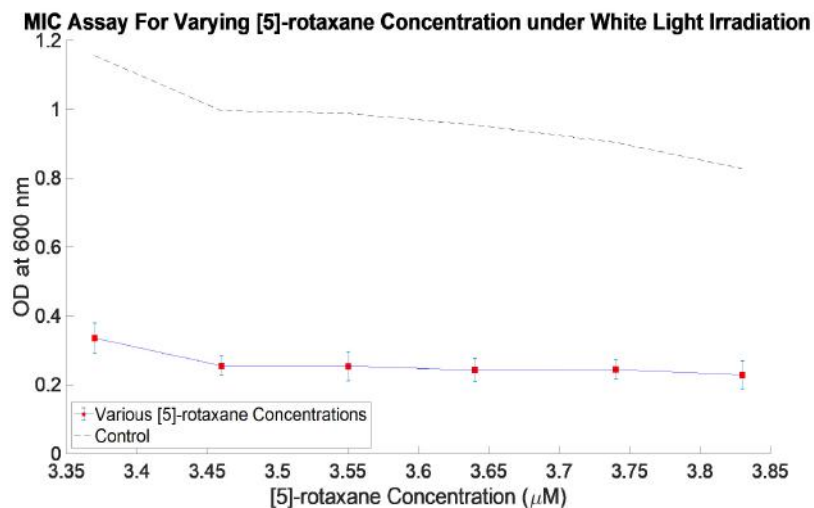


Figure 3.17: MIC Assay for **(6)**: concentrations between 3.37 μM and 3.83 μM under white light irradiation (22 mW/cm^2).

After determining MIC value as 3.5 μM , bacterial survival experiments were performed in the dark and upon exposure to white light for 1 min. with flux of 22 mW/cm^2 by a surface plating method. (Figure 3.18 c-f). Quantification of colony forming units demonstrated that the killing efficiency upon irradiation of *E. coli* suspension treated with 3.5 μM of **(6)** was reported 96%, while the inhibition percent in the dark was only around 9% (Figure 3.18 b). The values were represented as the mean \pm standard deviation (SD) of six replicates. Error bars represent SD of data from six separate measurements.

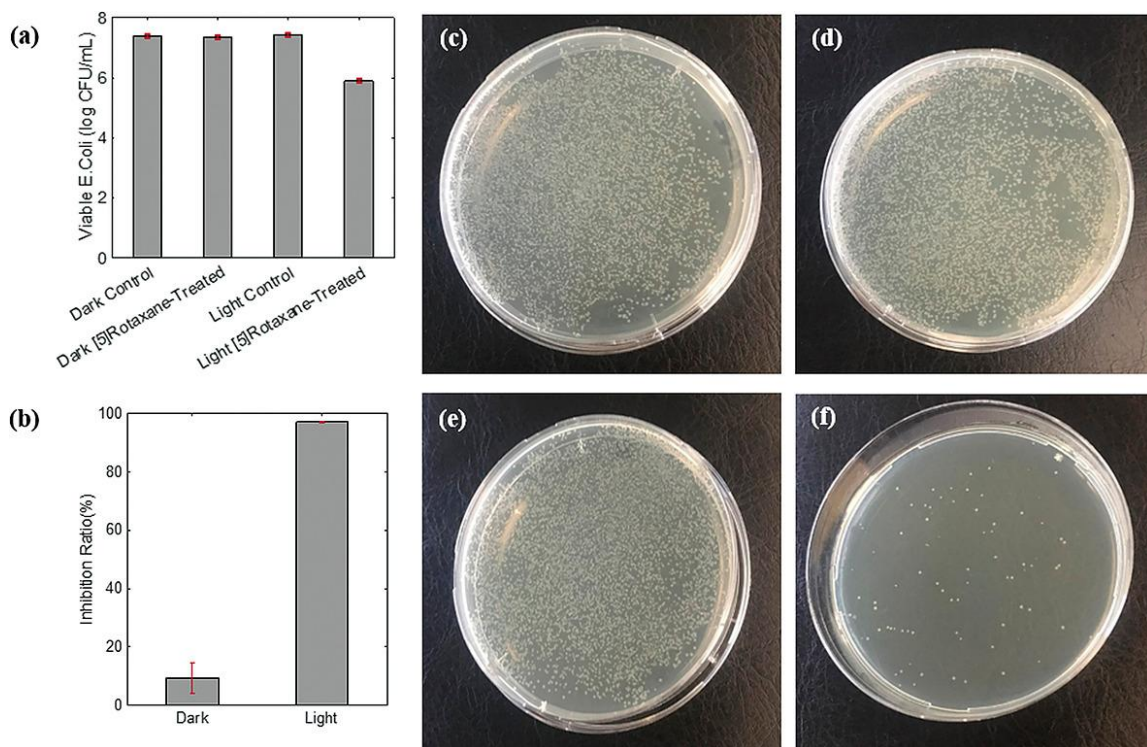


Figure 3.18: (a), (b) Bacterial killing performance of **(6)** toward *E. coli* in the dark and under light exposure. Plate photographs for *E. coli* on YTD agar plate treated (c) control in the dark, (d) **(6)**-treated in the dark, (e) control under light exposure (1 min, 22 mW/cm²) (f) **(6)**-treated under light exposure (1 min, 22 mW/cm²).

Antibacterial activity of protonated alkyne porphyrin **(5)** which is the core of **(6)** (without CB6), on *E. coli* in the dark and under photoirradiation exposing the same conditions that are, 3.5 μ M of **(5)**, 22 mW/cm² white light exposure for 1 min was also tested to understand the effect of CB6. **(5)** exhibited inhibitory effect around 60% and 70%, in the dark and under light, respectively (Figure 3.19 and 3.20). High dark toxicity of **(5)** in comparison to **(6)** was caused by the strong electrostatic interactions between the ammonium groups with bacterial cell walls and addition of the hydrophobic part of the porphyrin monomer through hydrophobic interactions. Another hindrance related to **(5)** was its poor solubility in PBS. In **(6)**, ammonium groups coordinate with the carbonyl portals of **(1)** providing interactions with bacterial cell walls.

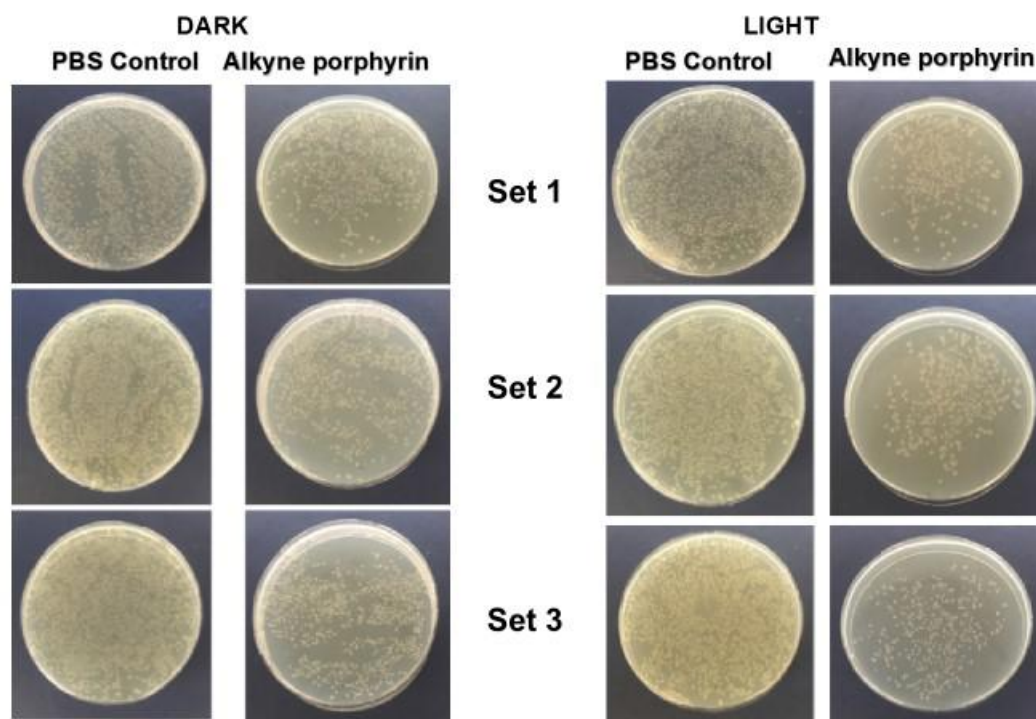


Figure 3.19: Plate photographs for *E. coli* on YTD agar plate treated with 3.5 μM of (5) and non-treated control in the dark (left panel) and under light (right panel).

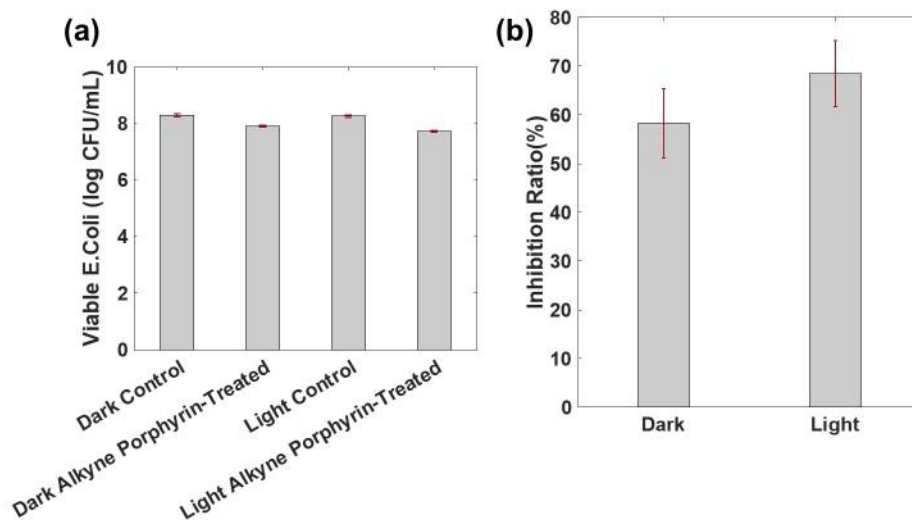


Figure 3.20: Biocidal activities of (5) against *E. coli* in the dark and under white light illumination.

The light-triggered antimicrobial activities of **(6)** toward the Gram-positive bacteria (*B. subtilis*) was also analyzed keeping the same experimental conditions. Almost 100% killing efficiency was achieved upon light illumination whereas it was only 7% in the dark. (Figure 3.21 and 3.22). These observations suggest that **(6)** has a potential to be employed as a broad-spectrum antibacterial agent.

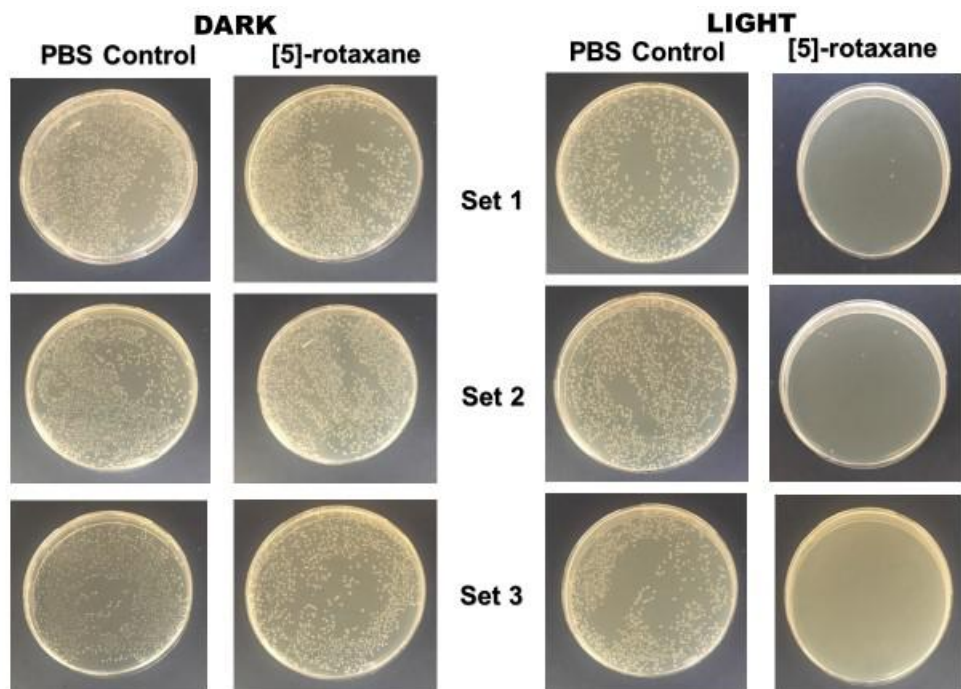


Figure 3.21: Plate photographs for *B. subtilis* on YTD agar plate treated with 3.5 μM of **(6)** and non-treated control in the dark (left panel) and under light (right panel).

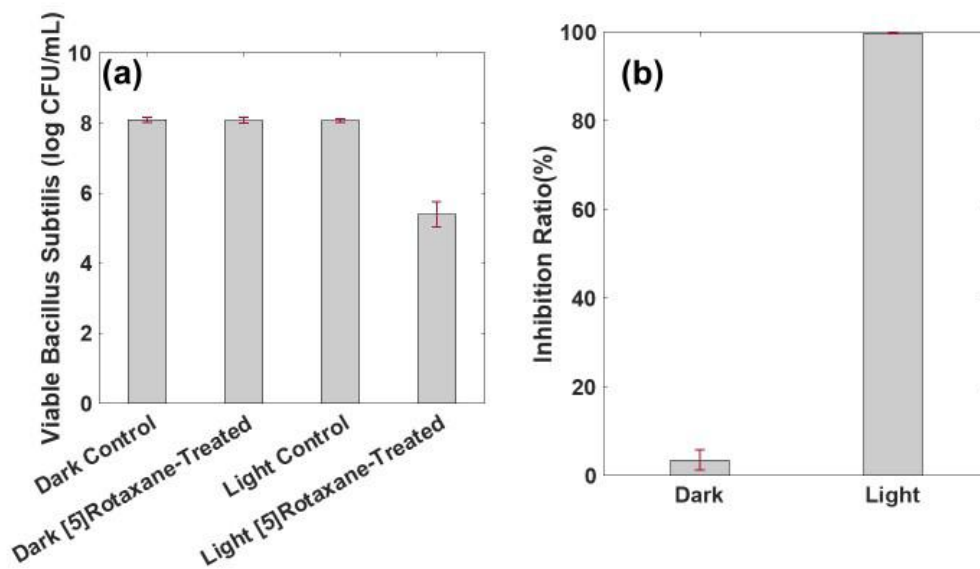


Figure 3.22: Biocidal activities of (6) against *B. subtilis* in the dark and under white light illumination.

Interactions between (6) and bacteria was further investigated by scanning electron microscopy (SEM) and zeta potential measurements. SEM is reliable technique to examine the morphology of bacteria interacted with any antibacterial agent. SEM images of *E. coli* incubated with 3.5 μM of (6) in dark and under light were captured. Below, Figure 3.23 b indicates *E. coli* cells treated with (6) in the dark along with its control group (Figure 3.23 a). From the images, it is clear that in the dark, vast majority of the *E. coli* were in rod-like shape and not affected (6). Their cell walls preserved their smooth surfaces as opposed to light-exposed case. SEM images of light-exposed group revealed that the surface of bacteria treated with (6) (Figure 3.23 d) were collapsed. Their membranes were observed to be ruptured and damaged compared to that of control group (Figure 3.23 c).

SEM pictures verified that (6) is able to destroy the bacterial outer membrane only when exposed to light but not in dark. These findings were also in good agreement with antibacterial experiments. Despite the fact that (6) has cationic nature with many ammonium ions leading to dark toxicity due to strong

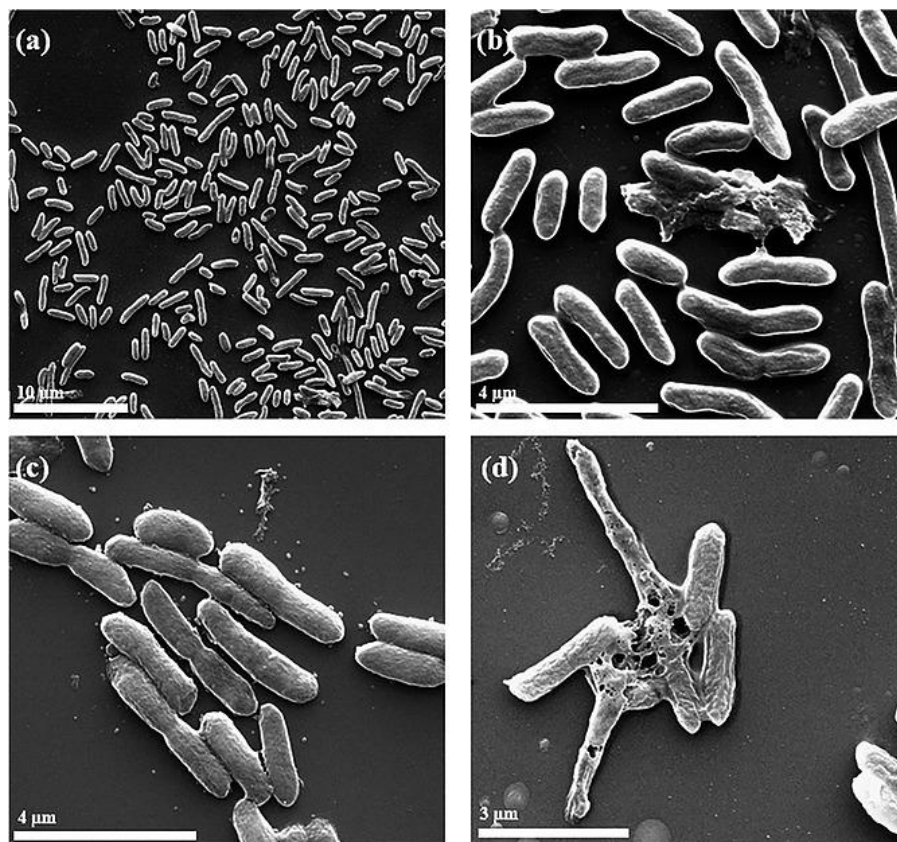


Figure 3.23: SEM images of *E. coli* (a) control in the dark, (b) 3.5 μM of **(6)**-treated in the dark, (c) control under photoirradiation (d) 3.5 μM of **(6)**-treated under photoirradiation.

electrostatic interaction between positive charges and *E. coli*, **(1)** disguised them through the formation of ion-dipole complexes which decrease the dark cytotoxicity. However, **(6)** was still able to interact with bacteria with weaker binding and found to be accumulating on the surfaces. Upon light-excitation ROS were produced and destroy the bacterial membrane as can be observed from the SEM pictures.

As a last proof, binding of **(6)** to bacteria was shown by ζ -potential measurements. When bacterial suspensions were incubated with **(6)**, positive ζ -potential shifts were obtained from 45.7 to 33.3 mV in the dark and from -50.3 to -22.9 mV upon light exposure (Figure 3.24).

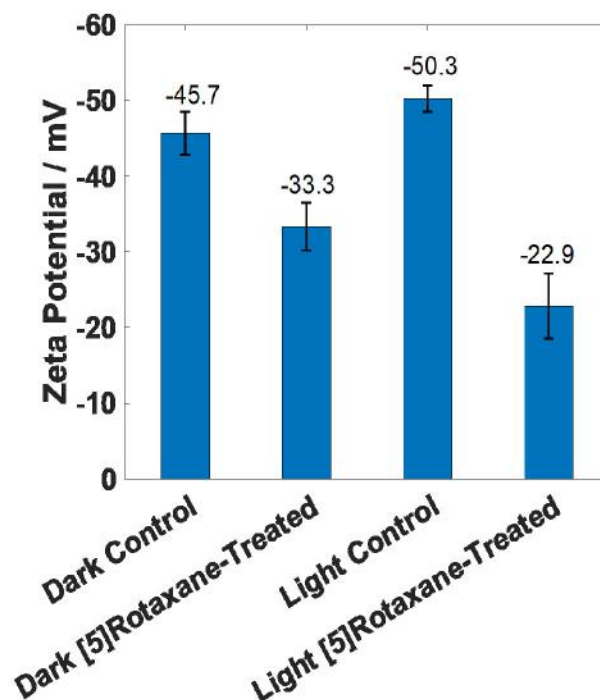


Figure 3.24: ζ -Potentials of *E. coli* incubated with $3.5 \mu\text{M}$ of **(6)** in water at 25.0°C in the dark and under light.

3.2.5 Examination of Cytotoxicity and Photocytotoxicity on the MCF-7 Cell Line

MTT assay was used for the determination of the cytotoxicity of **(6)** on mammalian cells *in-vitro*. To this end, MCF-7 was selected as a modal breast cancer cell line and incubated with the various dosages of **(6)** in dark and under photoirradiation. Based upon the dark cytotoxicity test, concentrations of **(6)** between $10\text{-}300 \mu\text{M}$ along with the non-treated DMEM control group were used for the determination of cytotoxicity of **(6)**. **(6)** did not exhibit any significant cytotoxicity on MCF-7 cells between control group and any of the concentrations used ($P=0.0653$) and had high cell viability. This observation confirmed the safety of **(6)** for mammalian cells in dark even at $300 \mu\text{M}$ which is much higher than that used for inactivation of bacteria (Figure 3.25 a). Photodynamic performance of **(6)** on MCF-7 was determined by exposing MCF-7 cells to the white light

(20 mW/cm²) with various exposure times (5, 10 and 15 min) and various concentrations of **(6)** (2-100 μ M). In opposition to dark case, MCF-7 cells showed significant decrease in relative cell viability upon light excitation. As given in Figure 3.25 b, significant cell viability decrease was recorded even at 2 μ M of **(6)** for the 10 min of light exposure when compared with the DMEM control group (P<0.0001). These findings supported that white light activated **(6)** well. As a result, the cell viability even at low concentrations were successfully reduced with the same rate of decrease reported at high concentrations. Significant cell viability reduction for the **(6)**-treated groups showed that the potential superiority of anti-tumorigenic activity upon light exposure. For that reason, employing **(6)** under light is considered as safe strategy to eliminate high cytotoxicity related side effects.

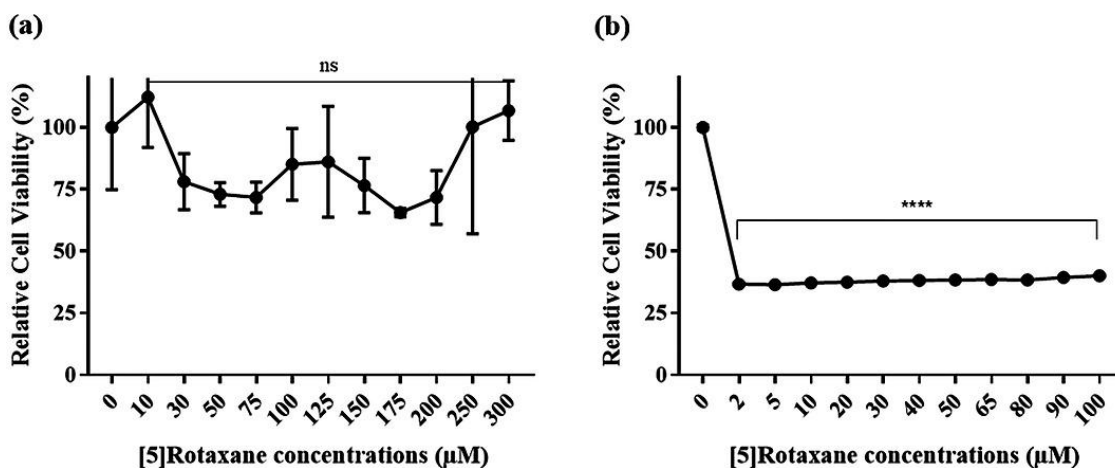
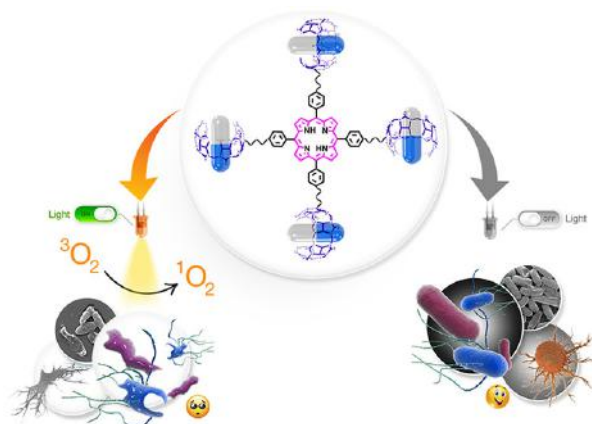


Figure 3.25: Relative cell viability for MCF-7 incubated with 2-100 μ M of **(6)** upon normalization with DMEM control group (a) in dark (P=0.0653) and (b) upon white light irradiation (10 min, 20mW/cm²) (P<0,0001).

3.3 Supramolecular Cucurbituril-Porphyrin Conjugate

This work has been partially reported in the publication below [119]:

•M.Özkan, Y.Kumar, Y.Keser, S.E. Hadi and D.Tuncel, Cucurbit[7]uril-Anchored Porphyrin-Based Multi-Functional Molecular Platform for Photodynamic Antimicrobial and Cancer Therapy. *ACS Appl. Bio Mater.* 2019, 2, 11, 4693-4697.



3.3.1 Aim of the Study

Herein, multifunctional photoactive supramolecular assembly was built through covalent linkage of four cucurbit[7]uril (CB7) (**2**) molecules functioning as receptor to porphyrin core using suitable linkers. Since this assembly was made up of tetraphenyl porphyrin (TPP) derivative and four CB7, it was abbreviated as TPP-4CB7 with the compound number of (**7**). In Figure 3.26, synthetic route for the preparation of (**7**) was shown.

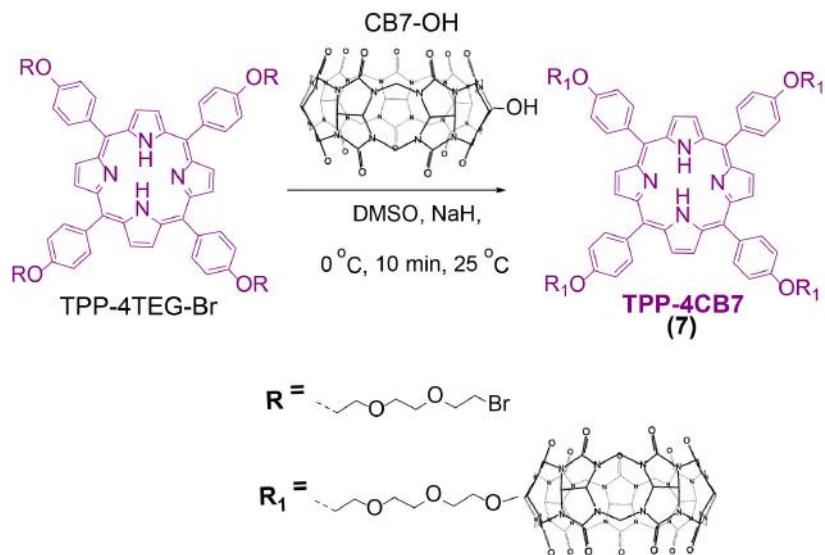


Figure 3.26: Synthetic route for the preparation of **(7)**.

(7) is a supramolecular platform serving very efficiently as light-activated broad-spectrum antibacterial agent and possess minimal dark cytotoxicity just like **(6)**. In addition to its antibacterial effect, here, main objective was to combine chemo- and photodynamic cancer therapy using **(7)** which makes this study novel. Presence of host molecules **(2)**, enables this system to be utilized as a vehicle to carry drug molecules. Since the photodynamic inactivation of bacteria mechanism using **(7)** is quite similar to that of **(6)** as both of them has porphyrin derivative as photoactive core, related discussion will not be mentioned here but can be found in detail in the given publication.[119] Herein, novel part of study which is implementation of **(7)** as drug carrier and combined chemo- and photodynamic therapy aspects will be highlighted.

3.3.2 Utilizing **(7)** as Drug Delivery Vehicle and Combination of Chemotherapy and PDT

After preparing **(7)** whose antibacterial activity was switched on upon light irradiation but switched off in the dark, its cytotoxicity and photocytotoxicity in

vitro was analysed using the concentrations between 1-100 μM . The findings revealed that (7)-treated MCF-7 cells in dark possessed high cell survival rate with half maximal inhibitory concentration value (IC_{50}) of $> 100 \mu\text{M}$. For determining the photocytotoxicity of (7), (7)-treated MCF-7 cells (1-100 μM) were exposed to white light with the flux of $20 \text{ mW}/\text{cm}^2$ for 5 min. Around 25% reduction in cell viability was reported at the minimum concentration (1 μM) in comparison to non-treated DMEM control group ($P < 0.0001$). As the dosage of (7) was increased, the cell viability decreased gradually. Half of the MCF-7 cells were inactivated even at relatively low concentration (5.5 μM) (Figure 3.28) Inactivation rate was found to reach to over 90% for the maximum concentration (100 μM). These findings clearly prove that even at minimal dosages, (7) was activated efficiently by white light resulting in considerable reduction in the cell survival rate. The results further confirm that (7) can be employed as an ideal photosensitizer having negligible dark cytotoxicity and it was activated only when excited by light.

Benefitting from the presence of host molecules (2) in the structure of (7) which enable host-guest chemistry, the next rational strategy was to exploit this supramolecular assembly as a drug carrier. In this context, an anticancer drug, doxorubicin hydrochloride (DOX) was chosen as a modal anticancer agent since it is known to prevent the growth of cancer cells by blocking topo isomerase. Before testing (7)+DOX complex *in vitro*, interactions and complex formation mechanism between (2) and DOX was experimentally investigated. $^1\text{H-NMR}$ spectrum of (7) with DOX was recorded, however it was not helpful since spectrum was mainly dominated by the peaks coming from (2). It was due to the fact that each (7) was including four (2) units. Therefore, $^1\text{H-NMR}$ spectra of DOX with (2) was also recorded. The resulting spectrum was similar to those reported in the literature. No significant shifts for DOX protons was observed when encapsulated by (2) showing the low binding constant of complexation. In the recent studies, it was suggested based on computational modeling that $-\text{NH}_2$ and $-\text{OH}$ groups of DOX molecule undergo complexation with the carbonyl portal of (2) via hydrogen bonding. [124] To investigate (2) and DOX binding further, isothermal titration calorimetry (ITC) was performed (Figure 3.27) in

the DMEM medium which was also used for the cell viability experiments. The results were not completely successful but still gave some insights. The binding stoichiometry was found to be 1:0.85 with a binding constant of $7.36 \times 10^5 \pm 2.45 \times 10^5 \text{ M}^{-1}$. Even though each (7) owns four (2) units, in this study, the amount of DOX used was kept limited with a maximum ratio of (7) to DOX (1:1.5). This shows that probably one DOX formed complex with more than one (2) unit of (7) leading to slow release of DOX.

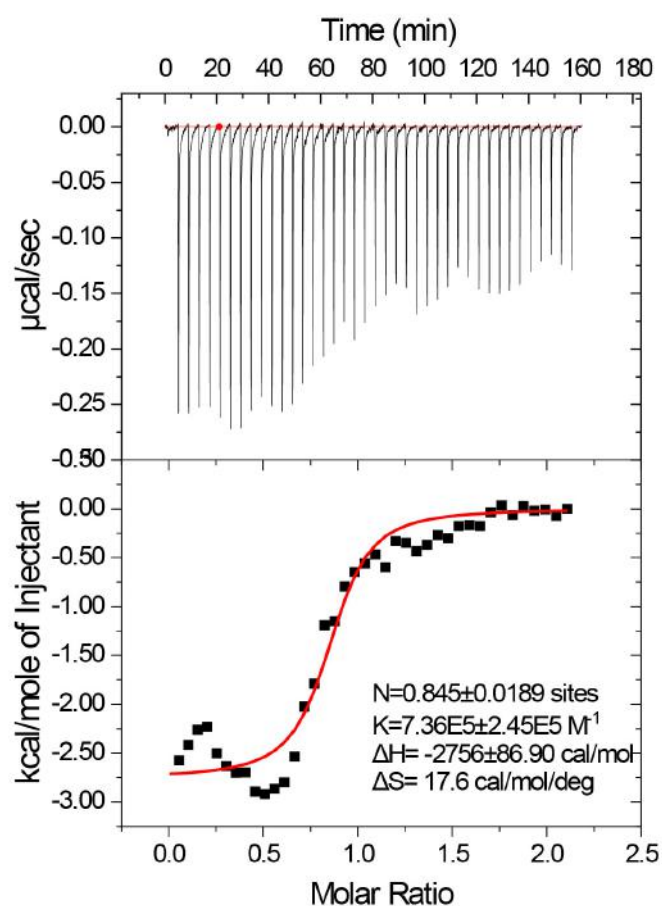


Figure 3.27: Isothermal Titration Calorimetry (ITC) data for the complexation of (2) and DOX.

For the evaluation of suitability of **(7)** to be used as drug delivery vehicle and for investigation whether it can be utilized for dual chemo and photodynamic therapy, **(7)**+DOX complexes were obtained by stirring DOX with **(7)** in DMEM medium. MCF-7 cells were treated with various dosages of **(7)**, DOX and **(7)**+DOX in dark and under light irradiation for 96 h. In MCF-7 cells incubated with only DOX, concentration-dependent reduction in cell viability was observed and light exposure had no significant effect on the toxicity of DOX (Figure 3.28 a, b). From the Figure 3.28, it can be clearly stated that DOX exhibited slightly less inhibitory effect upon complexation with **(7)** in the light. This observation probably stems from the strong interactions of DOX with **(2)** providing slow release. This might be particularly desired when slow and sustained release of drugs are targeted. On the other hand, 50% inactivation of MCF-7 was achieved under white light illumination upon complexation of 10 μM DOX and 4 μM **(7)** in comparison to 50% inactivation observed for DOX and **(7)** individually at the doses of 20 μM and 5.5 μM , respectively. Furthermore, cell viability reduced almost 100% upon the treatment of maximum concentration. These findings indicate that synergistic **(7)** has great potential combining chemo and photodynamic effects in one molecular platform and it can be conveniently employed both as photosensitizer and drug carrier for dual chemo- and photodynamic therapy.

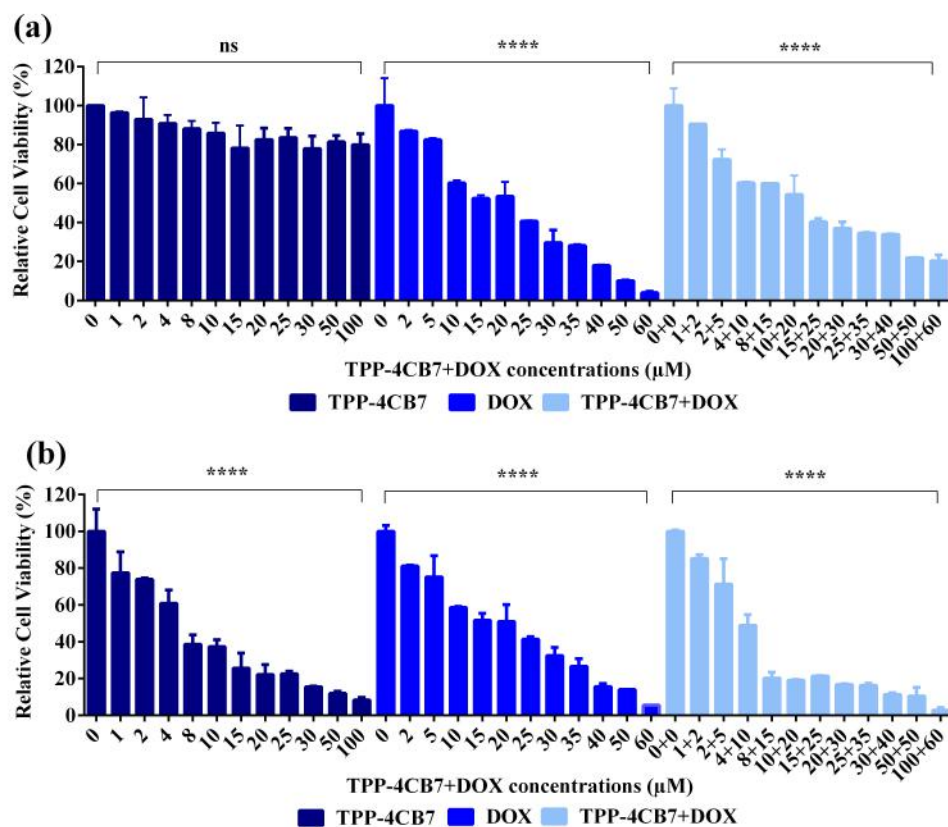
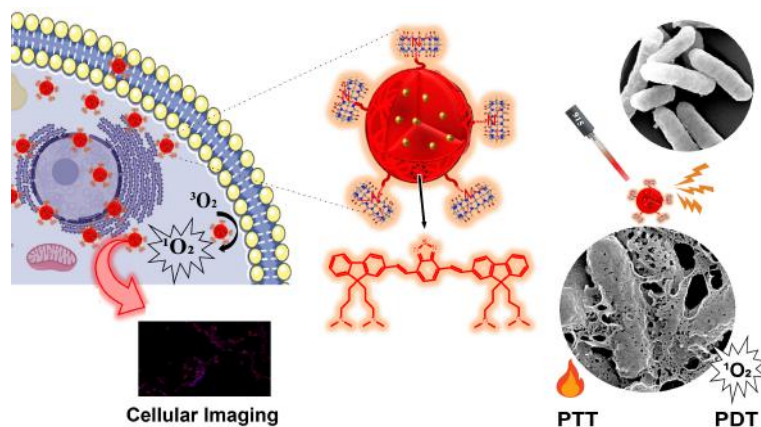


Figure 3.28: *In vitro* relative cell viability (%) after treatment with various concentrations of (7), DOX and (7)+DOX (a) in dark, (b) upon white light irradiation (5 min, 20 mW/cm²).

3.4 Cucurbituril-Capped Conjugated Oligomer-Gold Nanoparticles

•**M.Özkan**, S. E. Hadi, I. Tunc, Y. Midilli, B. Ortac and D. Tuncel, Cucurbit[7]uril-Capped Hybrid Conjugated Oligomer-Gold Nanoparticles for Combined Photodynamic-Photothermal Therapy and Cellular Imaging. *ACS Appl. Polym. Mater.* 2020, DOI:10.1021/acsapm.0c00540.



3.4.1 Aim of the Study

Herein, hybrid nanoparticles (NPs) made up of red-emitting conjugated oligomer (COL) (**8**) and gold nanoparticles (Au-NPs) were synthesized using a one-pot synthetic method. In this reaction, (**8**) acts both as reducing agent and as matrix for wrapping the newly formed Au-NPs. These hybrid NPs (COL-Au-NP) (**10**) were found to have photodynamic and photothermal killing efficiency towards gram-positive and gram-negative bacteria. (**10**) exhibits high photostability and thermal reversibility. Dark cytotoxicity of (**10**) against bacteria and human breast cancer cells (MCF-7) was remarkably decreased by capping it with (**2**) and resulting NPs were abbreviated as (CB7@COL-Au-NP) (**12**). Light-triggered cytotoxicity of (**10**) was maintained after synthesis of (**12**) upon irradiation by 915 nm laser for photothermal therapy (PTT) and white light for photodynamic therapy (PDT), respectively. Additionally, cellular imaging capability of (**12**) was shown owing to its inherently fluorescent property and this property could be utilized for image-guided therapy applications.

3.4.2 Preparation of NPs

In the Figure 3.30 schematic look for the synthesis of conjugated oligomer nanoparticles (COL-NP) (**9**), conjugated oligomer-gold nanoparticles (COL-Au-NP) (**10**) and complexation of amine residues of (**9**) and (**10**) by (**2**) yielding

(11) and (12) respectively, was depicted. Synthesis of benzothiadiazole and fluorene based (8) was published by our group according to given scheme in Figure 3.29. [64]

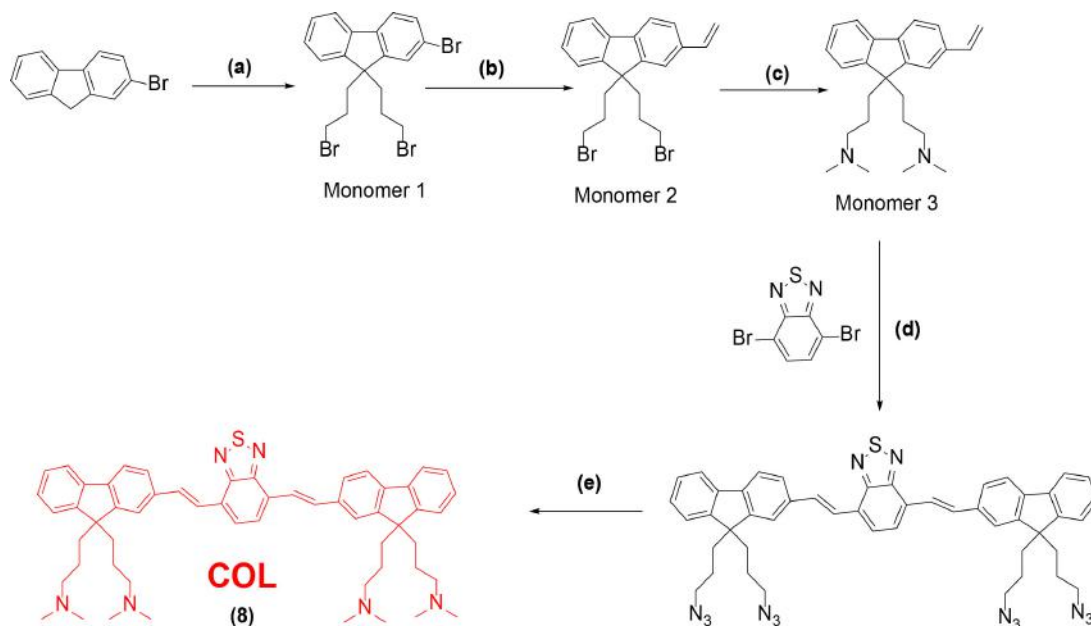


Figure 3.29: Schematic route to prepare (8).

(a) 1,3-Dibromopropane, aq. NaOH (50%, w/w), tetra-butyl ammonium bromide (TBAB), 80 °C, 64%, (b) tributyl vinyltin, Pd(Cl₂)(PPh₂)₂, 2,6-di-tert-butyl phenol, toluene, 100 °C, 24 h, 90%, (c) NaN₃, 60 °C, DMF, 24 h, 93%, (d) aq. K₂CO₃, Pd(OAc)₂, Pd(PPh₃)₄, DMF, 70 °C, 24 h, 45%, (e) PPh₃, THF, 25 °C, 24 h, 80%.

To prepare NPs, (8) was dissolved in tetrahydrofuran (THF) and added dropwise to Milli-Q water and aqueous AuCl₃ solution while sonicating for obtaining (9) and (10), respectively. Using this strategy provides *in situ* formation of metal NPs without needing extra reducing agent since tertiary amine pendant groups in (8) behaves as reducing agent and as ligands for stabilizing newly formed metal NPs. Various ratios of (8) to Au ion concentration were probed and 2:1, (8):Au was determined as the optimum one. Raspberry-type design was also tried in which NPs were obtained by first forming (9) and then reacted with Au ions

to yield Au NPs on (9) but resulting NPs were found to be unstable undergoing agglomeration over time. Thus, in the next studies, hybrid NPs with the determined optimum ratio having Au-NP wrapped by (8) design were used.

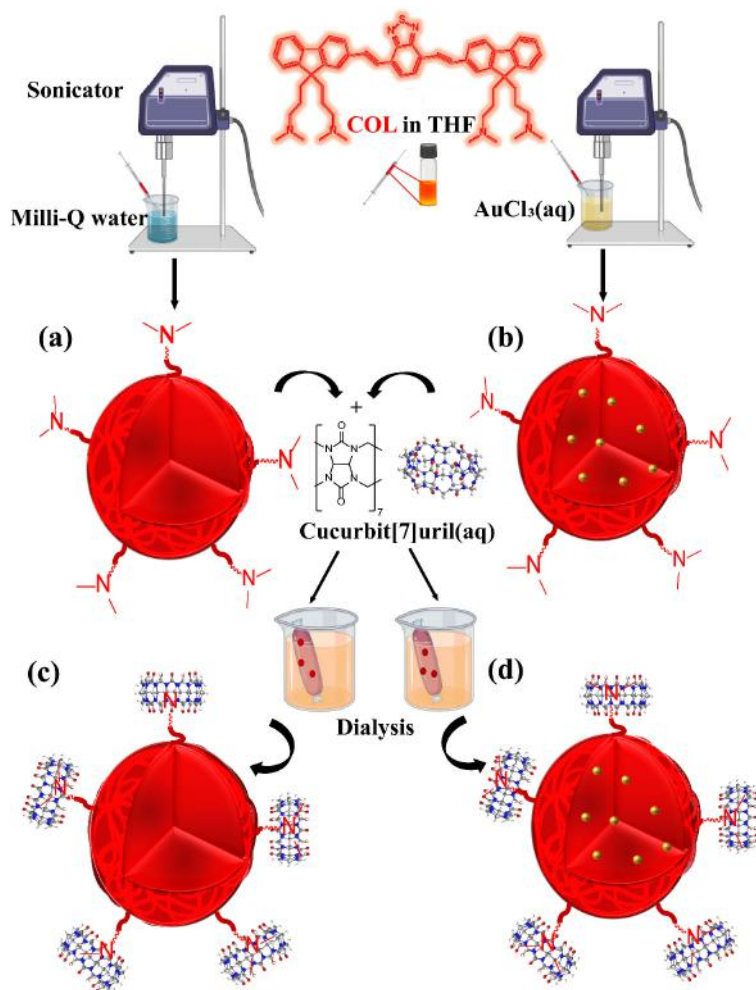


Figure 3.30: A schematic view for the synthesis of (a) conjugated oligomer nanoparticles (COL-NP) (9), (b) conjugated oligomer-gold nanoparticles (COL-Au-NP) (10), and complexation of amine residues of NPs with CB7, (c) CB7@COL-NP (11), (d) CB7@COL-Au-NP (12).

Sizes of prepared NPs were determined by dynamic light scattering (DLS) measurements. Mean hydrodynamic diameter was reported as around 122 nm for (9). For (10), it reduced to ~84 nm, for (11) ~123 nm and for (12) ~83 nm (Figure 3.31). The ζ -potential measurements showed that (9) and (10) own zeta potentials of +50 mV. Amine groups at the pendant chain of (8) are responsible

for these positive zeta-potentials proving the formation of stable nanoparticle dispersion through repulsive forces between NPs. When capping them by (2) did not affect their size. However, their zeta-potential values reduced to around +25 mV because of partially negatively charged carbonyl groups of (2). In table 3.1, average zeta size, polydispersity index (PDI), and zeta-potential of NPs were shown.

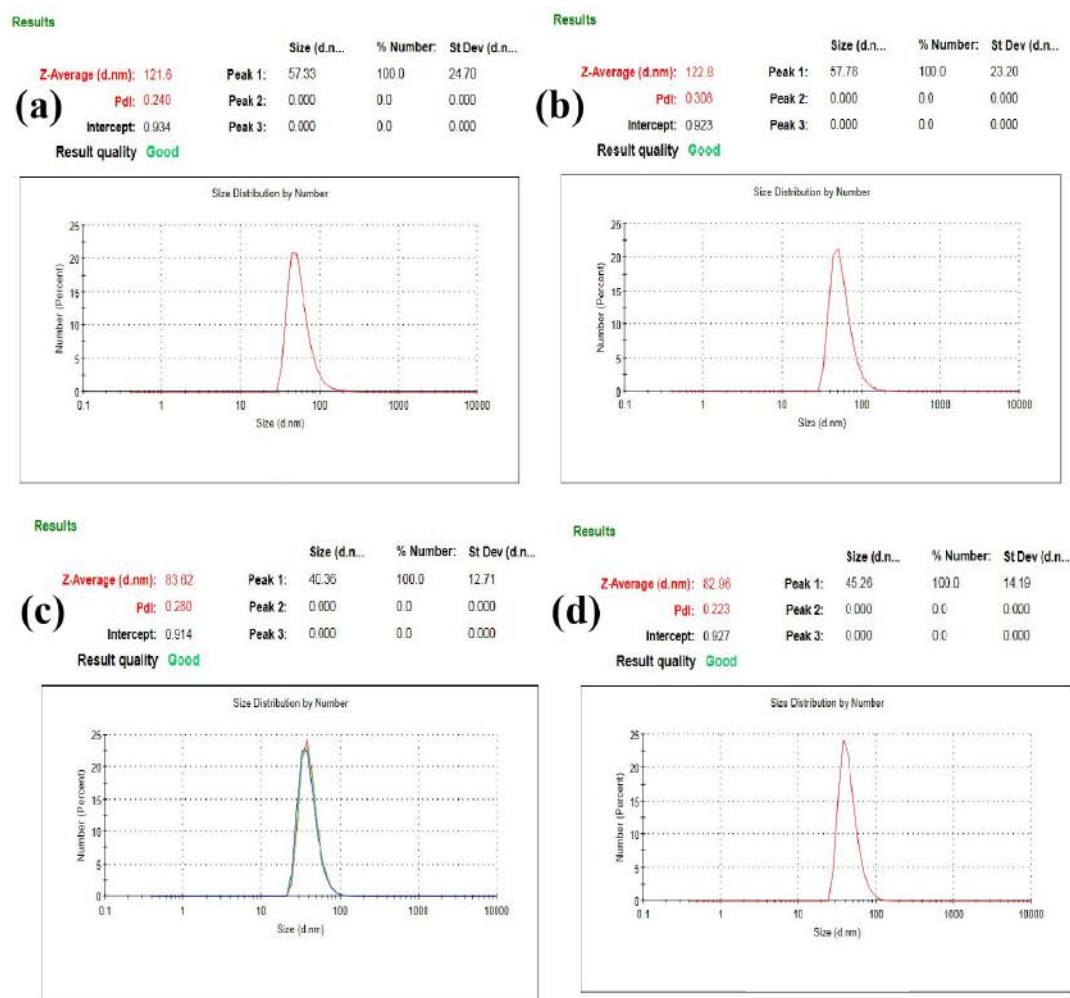


Figure 3.31: DLS histograms of (a) (9), (b) (11), (c) (10), (d) (12).

NPs	Z-average (nm)	PDI	ζ -potential (mV)
(9)	121.6	0.240	52.2
(11)	122.8	0.306	24.3
(10)	83.62	0.280	54.1
(12)	82.96	0.223	37.3

Table 3.1: Z-average size, PDI and zeta potential of (9), (10), (11) and (12).

3.4.3 Photophysical and Photothermal Properties of NPs

Photophysical properties of (9) and (10) were characterized using UVvis-NIR absorption spectroscopy. While UV-vis-NIR spectrum of (9) in water exhibits two main peaks at 350 and 457 nm. However, the peak at 457 nm was found to be red-shifted 12 nm for (10) and appeared than that of (9). The reason behind this finding is the contribution of additional plasmonic band of (10) beside the absorption peak of (9) (Figure 3.32).

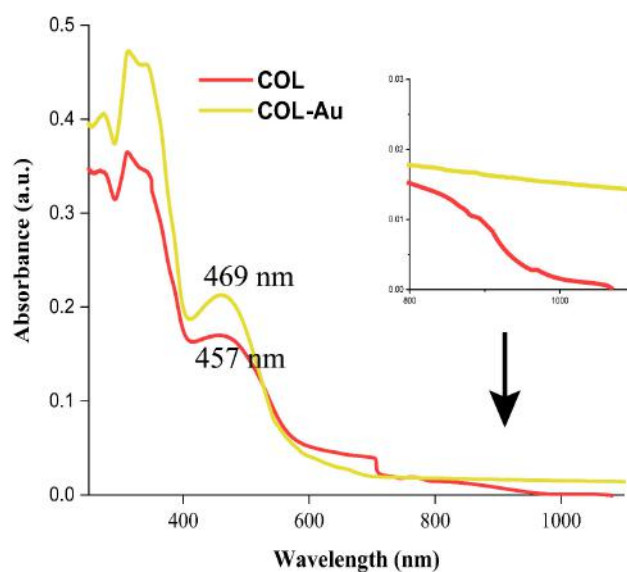


Figure 3.32: UV-vis-NIR absorbance spectrum of (9) and (10) in Milli-Q water.

The average lifetimes for **(8)**, **(9)** and **(10)** were reported based on the intensity-averaged (IA) and amplitude-averaged (AA) lifetime and compiled in Table 3.2. For both **(9)** and **(10)** the fluorescence lifetime and quantum yield remarkably reduced in comparison to **(8)** solution in THF caused by folding of **(8)** chains in water leading to close contacts and also considerable increase in their non-radiative channels.

Sample	IA lifetime (ns)	AA lifetime (ns)	Quantum Yield (%)
(8)	4.4	3.3	65.3
(9)	0.5	0.3	6
(10)	0.3	0.2	3

Table 3.2: The fluorescence lifetime and quantum yield of **(8)**, **(9)** and **(10)**.

The ROS generation performances of **(9)** and **(10)** under white light illumination (1 mW/cm^2) were evaluated by DCFH-DA assay similarly described in section 3.2.3 and details are available in the publication. [120] Both **(9)** and **(10)** were found to have high ROS generation ability but ROS generation ability of **(10)** was higher than that of **(9)** which can be justified by the metal-enhanced ROS generation effect. [125]

3.4.4 Photothermal Properties of NPs

Photothermal properties of hybrid NPs was analysed although significant plasmonic absorption peak for **(10)** was not seen in the NIR region of the spectrum. Aqueous dispersions of **(9)**, **(10)**, **(11)** and **(12)** were excited by a NIR laser of 915 nm wavelength. Various laser dosages between $1\text{-}7 \text{ W/cm}^2$ and NP concentrations between $1\text{-}10 \text{ }\mu\text{M}$ were tested to determine optimum laser density and NP concentration. During irradiation, heat was released leading to temperature elevation. Temperature elevation over time for each condition were recorded using thermal camera. The results were shown in Figure 3.33.

Optimum conditions were determined as $10 \text{ }\mu\text{M}$ with a flux of 7 W/cm^2 to

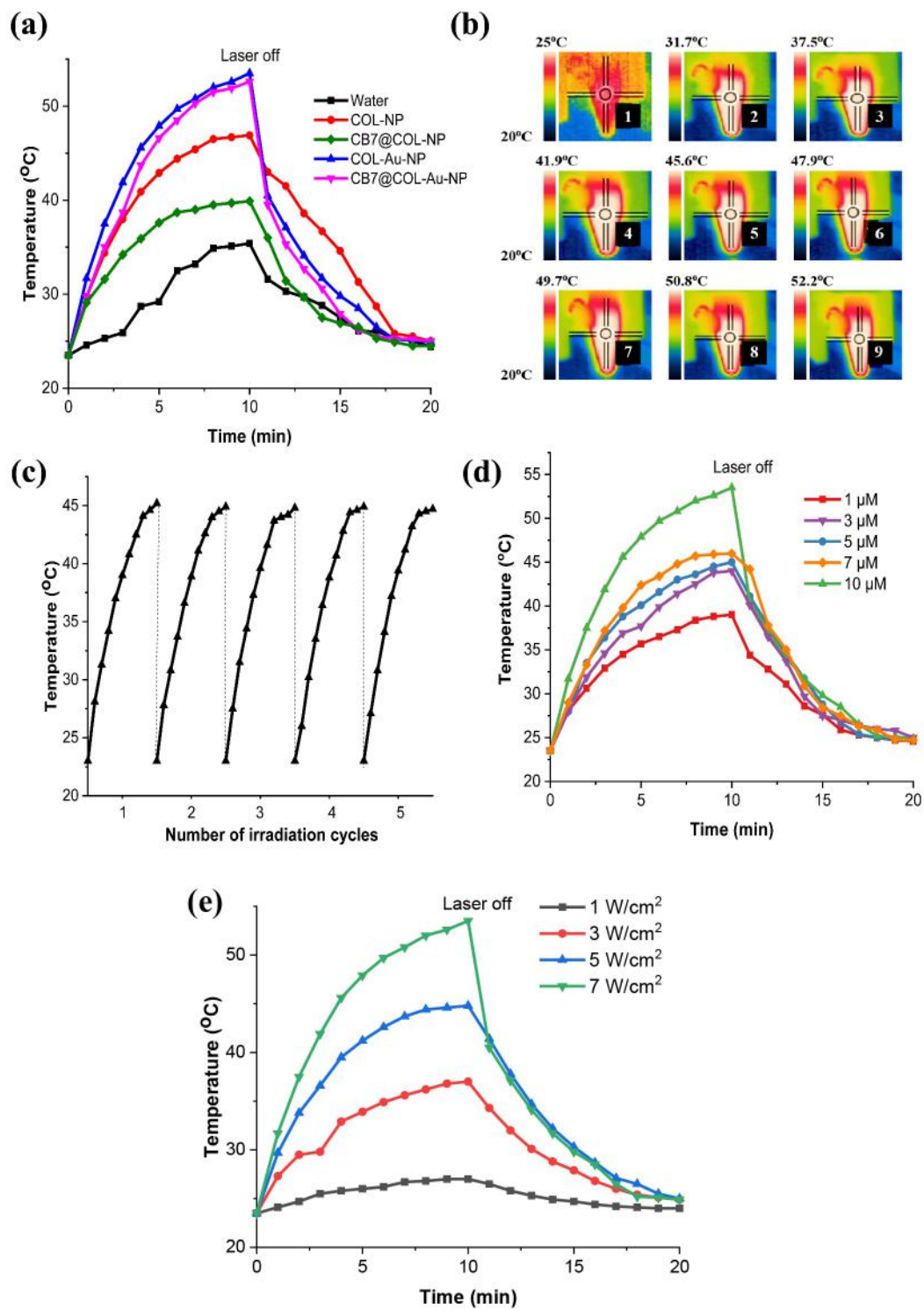


Figure 3.33: Photothermal response of NPs.

record maximum temperature elevation. These conditions yielded photothermal conversion efficiency of **(10)** as $\sim 15\%$ which was determined using a method reported in the literature [126] and related calculations were shown in the following section in detail. Laser intensity was higher than the ones used in literature experiments. However, concentration of NPs was quite low ($10 \mu\text{M} = 8.6 \mu\text{g/mL}$). Instead of using higher NP concentrations, laser density was risen for being more convenient for bacterial experiments. Temperature elevation of NPs over time was presented in Figure 3.33 a. **(12)** gives almost the same photothermal response with **(10)**. The rapid temperature increase was observed for **(10)** and **(12)** over 45°C within 5 min. At the end of light exposure, temperature reached to 52°C . After 10 min, the laser was shut off to investigate whether the temperature decreases to the initial temperature or not. It was important to confirm the reversibility of process. NIR thermal images were given in Figure 3.33 b. At the end of the 5 serial ON/OFF cycles irradiating each for 5 min, **(10)** preserved its photothermal performance (Figure 3.33 c). This observation is crucial characteristic of good photothermal agent proving its high photothermal stability. Moreover, **(10)** exhibits dose-dependent temperature elevation as shown in Figure 3.33 d at fixed laser flux. It was also seen that temperature rises at fixed concentration of **(10)** as laser density was increased (Figure 3.33 e).

3.4.5 Quantification of Photothermal Conversion Efficiency

The photothermal conversion efficiency (η) of **(10)** was quantified by following the method reported in the literature. [126] Total energy balance for system:

$$\sum m_i C_{p,i} \frac{dT}{dt} = Q_{(10)} + Q - Q_{env} \quad (3.1)$$

where

$$m = \text{mass of water} = 1.0 \text{ g}$$

C_p = heat capacity of water = 4.186 J/g

T = solution temperature

$Q_{(10)}$ = energy inputted by nanoparticles

Q = heat dissipated from the light absorbed by the solvent and container

Q_{env} = is heat conduction away from the system surface by air

$$Q_{(10)} = I(1 - 10^{-A^{915}})\eta \quad (3.2)$$

I= laser power

A^{915} = absorbance of **(10)** at 915 nm

η = photothermal conversion efficiency of **(10)**

$$Q_{env} = hS(T - T_{env}) \quad (3.3)$$

h=the heat transfer coefficient

S=surface area of the container

T_{env} =environmental temperature

$$Q_{(10)} + Q = hS(T_{max} - T_{env}) \quad (3.4)$$

T_{max} =maximum steady temperature

$$\eta = \frac{hS(T_{max} - T_{env}) - Q}{I(1 - 10^{-A^{915}})} \quad (3.5)$$

$$\theta = \frac{(T - T_{env})}{(T_{max} - T_{env})} \quad (3.6)$$

θ =dimensionless parameter

$$\eta = \frac{hS(T_{max} - T_{env}) - Q}{I(1 - 10^{-A^{915}})} \quad (3.7)$$

$$\tau_s = \frac{\sum m_i C_{p,i}}{hS} \quad (3.8)$$

τ_s =sample system time constant

$$\frac{d\theta}{dt} = \frac{1}{\tau_s} \left[\frac{Q_{(10)} + Q}{hS(T_{max} - T_{env})} \right] - Q \quad (3.9)$$

When the laser was shut off: $Q_{(10)} + Q = 0$ yields:

$$dt = -\tau_s \frac{d\theta}{\theta} \quad (3.10)$$

Integration of equation 3.10 yields:

$$t = -\tau_s \ln \theta \quad (3.11)$$

Q was measured as 28.5 mW from container filled with Milli-Q water without (10).

$$T_{max} - T_{env} = 18.1 \text{ }^\circ\text{C}$$

$$I = 7 \text{ W/cm}^2$$

$A^{915} = 0.03$ (from Figure 3.32)

τ_s was determined as 12.6 min which is 756 s by applying the linear time data vs negative natural logarithm of θ (slope of linear fitting corresponds to 776 s). From equation 3.8, hS is found to be 5.5 mW/°C.

Therefore, according to equation 3.8, the hS is found to be 5.5 mW/ °C. Substituting hS value into equation 3.5, the 915 nm laser photothermal conversion efficiency of (10) is quantified as

$$\eta_{(10)} = \frac{(5.5mW/^\circ * C18.1^\circ C - 28.5mW)}{7000mW * (1 - 10^{-0.03})}$$

$$\eta_{(10)}=15.2\%$$

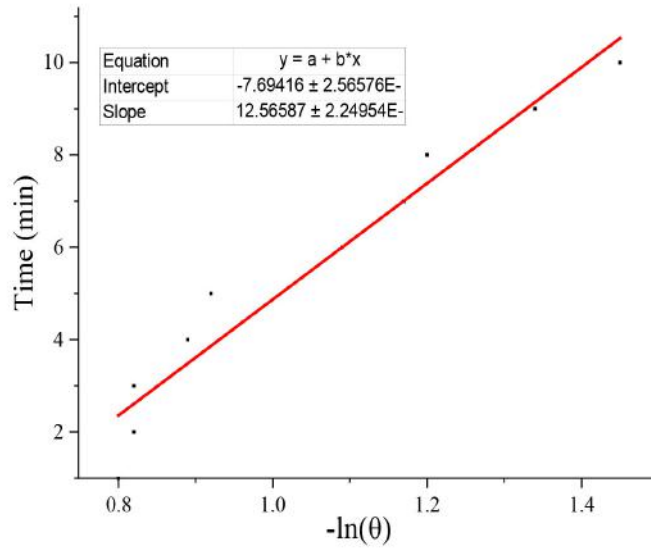


Figure 3.34: Time vs $-\ln(\theta)$ graph for the quantification of photothermal conversion efficiency of (10).

3.4.6 Photodynamic Effects of NPs on Bacteria

Photodynamic inactivation of *E. coli* by NPs was shown under photoirradiation (22 mW/cm², 3 min) as described for (6). Bacterial suspensions were treated with 12.4 μg/mL (determined as MIC value) of NPs both in the dark and under light exposure and their semi-solid LB agar plate and corresponding SEM images were presented in Figure 3.35. Quantification of CFUs indicated around 3.5-log reduction (Figure 3.36) in CFU of *E. coli* treated with 12.4 μg/mL of (10) upon light illumination. On the other hand, in the dark, (10) was also found to be toxic with 0.6-log reduction which cannot be considered as negligible. For solving this dark cytotoxicity, the amine residues on the surfaces of (10) were complexed with (2) yielding (12). Dark cytotoxicity (12) was considerably decreased and it was observed to be highly stable in aqueous solution, PBS, and DMEM. No visible aggregation of (12) was seen in those media. The same treatments on *B. subtilis* yielded similar results.

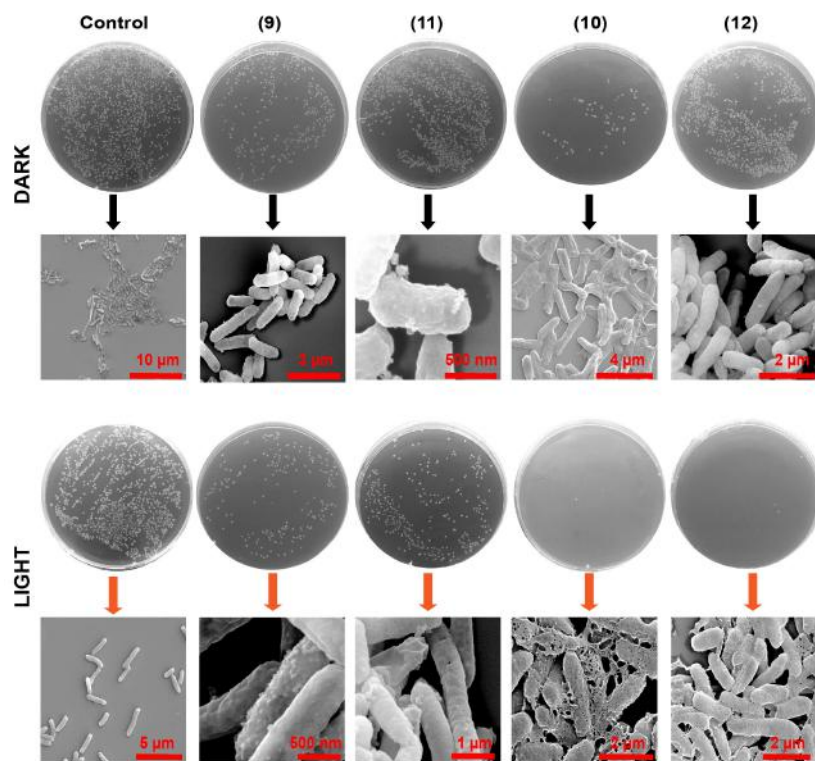


Figure 3.35: Semi-solid agar plate and corresponding SEM pictures for *E. coli* treated with 12.4 μg/mL of NPs in the dark and under light.

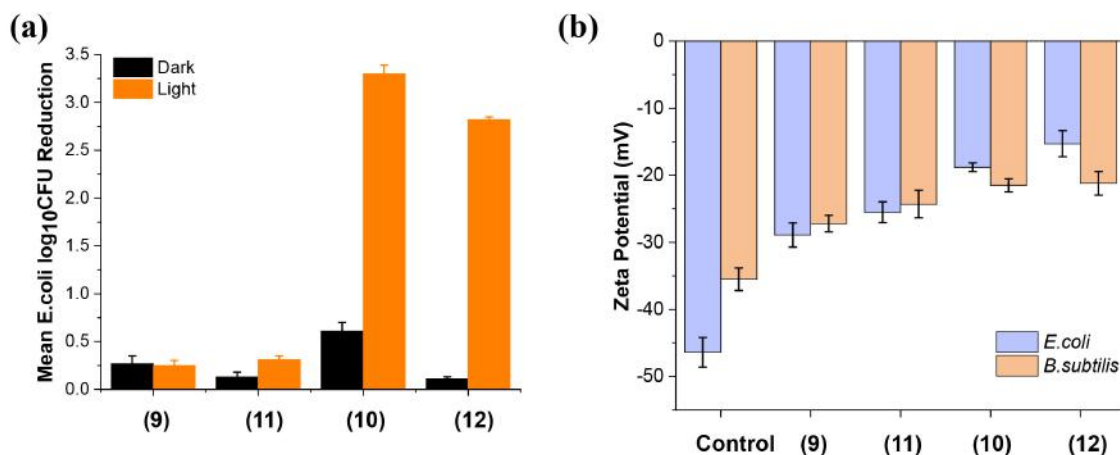


Figure 3.36: (a) Mean *E. coli* log₁₀CFU reduction upon NP-treatment in the dark and under light, (b) ζ -potential measurements of NP-treated *E. coli* and *B. subtilis*.

3.4.7 Cellular Imaging by NPs

Photodynamic anti-cancer effect of NPs was proven on MCF-7 cells using MTT assay. Since photodynamic inactivation of MCF-7 cells were explained for (6) and (7) and that is quite similar to that of NPs, this part will not be focused. However, related discussions are available in the referred publication in detail. [120] Instead, as a more novel part, application of NPs in cellular imaging will be emphasized. Since the NPs are fluorescent by their nature, they are suitable for being directly employed in cellular imaging or image-guided PDT of cancer. For confirming whether NPs are able to be internalized by MCF-7 cells or not, NP-treated and non-treated cells were checked by confocal laser scanning microscopy (CLSM) as given in Figure 3.37. Cells were incubated with 1 μ M of (10) and (12) for 72 h. However, for the light groups, after 48 h, cells were illuminated by white light for 20 min (the same conditions used in MTT assays). Cellular nuclei were stained by DAPI. DAPI emits blue fluorescence emission upon excitation by 461 nm laser, whereas (10) emits red fluorescence upon excitation by 580 nm laser. From the Figure 3.37 c, d and h, merged images verify that the cellular uptake of (10) and (10) was accumulated specifically around the nuclear membrane.

Besides, change in cellular phenotype after treatment with NPs was obvious. Differential interference contrast microscopy (DIC) pictures of MCF-7 cells were also taken. Figure 3.37 a and e present the DIC pictures of control group in the dark and also upon light illumination. Cells were observed to be highly adherent and in cobblestone-like shape. They preserve their edged structure even after exposing them to light. However, when the cells were treated with (10) even without light, morphological changes were clearly observed. Cells could not preserve their sided membrane shape and were seen to be circular having dark inner contents as shown in the Figure 3.37 i. Similar phenotypical differences were observed for (12) as well disturbing the appearance of cells (Figure 3.38).

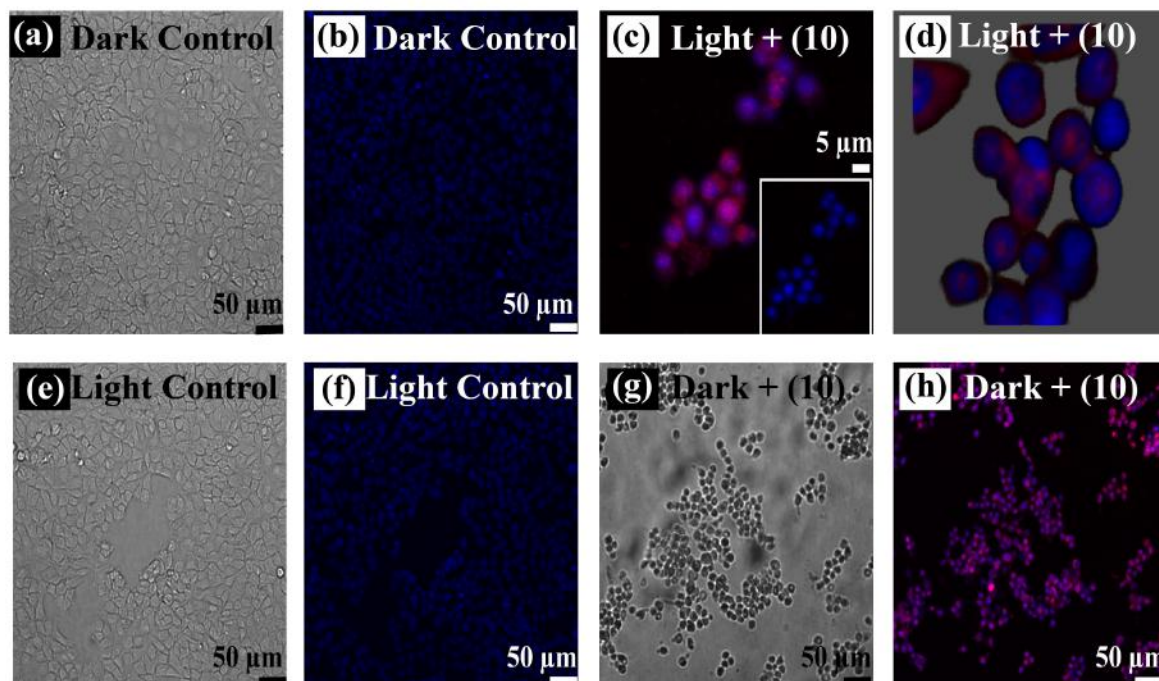


Figure 3.37: DIC and CLSM images of (10)-treated and non-treated MCF-7 cells with and without light.

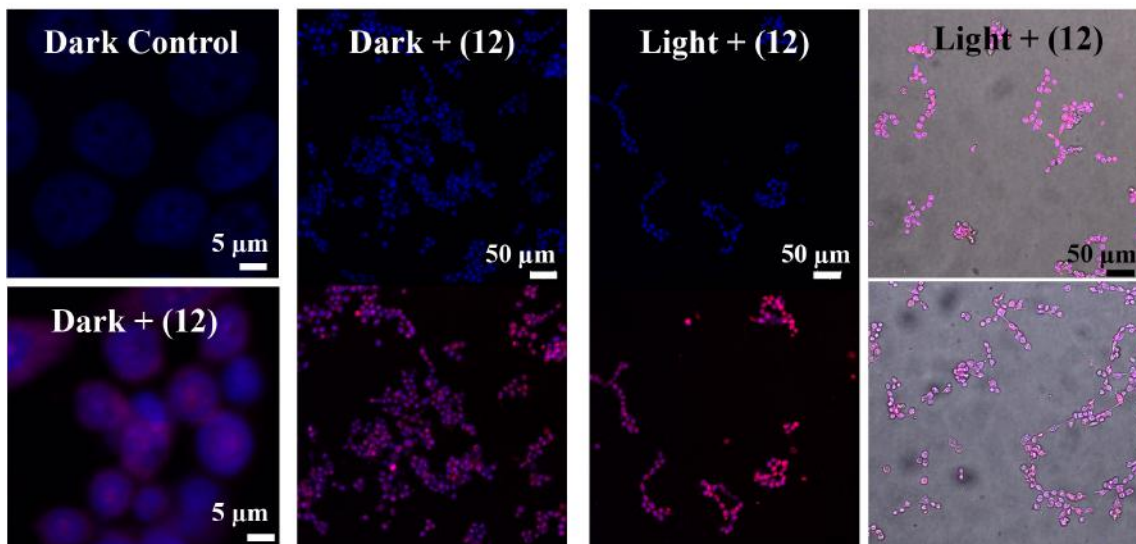


Figure 3.38: CLSM images of MCF-7 nuclei stained with DAPI (blue) and treated with (12) (merged).

3.4.8 Combined PTT/PDT Effect of NPs on Bacteria

After revealing that NPs function as good photosensitizers with photothermal properties, combination of PDT and PTT on bacteria was aimed. Combined PDT and PTT effect of NPs was investigated by treating *E. coli* and *B. subtilis* with 12.4 $\mu\text{g}/\text{mL}$ (MIC value) of NPs using agar disk diffusion assay. Also, a reference antibiotic, ampicillin was used for the comparison of performance of NPs with standard. As illustrated in Figure 3.39, treatments were performed in dark, only under white light illumination for 3 min (PDT), only under 915 nm NIR laser excitation for 3 min (PTT) and under 3 min white light illumination followed by 3 min 915 nm NIR laser excitation (combined PDT/PTT). Inhibition zones were reported as cell-free zones and they were the mean of radii measured from at least six different points of circle. Experiments were performed at least three times, results were plotted as the mean of three independent experiments and error bars represent the standard deviation. Expectedly, the inhibition zone for ampicillin was measured to be around 3 mm for all conditions. In the dark, only the inhibitory effect of (10) was clear on both bacteria. PDT performance of (10) was much better than that of PTT. When PDT and PTT conditions

were simultaneously applied, broader inhibition zones were recorded for all NPs as shown in Figure 3.40. Particularly for (12), inactivation of both species was dramatically enhanced. These observations reveal that combined PDT and PTT could afford improved antibacterial therapeutic output beyond individual modes of PDT or PTT.

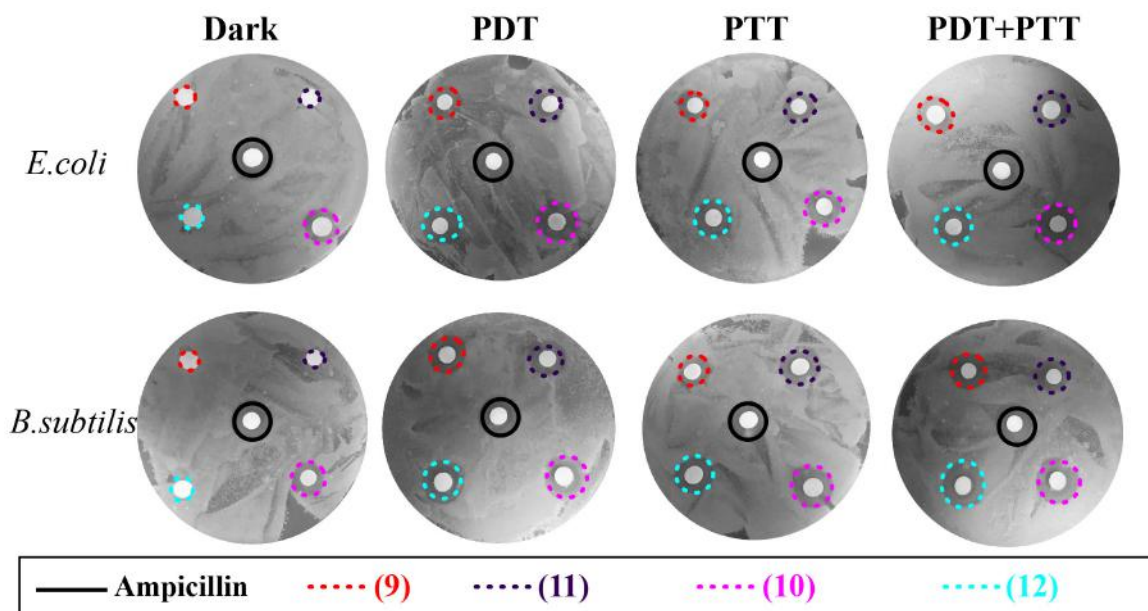


Figure 3.39: Plate photographs of agar disc diffusion assays of *E. coli* and *B. subtilis* treated with $12.4 \mu\text{g}/\text{mL}$ of ampicillin, (9), (10), (11) and (12) in the dark and satisfying PDT, PTT and PDT+PTT conditions.

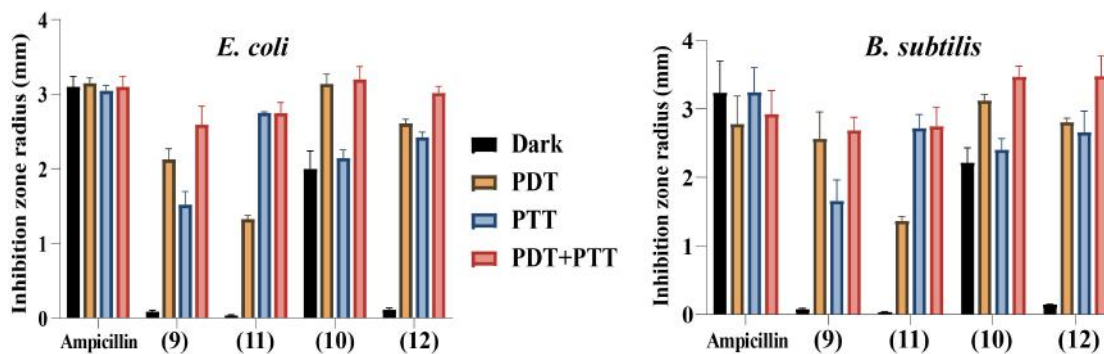


Figure 3.40: Inhibition zone graphs of *E. coli* and *B. subtilis* for the plates in Figure 3.39.

Chapter 4

Conclusions and Future Prospective

Three multifunctional supramolecular constructs based on CB and photoactive conjugated compounds were successfully prepared and their use in various nanomedicine applications including antimicrobial and anticancer PDT, combined PDT and PTT for the inactivation of bacteria, drug delivery and cellular imaging was also demonstrated.

Firstly, stable [5]-rotaxane based on photoactive tetraphenyl porphyrin derivative core and CB6, as macrocycle, were obtained through 1,3-dipolar cycloaddition reactions. Further investigation of [5]-rotaxane revealed that it has ability to generate ROS efficiently and this, in turn, makes it a desirable photosensitizer which can remain stable at physiological pH (7.4) for prolonged times. By utilizing these aforementioned features, [5]-rotaxane was employed as a broad-spectrum antibacterial agent against Gram-negative (*E. coli*) and Gram-positive (*B. subtilis*) bacteria which were selected as modal organisms as well as anticancer agent against human breast cancer cell line (MCF-7) via visible-light-promoted generation of ROS. [5]-rotaxane was found to have negligible dark cytotoxicity upon complexation with CB6 and it could afford efficacious PDT of cancer and infectious diseases caused by bacteria. Although various types of rotaxanes were

constructed and found to have high singlet oxygen generation capacity, they were mainly mentioned in the context of potential PDT agents in the literature. Thus, [5]-rotaxane is rare example of rotaxanes implemented in PDT.

Second multifunctional photoactive supramolecular assembly was built through covalently binding of four CB7 molecules, behaving as receptor, to a tetraphenyl porphyrin core using suitable linkers. As well as its light-promoted antibacterial and antitumor property just like [5]-rotaxane, here, main goal was the achievement of combine chemo- and photodynamic cancer therapy which makes this study novel. Host-guest interactions took place between CB7 and an anticancer drug, doxorubicin hydrochloride (DOX), enabling this system to be used as drug delivery vehicles and hereby synergistic PDT and chemotherapy was achieved. Finally, CB7-capped hybrid nanoparticles (NPs) made up of red-emitting conjugated oligomer (COL) and gold nanoparticles (Au-NPs) were prepared using one-pot synthetic method. These hybrid NPs were found to have high photostability, thermal reversibility and high ROS generation capacity. Benefitting from these properties, combined photodynamic and photothermal killing efficiency of NPs towards Gram-positive and Gram-negative bacteria was verified. Combination of therapies facilitated more enhanced therapeutic outputs of individual therapies by cooperatively integrating them into a single theranostic platform. Furthermore, their use in cellular imaging capability was shown owing to their intrinsically fluorescent properties and this feature offers a great promise for the image-guided PDT applications.

All of these three systems have two main features in common. Firstly, since they were composed of photoactive compounds, they are good photosensitizers with high stability in biological media and high ROS production performance which renders them suitable for PDT of cancer and wide range bacterial infections. Secondly, their inhibitory effects were switched on under photoirradiation even quite low flux of light and short exposure time whereas it was switched off in the dark. This controllable disguise was provided upon complexation with CB molecules by reducing dark cytotoxicity of photoactive compounds significantly. Achieving efficacious PDT is appealing and promising since over the past few decades, material-based alternative strategies have been extensively sought due

to expanding concerns about the rapid evolution of antidrug-resistant pathogens and cancer cells. At this point, PDT gains keen attention as clinically approved antimicrobial and antitumor strategy showing minimal invasiveness, enhanced targeting properties and reduced side effects in comparison with the other conventional therapies. Therefore, constructing such systems affording good therapeutic outcomes are important and constructed CB-based supramolecular assemblies can be considered as useful contributions.

On the other hand, deficiency of these CB-based supramolecular constructs should also be mentioned from the clinical point of view. The mutual and main drawback of these systems is weak specificity. Although these supramolecular assemblies were not tried on the normal cells yet, they most probably affect normal cells too under light. Specificity of them relies mainly on enhanced permeability and retention (EPR) effect which is considered as passive targeting. Targeted cancer therapy is one of the major modalities of medical treatment and still remains as a big challenge of nanomedicine. Vast majority of research efforts have been directed towards to achievement of efficient targeting. Prospective and the most promising applications of the prepared CB-based supramolecular constructs would be enhanced targeting of cancer cells. For this purpose, as future studies, they can be integrated with superparamagnetic iron oxide nanoparticles (SPIONs) for magnetic targeting of cancer upon exposure to magnetic field as reported in the collaborative work of our group and King's College London. [127] Modifying the structure of these current CB-based supramolecular assemblies by incorporating cancer targeting peptides might also be useful in this regard. Future studies will mainly be focused on enhancing targeting properties of them. To this end, engineering of their structure will be needed to increase stimuli-responsiveness for active targeting and then modified constructs should be tried *in vitro* and *in vivo* to investigate whether targeting is successful.

Bibliography

- [1] J. M. Lehn, “Cryptates: the chemistry of macropolycyclic inclusion complexes,” *Accounts of chemical research*, vol. 11, no. 2, pp. 49–57, 1978.
- [2] J.-M. Lehn, “Supramolecular chemistry—scope and perspectives molecules, supermolecules, and molecular devices (nobel lecture),” *Angewandte Chemie International Edition in English*, vol. 27, no. 1, pp. 89–112, 1988.
- [3] J. W. Steed, D. R. Turner, and K. Wallace, *Core concepts in supramolecular chemistry and nanochemistry*. John Wiley & Sons, 2007.
- [4] D. Tuncel, A. Kaifer, U. Pischel, R. Wang, Z. Li, H. Pal, K. Kim, J. Mohanty, D. Fuentealba, H.-J. Schneider, *et al.*, *Cucurbituril-based Functional Materials*. Royal Society of Chemistry, 2019.
- [5] B. Nagel, H. Dellweg, and L. Gierasch, “Glossary for chemists of terms used in biotechnology (iupac recommendations 1992),” *Pure and Applied Chemistry*, vol. 64, no. 1, pp. 143–168, 1992.
- [6] L. K. von Krbek, C. A. Schalley, and P. Thordarson, “Assessing cooperativity in supramolecular systems,” *Chemical Society Reviews*, vol. 46, no. 9, pp. 2622–2637, 2017.
- [7] J. B. Wittenberg and L. Isaacs, “Complementarity and preorganization,” *Supramolecular Chemistry: From Molecules to Nanomaterials*, 2012.
- [8] D. J. Cram, “Preorganization—from solvents to spherands,” *Angewandte Chemie International Edition in English*, vol. 25, no. 12, pp. 1039–1057, 1986.

- [9] S. Dong, B. Zheng, F. Wang, and F. Huang, "Supramolecular polymers constructed from macrocycle-based host-guest molecular recognition motifs," *Accounts of chemical research*, vol. 47, no. 7, pp. 1982-1994, 2014.
- [10] C. J. Pedersen, "Cyclic polyethers and their complexes with metal salts," *Journal of the American Chemical Society*, vol. 89, no. 26, pp. 7017-7036, 1967.
- [11] J. Szejtli, "Introduction and general overview of cyclodextrin chemistry," *Chemical reviews*, vol. 98, no. 5, pp. 1743-1754, 1998.
- [12] S. Tan, K. Ladewig, Q. Fu, A. Blencowe, and G. G. Qiao, "Cyclodextrin-based supramolecular assemblies and hydrogels: recent advances and future perspectives," *Macromolecular rapid communications*, vol. 35, no. 13, pp. 1166-1184, 2014.
- [13] F. Van De Manakker, T. Vermonden, C. F. Van Nostrum, and W. E. Hennink, "Cyclodextrin-based polymeric materials: synthesis, properties, and pharmaceutical/biomedical applications," *Biomacromolecules*, vol. 10, no. 12, pp. 3157-3175, 2009.
- [14] G. Crini, S. Fourmentin, É. Fenyvesi, G. Torri, M. Fourmentin, and N. Morin-Crini, "Cyclodextrins, from molecules to applications," *Environmental chemistry letters*, vol. 16, no. 4, pp. 1361-1375, 2018.
- [15] T. Ogoshi, S. Kanai, S. Fujinami, T.-a. Yamagishi, and Y. Nakamoto, "para-bridged symmetrical pillar [5] arenes: their lewis acid catalyzed synthesis and host-guest property," *Journal of the American Chemical Society*, vol. 130, no. 15, pp. 5022-5023, 2008.
- [16] X.-S. Du, C.-Y. Wang, Q. Jia, R. Deng, H.-S. Tian, H.-Y. Zhang, K. Meguellati, and Y.-W. Yang, "Pillar [5] arene-based [1] rotaxane: high-yield synthesis, characterization and application in knoevenagel reaction," *Chemical Communications*, vol. 53, no. 38, pp. 5326-5329, 2017.
- [17] J.-F. Chen, Q. Lin, Y.-M. Zhang, H. Yao, and T.-B. Wei, "Pillararene-based fluorescent chemosensors: recent advances and perspectives," *Chemical Communications*, vol. 53, no. 100, pp. 13296-13311, 2017.

- [18] W. Si, L. Chen, X.-B. Hu, G. Tang, Z. Chen, J.-L. Hou, and Z.-T. Li, "Selective artificial transmembrane channels for protons by formation of water wires," *Angewandte Chemie International Edition*, vol. 50, no. 52, pp. 12564–12568, 2011.
- [19] W. Feng, M. Jin, K. Yang, Y. Pei, and Z. Pei, "Supramolecular delivery systems based on pillararenes," *Chemical Communications*, vol. 54, no. 97, pp. 13626–13640, 2018.
- [20] C. D. Gutsche and R. Muthukrishnan, "Calixarenes. 1. analysis of the product mixtures produced by the base-catalyzed condensation of formaldehyde with para-substituted phenols," *The Journal of Organic Chemistry*, vol. 43, no. 25, pp. 4905–4906, 1978.
- [21] Z. Liu, S. K. M. Nalluri, and J. F. Stoddart, "Surveying macrocyclic chemistry: from flexible crown ethers to rigid cyclophanes," *Chemical Society Reviews*, vol. 46, no. 9, pp. 2459–2478, 2017.
- [22] R. Behrend, E. Meyer, and F. Rusche, "I. ueber condensationsproducte aus glycoluril und formaldehyd," *Justus Liebigs Annalen der Chemie*, vol. 339, no. 1, pp. 1–37, 1905.
- [23] J. Kim, I.-S. Jung, S.-Y. Kim, E. Lee, J.-K. Kang, S. Sakamoto, K. Yamaguchi, and K. Kim, "New cucurbituril homologues: syntheses, isolation, characterization, and x-ray crystal structures of cucurbit [n] uril (n= 5, 7, and 8)," *Journal of the American Chemical Society*, vol. 122, no. 3, pp. 540–541, 2000.
- [24] A. Day, A. P. Arnold, R. J. Blanch, and B. Snushall, "Controlling factors in the synthesis of cucurbituril and its homologues," *The Journal of organic chemistry*, vol. 66, no. 24, pp. 8094–8100, 2001.
- [25] A. I. Day, R. J. Blanch, A. P. Arnold, S. Lorenzo, G. R. Lewis, and I. Dance, "A cucurbituril-based gyroscane: a new supramolecular form," *Angewandte Chemie*, vol. 114, no. 2, pp. 285–287, 2002.
- [26] F. Diederich, P. J. Stang, and R. R. Tykwinski, *Modern supramolecular chemistry: strategies for macrocycle synthesis*. John Wiley & Sons, 2008.

- [27] E. Masson, X. Ling, R. Joseph, L. Kyeremeh-Mensah, and X. Lu, "Cucurbituril chemistry: a tale of supramolecular success," *Rsc Advances*, vol. 2, no. 4, pp. 1213–1247, 2012.
- [28] J. Lagona, P. Mukhopadhyay, S. Chakrabarti, and L. Isaacs, "The cucurbit [n] uril family," *Angewandte Chemie International Edition*, vol. 44, no. 31, pp. 4844–4870, 2005.
- [29] L. Isaacs, S.-K. Park, S. Liu, Y. H. Ko, N. Selvapalam, Y. Kim, H. Kim, P. Y. Zavalij, G.-H. Kim, H.-S. Lee, *et al.*, "The inverted cucurbit [n] uril family," *Journal of the American Chemical Society*, vol. 127, no. 51, pp. 18000–18001, 2005.
- [30] J. W. Lee, S. Samal, N. Selvapalam, H.-J. Kim, and K. Kim, "Cucurbituril homologues and derivatives: new opportunities in supramolecular chemistry," *Accounts of chemical research*, vol. 36, no. 8, pp. 621–630, 2003.
- [31] H.-J. Buschmann, E. Cleve, K. Jansen, A. Wego, and E. Schollmeyer, "The determination of complex stabilities between different cyclodextrins and dibenzo-18-crown-6, cucurbit [6] uril, decamethylcucurbit [5] uril, cucurbit [5] uril, p-tert-butylcalix [4] arene and p-tert-butylcalix [6] arene in aqueous solutions using a spectrophotometric method," *Materials Science and Engineering: C*, vol. 14, no. 1-2, pp. 35–39, 2001.
- [32] S. J. Barrow, S. Kaseera, M. J. Rowland, J. del Barrio, and O. A. Scherman, "Cucurbituril-based molecular recognition," *Chemical reviews*, vol. 115, no. 22, pp. 12320–12406, 2015.
- [33] F. Biedermann and O. A. Scherman, "Cucurbit [8] uril mediated donor–acceptor ternary complexes: a model system for studying charge-transfer interactions," *The Journal of Physical Chemistry B*, vol. 116, no. 9, pp. 2842–2849, 2012.
- [34] S. He, F. Biedermann, N. Vankova, L. Zhechkov, T. Heine, R. E. Hoffman, A. De Simone, T. T. Duignan, and W. M. Nau, "Cavitation energies can outperform dispersion interactions," *Nature chemistry*, vol. 10, no. 12, pp. 1252–1257, 2018.

- [35] F. Biedermann, W. M. Nau, and H.-J. Schneider, “The hydrophobic effect revisited—studies with supramolecular complexes imply high-energy water as a noncovalent driving force,” *Angewandte Chemie International Edition*, vol. 53, no. 42, pp. 11158–11171, 2014.
- [36] K. M. Park, M. Y. Hur, S. K. Ghosh, D. R. Boraste, S. Kim, and K. Kim, “Cucurbit [n] uril-based amphiphiles that self-assemble into functional nanomaterials for therapeutics,” *Chemical Communications*, vol. 55, no. 72, pp. 10654–10664, 2019.
- [37] D. Tuncel and J. H. Steinke, “Catalytically self-threading polyrotaxanes,” *Chemical Communications*, no. 16, pp. 1509–1510, 1999.
- [38] F. Constabel and K. Geckeler, “Nanoencapsulation of [60] fullerene with the cavitand cucurbit [7] uril,” 2004.
- [39] Q. An, Q. Chen, W. Zhu, Y. Li, C.-a. Tao, H. Yang, Z. Li, L. Wan, H. Tian, and G. Li, “A facile method for preparing one-molecule-thick free-standing organic nanosheets with a regular square shape,” *Chemical communications*, vol. 46, no. 5, pp. 725–727, 2010.
- [40] C. Hu, N. Ma, F. Li, Y. Fang, Y. Liu, L. Zhao, S. Qiao, X. Li, X. Jiang, T. Li, *et al.*, “Cucurbit [8] uril-based giant supramolecular vesicles: highly stable, versatile carriers for photoresponsive and targeted drug delivery,” *ACS applied materials & interfaces*, vol. 10, no. 5, pp. 4603–4613, 2018.
- [41] K. Madasamy, V. M. Shanmugam, D. Velayutham, and M. Kathiresan, “Reversible 2d supramolecular organic frameworks encompassing viologen cation radicals and cb [8],” *Scientific reports*, vol. 8, no. 1, pp. 1–12, 2018.
- [42] W. Wang and A. E. Kaifer, “Electrochemical switching and size selection in cucurbit [8] uril-mediated dendrimer self-assembly,” *Angewandte Chemie International Edition*, vol. 45, no. 42, pp. 7042–7046, 2006.
- [43] H. Chen, S. Hou, H. Ma, X. Li, and Y. Tan, “Controlled gelation kinetics of cucurbit [7] uril-adamantane cross-linked supramolecular hydrogels with competing guest molecules,” *Scientific reports*, vol. 6, no. 1, pp. 1–10, 2016.

- [44] X. Lu and E. Masson, "Formation and stabilization of silver nanoparticles with cucurbit [n] urils (n= 5- 8) and cucurbituril-based pseudorotaxanes in aqueous medium," *Langmuir*, vol. 27, no. 6, pp. 3051–3058, 2011.
- [45] A. Facchetti, " π -conjugated polymers for organic electronics and photovoltaic cell applications," *Chemistry of Materials*, vol. 23, no. 3, pp. 733–758, 2011.
- [46] I. Fischer, A. Kaeser, M. A. Peters-Gumbs, and A. P. Schenning, "Fluorescent π -conjugated polymer dots versus self-assembled small-molecule nanoparticles: What's the difference?," *Chemistry—A European Journal*, vol. 19, no. 33, pp. 10928–10934, 2013.
- [47] D. Tuncel, " π -conjugated nanostructured materials: preparation, properties and photonic applications," *Nanoscale Advances*, vol. 1, no. 1, pp. 19–33, 2019.
- [48] X. Xu, R. Liu, and L. Li, "Nanoparticles made of π -conjugated compounds targeted for chemical and biological applications," *Chemical Communications*, vol. 51, no. 94, pp. 16733–16749, 2015.
- [49] P. Rothmund, "Formation of porphyrins from pyrrole and aldehydes," *Journal of the American Chemical Society*, vol. 57, no. 10, pp. 2010–2011, 1935.
- [50] A. D. Adler, F. R. Longo, and W. Shergalis, "Mechanistic investigations of porphyrin syntheses. i. preliminary studies on ms-tetraphenylporphin," *Journal of the American Chemical Society*, vol. 86, no. 15, pp. 3145–3149, 1964.
- [51] A. D. Adler, F. R. Longo, J. D. Finarelli, J. Goldmacher, J. Assour, and L. Korsakoff, "A simplified synthesis for meso-tetraphenylporphine," *The Journal of Organic Chemistry*, vol. 32, no. 2, pp. 476–476, 1967.
- [52] Z.-C. Sun, Y.-B. She, Y. Zhou, X.-F. Song, and K. Li, "Synthesis, characterization and spectral properties of substituted tetraphenylporphyrin iron chloride complexes," *Molecules*, vol. 16, no. 4, pp. 2960–2970, 2011.

- [53] J. S. Lindsey and R. W. Wagner, "Investigation of the synthesis of ortho-substituted tetraphenylporphyrins," *The Journal of Organic Chemistry*, vol. 54, no. 4, pp. 828–836, 1989.
- [54] J. S. Lindsey, "Synthetic routes to meso-patterned porphyrins," *Accounts of chemical research*, vol. 43, no. 2, pp. 300–311, 2010.
- [55] A. Koc and D. Tuncel, "Supramolecular assemblies of cucurbiturils with photoactive, π -conjugated chromophores," *Israel Journal of Chemistry*, vol. 58, no. 3-4, pp. 334–342, 2018.
- [56] L. Chen, D. W. McBranch, H.-L. Wang, R. Helgeson, F. Wudl, and D. G. Whitten, "Highly sensitive biological and chemical sensors based on reversible fluorescence quenching in a conjugated polymer," *Proceedings of the National Academy of Sciences*, vol. 96, no. 22, pp. 12287–12292, 1999.
- [57] C. Fan, S. Wang, J. W. Hong, G. C. Bazan, K. W. Plaxco, and A. J. Heeger, "Beyond superquenching: hyper-efficient energy transfer from conjugated polymers to gold nanoparticles," *Proceedings of the National Academy of Sciences*, vol. 100, no. 11, pp. 6297–6301, 2003.
- [58] S. W. Thomas, G. D. Joly, and T. M. Swager, "Chemical sensors based on amplifying fluorescent conjugated polymers," *Chemical reviews*, vol. 107, no. 4, pp. 1339–1386, 2007.
- [59] X. Liu, T. Chen, F. Yu, Y. Shang, X. Meng, and Z.-R. Chen, "Aie-active random conjugated copolymers synthesized by admet polymerization as a fluorescent probe specific for palladium detection," *Macromolecules*, vol. 53, no. 4, pp. 1224–1232, 2020.
- [60] C. Wu, T. Schneider, M. Zeigler, J. Yu, P. G. Schiro, D. R. Burnham, J. D. McNeill, and D. T. Chiu, "Bioconjugation of ultrabright semiconducting polymer dots for specific cellular targeting," *Journal of the American Chemical Society*, vol. 132, no. 43, pp. 15410–15417, 2010.

- [61] K. Pu, A. J. Shuhendler, J. V. Jokerst, J. Mei, S. S. Gambhir, Z. Bao, and J. Rao, “Semiconducting polymer nanoparticles as photoacoustic molecular imaging probes in living mice,” *Nature nanotechnology*, vol. 9, no. 3, pp. 233–239, 2014.
- [62] P. Howes, R. Thorogate, M. Green, S. Jickells, and B. Daniel, “Synthesis, characterisation and intracellular imaging of peg capped behp-ppv nanospheres,” *Chemical communications*, no. 18, pp. 2490–2492, 2009.
- [63] J. H. Moon, “Conjugated polymers for gene delivery,” *Conjugated Polymers for Biological and Biomedical Applications*, pp. 215–241, 2018.
- [64] J. Pennakalathil, E. Jahja, E. S. Ozdemir, O. Konu, and D. Tuncel, “Red emitting, cucurbituril-capped, ph-responsive conjugated oligomer-based nanoparticles for drug delivery and cellular imaging,” *Biomacromolecules*, vol. 15, no. 9, pp. 3366–3374, 2014.
- [65] M. R. Antognazza, M. Di Paolo, D. Ghezzi, M. Mete, S. Di Marco, J. F. Maya-Vetencourt, R. Maccarone, A. Desii, F. Di Fonzo, M. Bramini, *et al.*, “Characterization of a polymer-based, fully organic prosthesis for implantation into the subretinal space of the rat,” *Advanced healthcare materials*, vol. 5, no. 17, pp. 2271–2282, 2016.
- [66] Kenry and B. Liu, “Recent advances in biodegradable conducting polymers and their biomedical applications,” *Biomacromolecules*, vol. 19, no. 6, pp. 1783–1803, 2018.
- [67] Z. Lu, Z. Zhang, and Y. Tang, “Conjugated polymers-based thermal-responsive nanoparticles for controlled drug delivery, tracking, and synergistic photodynamic therapy/chemotherapy,” *ACS Applied Bio Materials*, vol. 2, no. 10, pp. 4485–4492, 2019.
- [68] L. Feng, J. Zhu, and Z. Wang, “Biological functionalization of conjugated polymer nanoparticles for targeted imaging and photodynamic killing of tumor cells,” *ACS applied materials & interfaces*, vol. 8, no. 30, pp. 19364–19370, 2016.

- [69] H. Sun, F. Lv, L. Liu, Q. Gu, and S. Wang, “Conjugated polymer materials for photothermal therapy,” *Advanced Therapeutics*, vol. 1, no. 6, p. 1800057, 2018.
- [70] F. M. Raymo and J. F. Stoddart, “Interlocked macromolecules,” *Chemical reviews*, vol. 99, no. 7, pp. 1643–1664, 1999.
- [71] S. A. Nepogodiev and J. F. Stoddart, “Cyclodextrin-based catenanes and rotaxanes,” *Chemical reviews*, vol. 98, no. 5, pp. 1959–1976, 1998.
- [72] P. T. Glink, A. I. Oliva, J. F. Stoddart, A. J. White, and D. J. Williams, “Template-directed synthesis of a [2] rotaxane by the clipping under thermodynamic control of a crown ether like macrocycle around a dialkylammonium ion,” *Angewandte Chemie International Edition*, vol. 40, no. 10, pp. 1870–1875, 2001.
- [73] W. Abraham, L. Grubert, U. W. Grummt, and K. Buck, “A photoswitchable rotaxane with a folded molecular thread,” *Chemistry—A European Journal*, vol. 10, no. 14, pp. 3562–3568, 2004.
- [74] V. Ramalingam and A. R. Urbach, “Cucurbit [8] uril rotaxanes,” *Organic Letters*, vol. 13, no. 18, pp. 4898–4901, 2011.
- [75] Y. Min, J. M. Caster, M. J. Eblan, and A. Z. Wang, “Clinical translation of nanomedicine,” *Chemical reviews*, vol. 115, no. 19, pp. 11147–11190, 2015.
- [76] B. Pelaz, C. Alexiou, R. A. Alvarez-Puebla, F. Alves, A. M. Andrews, S. Ashraf, L. P. Balogh, L. Ballerini, A. Bestetti, C. Brendel, *et al.*, “Diverse applications of nanomedicine,” 2017.
- [77] M. L. Etheridge, S. A. Campbell, A. G. Erdman, C. L. Haynes, S. M. Wolf, and J. McCullough, “The big picture on nanomedicine: the state of investigational and approved nanomedicine products,” *Nanomedicine: nanotechnology, biology and medicine*, vol. 9, no. 1, pp. 1–14, 2013.
- [78] A. Z. Mirza and F. A. Siddiqui, “Nanomedicine and drug delivery: a mini review,” *International Nano Letters*, vol. 4, no. 1, p. 94, 2014.

- [79] K. C. Li, S. D. Pandit, S. Guccione, and M. D. Bednarski, “Molecular imaging applications in nanomedicine,” *Biomedical Microdevices*, vol. 6, no. 2, pp. 113–116, 2004.
- [80] I. Yacoby and I. Benhar, “Antibacterial nanomedicine,” 2008.
- [81] M.-G. Kim, J. Y. Park, Y. Shon, G. Kim, G. Shim, and Y.-K. Oh, “Nanotechnology and vaccine development,” *asian journal of pharmaceutical sciences*, vol. 9, no. 5, pp. 227–235, 2014.
- [82] J. A. Jackman, J. Lee, and N.-J. Cho, “Nanomedicine for infectious disease applications: innovation towards broad-spectrum treatment of viral infections,” *Small*, vol. 12, no. 9, pp. 1133–1139, 2016.
- [83] M. C. Arachchige, Y. K. Reshetnyak, and O. A. Andreev, “Advanced targeted nanomedicine,” *Journal of biotechnology*, vol. 202, pp. 88–97, 2015.
- [84] J. W. Cassidy, “Nanotechnology in the regeneration of complex tissues,” *Bone and tissue regeneration insights*, vol. 5, pp. BTRI-S12331, 2014.
- [85] M. Hajjalyani, D. Tewari, E. Sobarzo-Sánchez, S. M. Nabavi, M. H. Farzaei, and M. Abdollahi, “Natural product-based nanomedicines for wound healing purposes: therapeutic targets and drug delivery systems,” *International journal of nanomedicine*, vol. 13, p. 5023, 2018.
- [86] V. Kumar, S. Palazzolo, S. Bayda, G. Corona, G. Toffoli, and F. Rizzolio, “Dna nanotechnology for cancer therapy,” *Theranostics*, vol. 6, no. 5, p. 710, 2016.
- [87] H. Liu and T. J. Webster, “Nanomedicine for implants: a review of studies and necessary experimental tools,” *Biomaterials*, vol. 28, no. 2, pp. 354–369, 2007.
- [88] S. Aftab, A. Shah, A. Nadhman, S. Kurbanoglu, S. A. Ozkan, D. D. Dionysiou, S. S. Shukla, and T. M. Aminabhavi, “Nanomedicine: An effective tool in cancer therapy,” *International journal of pharmaceuticals*, vol. 540, no. 1-2, pp. 132–149, 2018.

- [89] Y. Xia, Y. Xiong, B. Lim, and S. E. Skrabalak, “Shape-controlled synthesis of metal nanocrystals: simple chemistry meets complex physics?,” *Angewandte Chemie International Edition*, vol. 48, no. 1, pp. 60–103, 2009.
- [90] B. Y. Kim, J. T. Rutka, and W. C. Chan, “Nanomedicine,” *New England Journal of Medicine*, vol. 363, no. 25, pp. 2434–2443, 2010.
- [91] X.-Q. Zhang, X. Xu, N. Bertrand, E. Pridgen, A. Swami, and O. C. Farokhzad, “Interactions of nanomaterials and biological systems: Implications to personalized nanomedicine,” *Advanced drug delivery reviews*, vol. 64, no. 13, pp. 1363–1384, 2012.
- [92] D. Peer, J. M. Karp, S. Hong, O. C. Farokhzad, R. Margalit, and R. Langer, “Nanocarriers as an emerging platform for cancer therapy,” *Nature nanotechnology*, vol. 2, no. 12, pp. 751–760, 2007.
- [93] J. M. Caster, A. N. Patel, T. Zhang, and A. Wang, “Investigational nanomedicines in 2016: a review of nanotherapeutics currently undergoing clinical trials,” *Wiley Interdisciplinary Reviews: Nanomedicine and Nanobiotechnology*, vol. 9, no. 1, p. e1416, 2017.
- [94] J.-M. Lehn, “Toward self-organization and complex matter,” *Science*, vol. 295, no. 5564, pp. 2400–2403, 2002.
- [95] H. Yang, B. Yuan, X. Zhang, and O. A. Scherman, “Supramolecular chemistry at interfaces: host–guest interactions for fabricating multifunctional biointerfaces,” *Accounts of chemical research*, vol. 47, no. 7, pp. 2106–2115, 2014.
- [96] S. Gürbüz, M. Idris, and D. Tuncel, “Cucurbituril-based supramolecular engineered nanostructured materials,” *Organic & biomolecular chemistry*, vol. 13, no. 2, pp. 330–347, 2015.
- [97] M. J. Webber and R. Langer, “Drug delivery by supramolecular design,” *Chemical Society Reviews*, vol. 46, no. 21, pp. 6600–6620, 2017.

- [98] M. W. Tibbitt, J. E. Dahlman, and R. Langer, "Emerging frontiers in drug delivery," *Journal of the American Chemical Society*, vol. 138, no. 3, pp. 704–717, 2016.
- [99] R. Haag, "Supramolecular drug-delivery systems based on polymeric core-shell architectures," *Angewandte Chemie International Edition*, vol. 43, no. 3, pp. 278–282, 2004.
- [100] N. Saleh, I. Ghosh, and W. M. Nau, "Cucurbiturils in drug delivery and for biomedical applications," *Supramolecular systems in biomedical fields*, no. 13, p. 164, 2013.
- [101] T. N. Seyfried and L. C. Huysentruyt, "On the origin of cancer metastasis," *Critical reviews in oncogenesis*, vol. 18, no. 1-2, p. 43, 2013.
- [102] U. Chilakamarthi and L. Giribabu, "Photodynamic therapy: past, present and future," *The Chemical Record*, vol. 17, no. 8, pp. 775–802, 2017.
- [103] J. Zhou, G. Yu, and F. Huang, "Supramolecular chemotherapy based on host-guest molecular recognition: a novel strategy in the battle against cancer with a bright future," *Chemical Society Reviews*, vol. 46, no. 22, pp. 7021–7053, 2017.
- [104] B. C. Wilson and M. S. Patterson, "The physics, biophysics and technology of photodynamic therapy," *Physics in Medicine & Biology*, vol. 53, no. 9, p. R61, 2008.
- [105] P. Agostinis, K. Berg, K. A. Cengel, T. H. Foster, A. W. Girotti, S. O. Gollnick, S. M. Hahn, M. R. Hamblin, A. Juzeniene, D. Kessel, *et al.*, "Photodynamic therapy of cancer: an update," *CA: a cancer journal for clinicians*, vol. 61, no. 4, pp. 250–281, 2011.
- [106] J. P. Celli, B. Q. Spring, I. Rizvi, C. L. Evans, K. S. Samkoe, S. Verma, B. W. Pogue, and T. Hasan, "Imaging and photodynamic therapy: mechanisms, monitoring, and optimization," *Chemical reviews*, vol. 110, no. 5, pp. 2795–2838, 2010.

- [107] Z. Zhou, J. Song, L. Nie, and X. Chen, “Reactive oxygen species generating systems meeting challenges of photodynamic cancer therapy,” *Chemical society reviews*, vol. 45, no. 23, pp. 6597–6626, 2016.
- [108] M.-F. Zuluaga and N. Lange, “Combination of photodynamic therapy with anti-cancer agents,” *Current medicinal chemistry*, vol. 15, no. 17, pp. 1655–1673, 2008.
- [109] K. Wu, H. Zhao, Z. Sun, B. Wang, X. Tang, Y. Dai, M. Li, Q. Shen, H. Zhang, Q. Fan, *et al.*, “Endogenous oxygen generating multifunctional theranostic nanoplatfrom for enhanced photodynamic-photothermal therapy and multimodal imaging,” *Theranostics*, vol. 9, no. 25, p. 7697, 2019.
- [110] Y. Liu, Y. Liu, W. Bu, C. Cheng, C. Zuo, Q. Xiao, Y. Sun, D. Ni, C. Zhang, J. Liu, *et al.*, “Hypoxia induced by upconversion-based photodynamic therapy: towards highly effective synergistic bioreductive therapy in tumors,” *Angewandte Chemie*, vol. 127, no. 28, pp. 8223–8227, 2015.
- [111] W. Park, S. Cho, J. Han, H. Shin, K. Na, B. Lee, and D.-H. Kim, “Advanced smart-photosensitizers for more effective cancer treatment,” *Biomaterials science*, vol. 6, no. 1, pp. 79–90, 2018.
- [112] Y. Liu, P. Bhattarai, Z. Dai, and X. Chen, “Photothermal therapy and photoacoustic imaging via nanotheranostics in fighting cancer,” *Chemical Society Reviews*, vol. 48, no. 7, pp. 2053–2108, 2019.
- [113] C. L. Ventola, “The antibiotic resistance crisis: part 1: causes and threats,” *Pharmacy and therapeutics*, vol. 40, no. 4, p. 277, 2015.
- [114] X. Li, B. Wu, H. Chen, K. Nan, Y. Jin, L. Sun, and B. Wang, “Recent developments in smart antibacterial surfaces to inhibit biofilm formation and bacterial infections,” *Journal of Materials Chemistry B*, vol. 6, no. 26, pp. 4274–4292, 2018.
- [115] X. Li, H. Bai, Y. Yang, J. Yoon, S. Wang, and X. Zhang, “Supramolecular antibacterial materials for combatting antibiotic resistance,” *Advanced Materials*, vol. 31, no. 5, p. 1805092, 2019.

- [116] K. Liu, Y. Liu, Y. Yao, H. Yuan, S. Wang, Z. Wang, and X. Zhang, "Supramolecular photosensitizers with enhanced antibacterial efficiency," *Angewandte Chemie International Edition*, vol. 52, no. 32, pp. 8285–8289, 2013.
- [117] L. Chen, H. Bai, J.-F. Xu, S. Wang, and X. Zhang, "Supramolecular porphyrin photosensitizers: Controllable disguise and photoinduced activation of antibacterial behavior," *ACS Applied Materials & Interfaces*, vol. 9, no. 16, pp. 13950–13957, 2017.
- [118] M. Özkan, Y. Keser, S. E. Hadi, and D. Tuncel, "A [5] rotaxane-based photosensitizer for photodynamic therapy," *European Journal of Organic Chemistry*, vol. 2019, no. 21, pp. 3534–3541, 2019.
- [119] M. Ozkan, Y. Kumar, Y. Keser, S. E. Hadi, and D. Tuncel, "Cucurbit [7] uril-anchored porphyrin-based multifunctional molecular platform for photodynamic antimicrobial and cancer therapy," *ACS Applied Bio Materials*, vol. 2, no. 11, pp. 4693–4697, 2019.
- [120] M. Özkan, S. E. Hadi, İ. Tunc, Y. Midilli, B. Ortaç, and D. Tuncel, "Cucurbit [7] uril-capped hybrid conjugated oligomer-gold nanoparticles for combined photodynamic-photothermal therapy and cellular imaging," *ACS Applied Polymer Materials*, 2020.
- [121] L. Wen, M. Li, and J. B. Schlenoff, "Polyporphyrin thin films from the interfacial polymerization of mercaptoporphyrins," *Journal of the American Chemical Society*, vol. 119, no. 33, pp. 7726–7733, 1997.
- [122] D. Tuncel, N. Cindir, and Ü. Koldemir, "[5] rotaxane and [5] pseudorotaxane based on cucurbit [6] uril and anchored to a meso-tetraphenyl porphyrin," *Journal of inclusion phenomena and macrocyclic chemistry*, vol. 55, no. 3-4, pp. 373–380, 2006.
- [123] Y. Kumar, B. Patil, A. Khaligh, S. E. Hadi, T. Uyar, and D. Tuncel, "Novel supramolecular photocatalyst based on conjugation of cucurbit [7]

- uril to non-metallated porphyrin for electrophotocatalytic hydrogen generation from water splitting,” *ChemCatChem*, vol. 11, no. 13, pp. 2940–2940, 2019.
- [124] F. Benyettou, H. Fahs, R. Elkharrag, R. A. Bilbeisi, B. Asma, R. Rezgui, L. Motte, M. Magzoub, J. Brandel, J.-C. Olsen, *et al.*, “Selective growth inhibition of cancer cells with doxorubicin-loaded cb [7]-modified iron-oxide nanoparticles,” *RSC advances*, vol. 7, no. 38, pp. 23827–23834, 2017.
- [125] N. Macia, R. Bresoli-Obach, S. Nonell, and B. Heyne, “Hybrid silver nanocubes for improved plasmon-enhanced singlet oxygen production and inactivation of bacteria,” *Journal of the American Chemical Society*, vol. 141, no. 1, pp. 684–692, 2018.
- [126] Q. Tian, F. Jiang, R. Zou, Q. Liu, Z. Chen, M. Zhu, S. Yang, J. Wang, J. Wang, and J. Hu, “Hydrophilic cu₉s₅ nanocrystals: a photothermal agent with a 25.7% heat conversion efficiency for photothermal ablation of cancer cells in vivo,” *ACS nano*, vol. 5, no. 12, pp. 9761–9771, 2011.
- [127] J. T.-W. Wang, U. Martino, R. Khan, M. Bazzar, P. Southern, D. Tuncel, and K. T. Al-Jamal, “Engineering red-emitting multi-functional nanocapsules for magnetic tumour targeting and imaging,” *Biomaterials Science*, vol. 8, no. 9, pp. 2590–2599, 2020.
- [128] A. L. Koner, I. Ghosh, N. Saleh, and W. M. Nau, “Supramolecular encapsulation of benzimidazole-derived drugs by cucurbit [7] uril,” *Canadian Journal of Chemistry*, vol. 89, no. 2, pp. 139–147, 2011.
- [129] Y. Zhao, M. H. Pourgholami, D. L. Morris, J. G. Collins, and A. I. Day, “Enhanced cytotoxicity of benzimidazole carbamate derivatives and solubilisation by encapsulation in cucurbit [n] uril,” *Organic & Biomolecular Chemistry*, vol. 8, no. 14, pp. 3328–3337, 2010.
- [130] Y. Zhao, D. P. Buck, D. L. Morris, M. H. Pourgholami, A. I. Day, and J. G. Collins, “Solubilisation and cytotoxicity of albendazole encapsulated in cucurbit [n] uril,” *Organic & Biomolecular Chemistry*, vol. 6, no. 24, pp. 4509–4515, 2008.

- [131] Z. Miskolczy, M. Megyesi, G. Tárkányi, R. Mizsei, and L. Biczók, "Inclusion complex formation of sanguinarine alkaloid with cucurbit [7] uril: inhibition of nucleophilic attack and photooxidation," *Organic & biomolecular chemistry*, vol. 9, no. 4, pp. 1061–1070, 2011.
- [132] H. Liu, X. Wu, Y. Huang, J. He, S.-F. Xue, Z. Tao, Q.-J. Zhu, and G. Wei, "Improvement of antifungal activity of carboxin by inclusion complexation with cucurbit [8] uril," *Journal of Inclusion Phenomena and Macrocyclic Chemistry*, vol. 71, no. 3-4, pp. 583–587, 2011.
- [133] A. C. Bhasikuttan, J. Mohanty, W. M. Nau, and H. Pal, "Efficient fluorescence enhancement and cooperative binding of an organic dye in a supra-biomolecular host–protein assembly," *Angewandte Chemie*, vol. 119, no. 22, pp. 4198–4200, 2007.
- [134] M. Megyesi, L. Biczók, and I. Jablonkai, "Highly sensitive fluorescence response to inclusion complex formation of berberine alkaloid with cucurbit [7] uril," *The Journal of Physical Chemistry C*, vol. 112, no. 9, pp. 3410–3416, 2008.
- [135] C.-F. Li, L.-M. Du, W.-Y. Wu, and A.-Z. Sheng, "Supramolecular interaction of cucurbit [n] urils and coptisine by spectrofluorimetry and its analytical application," *Talanta*, vol. 80, no. 5, pp. 1939–1944, 2010.
- [136] M. J. Pisani, Y. Zhao, L. Wallace, C. E. Woodward, F. R. Keene, A. I. Day, and J. G. Collins, "Cucurbit [10] uril binding of dinuclear platinum (ii) and ruthenium (ii) complexes: association/dissociation rates from seconds to hours," *Dalton Transactions*, vol. 39, no. 8, pp. 2078–2086, 2010.
- [137] N. Dong, S.-F. Xue, Q.-J. Zhu, Z. Tao, Y. Zhao, and L.-X. Yang, "Cucurbit [n] urils (n= 7, 8) binding of camptothecin and the effects on solubility and reactivity of the anticancer drug," *Supramolecular Chemistry*, vol. 20, no. 7, pp. 663–671, 2008.
- [138] G. Villarroel-Lecourt, J. Carrasco-Carvajal, F. Andrade-Villalobos, F. Solis-Egana, I. Merino-San Martín, J. Robinson-Duggon, and

- D. Fuentealba, "Encapsulation of chemotherapeutic drug melphalan in cucurbit [7] uril: Effects on its alkylating activity, hydrolysis, and cytotoxicity," *ACS omega*, vol. 3, no. 7, pp. 8337–8343, 2018.
- [139] D. Ma, G. Hettiarachchi, D. Nguyen, B. Zhang, J. B. Wittenberg, P. Y. Zavalij, V. Briken, and L. Isaacs, "Acyclic cucurbit [n] uril molecular containers enhance the solubility and bioactivity of poorly soluble pharmaceuticals," *Nature chemistry*, vol. 4, no. 6, pp. 503–510, 2012.
- [140] L. Cao, G. Hettiarachchi, V. Briken, and L. Isaacs, "Cucurbit [7] uril containers for targeted delivery of oxaliplatin to cancer cells," *Angewandte Chemie International Edition*, vol. 52, no. 46, pp. 12033–12037, 2013.
- [141] J. A. Plumb, B. Venugopal, R. Oun, N. Gomez-Roman, Y. Kawazoe, N. S. Venkataramanan, and N. J. Wheate, "Cucurbit [7] uril encapsulated cisplatin overcomes cisplatin resistance via a pharmacokinetic effect," *Metalomics*, vol. 4, no. 6, pp. 561–567, 2012.
- [142] A. R. Kennedy, A. J. Florence, F. J. McInnes, and N. J. Wheate, "A chemical preformulation study of a host–guest complex of cucurbit [7] uril and a multinuclear platinum agent for enhanced anticancer drug delivery," *Dalton Transactions*, no. 37, pp. 7695–7700, 2009.
- [143] Y. Zhao, M. S. Bali, C. Cullinane, A. I. Day, and J. G. Collins, "Synthesis, cytotoxicity and cucurbituril binding of triamine linked dinuclear platinum complexes," *Dalton Transactions*, no. 26, pp. 5190–5198, 2009.
- [144] D. P. Buck, P. M. Abeyasinghe, C. Cullinane, A. I. Day, J. G. Collins, and M. M. Harding, "Inclusion complexes of the antitumour metallocenes cp2mcl2 (m= mo, ti) with cucurbit [n] urils," *Dalton Transactions*, no. 17, pp. 2328–2334, 2008.
- [145] C. Kim, S. S. Agasti, Z. Zhu, L. Isaacs, and V. M. Rotello, "Recognition-mediated activation of therapeutic gold nanoparticles inside living cells," *Nature chemistry*, vol. 2, no. 11, pp. 962–966, 2010.

- [146] H. Cong, C.-R. Li, S.-F. Xue, Z. Tao, Q.-J. Zhu, and G. Wei, "Cucurbituril-resisted acylation of the anti-tuberculosis drug isoniazid via a supramolecular strategy," *Organic & biomolecular chemistry*, vol. 9, no. 4, pp. 1041–1046, 2011.
- [147] N. J. Wheate, V. Vora, N. G. Anthony, and F. J. McInnes, "Host–guest complexes of the antituberculosis drugs pyrazinamide and isoniazid with cucurbit [7] uril," *Journal of Inclusion Phenomena and Macrocyclic Chemistry*, vol. 68, no. 3-4, pp. 359–367, 2010.
- [148] N. Saleh, A. L. Koner, and W. M. Nau, "Activation and stabilization of drugs by supramolecular pka shifts: Drug-delivery applications tailored for cucurbiturils," *Angewandte Chemie*, vol. 120, no. 29, pp. 5478–5481, 2008.
- [149] C. Li, J. Li, and X. Jia, "Selective binding and highly sensitive fluorescent sensor of palmatine and dehydrocorydaline alkaloids by cucurbit [7] uril," *Organic & Biomolecular Chemistry*, vol. 7, no. 13, pp. 2699–2703, 2009.
- [150] Y. Zhou, H. Yu, L. Zhang, H. Xu, L. Wu, J. Sun, and L. Wang, "A new spectrofluorometric method for the determination of nicotine base on the inclusion interaction of methylene blue and cucurbit [7] uril," *Microchimica Acta*, vol. 164, no. 1-2, pp. 63–68, 2009.
- [151] N. Kahwajy, A. Nematollahi, R. R. Kim, W. B. Church, and N. J. Wheate, "Comparative macrocycle binding of the anticancer drug phenanthriplatin by cucurbit [n] urils, β -cyclodextrin and para-sulfonatocalix [4] arene: a 1 h nmr and molecular modelling study," *Journal of Inclusion Phenomena and Macrocyclic Chemistry*, vol. 87, no. 3-4, pp. 251–258, 2017.
- [152] S. Dutta Choudhury, J. Mohanty, A. C. Bhasikuttan, and H. Pal, "A fluorescence perspective on the differential interaction of riboflavin and flavin adenine dinucleotide with cucurbit [7] uril," *The Journal of Physical Chemistry B*, vol. 114, no. 33, pp. 10717–10727, 2010.
- [153] S. D. Choudhury, J. Mohanty, H. Pal, and A. C. Bhasikuttan, "Cooperative metal ion binding to a cucurbit [7] uril- thioflavin t complex: Demonstration

- of a stimulus-responsive fluorescent supramolecular capsule,” *Journal of the American Chemical Society*, vol. 132, no. 4, pp. 1395–1401, 2010.
- [154] I. W. Wyman and D. H. Macartney, “Host–guest complexations of local anaesthetics by cucurbit [7] uril in aqueous solution,” *Organic & biomolecular chemistry*, vol. 8, no. 1, pp. 247–252, 2010.
- [155] N. Saleh, M. A. Meetani, L. Al-Kaabi, I. Ghosh, and W. M. Nau, “Effect of cucurbit [n] urils on tropicamide and potential application in ocular drug delivery,” *Supramolecular Chemistry*, vol. 23, no. 9, pp. 650–656, 2011.
- [156] N. Saleh, M. B. Al-Handawi, M. S. Bufaroosha, K. I. Assaf, and W. M. Nau, “Tuning protonation states of tripeleennamine antihistamines by cucurbit [7] uril,” *Journal of Physical Organic Chemistry*, vol. 29, no. 2, pp. 101–106, 2016.
- [157] S. Li, H. Yin, G. Martinz, I. W. Wyman, D. Bardelang, D. H. Macartney, and R. Wang, “Supramolecular encapsulation of benzocaine and its metabolite para-aminobenzoic acid by cucurbit [7] uril,” *New Journal of Chemistry*, vol. 40, no. 4, pp. 3484–3490, 2016.
- [158] E. Corda, M. Hernandez, S. Sanchez-Cortes, and P. Sevilla, “Cucurbit [n] urils (n= 6–8) used as host molecules on supramolecular complexes formed with two different drugs: Emodin and indomethacin,” *Colloids and Surfaces A: Physicochemical and Engineering Aspects*, vol. 557, pp. 66–75, 2018.
- [159] X. Huang, Y. Tan, Q. Zhou, and Y. Wang, “Fabrication of cucurbit [6] uril mediated alginate physical hydrogel beads and their application as a drug carriers,” *e-polymers*, vol. 8, no. 1, 2008.
- [160] T. Minami, N. A. Esipenko, B. Zhang, M. E. Kozelkova, L. Isaacs, R. Nishiyabu, Y. Kubo, and P. Anzenbacher Jr, “Supramolecular sensor for cancer-associated nitrosamines,” *Journal of the American Chemical Society*, vol. 134, no. 49, pp. 20021–20024, 2012.

- [161] Y. Huang, S.-F. Xue, Z. Tao, Q.-J. Zhu, H. Zhang, J.-X. Lin, and D.-H. Yu, "Solubility enhancement of kinetin through host-guest interactions with cucurbiturils," *Journal of Inclusion Phenomena and Macrocyclic Chemistry*, vol. 61, no. 1-2, pp. 171-177, 2008.
- [162] Q. Zhang, G. Li, X. Xiao, S. Zhan, and Y. Cao, "Efficient and selective enrichment of ultratrace cytokinins in plant samples by magnetic perhydroxy-cucurbit [8] uril microspheres," *Analytical chemistry*, vol. 88, no. 7, pp. 4055-4062, 2016.
- [163] H. Yin, Q. Huang, W. Zhao, D. Bardelang, D. Siri, X. Chen, S. M. Lee, and R. Wang, "Supramolecular encapsulation and bioactivity modulation of a halonium ion by cucurbit [n] uril (n= 7, 8)," *The Journal of Organic Chemistry*, vol. 83, no. 8, pp. 4882-4887, 2018.
- [164] H. Feng, J. Kan, C. Redshaw, B. Bian, Z. Tao, and X. Xiao, "Supramolecular drug inclusion complex constructed from cucurbit [7] uril and the hepatitis b drug adefovir," *Supramolecular Chemistry*, vol. 31, no. 4, pp. 260-267, 2019.
- [165] Y. Huang, X.-Z. Fu, S.-F. Xue, Z. Tao, Q.-J. Zhu, and G. Wei, "Encapsulation of adefovir bis (l-leucine propyl) ester pro-virucide in cucurbit [7] uril and its activity against tobacco mosaic virus," *Supramolecular Chemistry*, vol. 25, no. 3, pp. 166-172, 2013.
- [166] H. S. El-Sheshtawy, S. Chatterjee, K. I. Assaf, M. N. Shinde, W. M. Nau, and J. Mohanty, "A supramolecular approach for enhanced antibacterial activity and extended shelf-life of fluoroquinolone drugs with cucurbit [7] uril," *Scientific reports*, vol. 8, no. 1, pp. 1-10, 2018.
- [167] S. K. Konda, R. Maliki, S. McGrath, B. S. Parker, T. Robinson, A. Spurling, A. Cheong, P. Lock, P. J. Pigram, D. R. Phillips, *et al.*, "Encapsulation of mitoxantrone within cucurbit [8] uril decreases toxicity and enhances survival in a mouse model of cancer," *ACS medicinal chemistry letters*, vol. 8, no. 5, pp. 538-542, 2017.

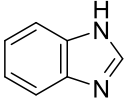
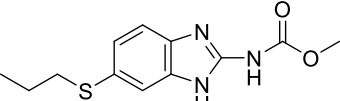
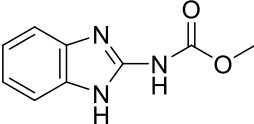
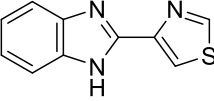
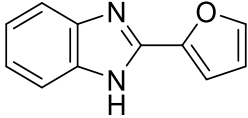
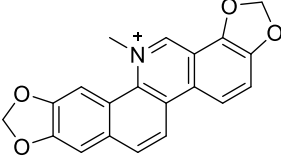
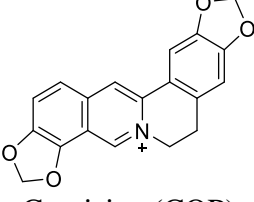
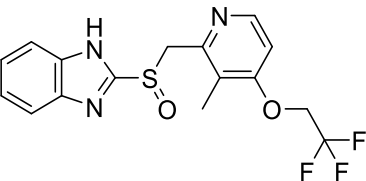
- [168] R. Wang, D. Bardelang, M. Waite, K. A. Udachin, D. M. Leek, K. Yu, C. I. Ratcliffe, and J. A. Ripmeester, "Inclusion complexes of coumarin in cucurbiturils," *Organic & Biomolecular Chemistry*, vol. 7, no. 11, pp. 2435–2439, 2009.
- [169] N. Barooah, J. Mohanty, H. Pal, and A. C. Bhasikuttan, "Stimulus-responsive supramolecular p k a tuning of cucurbit [7] uril encapsulated coumarin 6 dye," *The Journal of Physical Chemistry B*, vol. 116, no. 12, pp. 3683–3689, 2012.
- [170] N. Barooah, M. Sundararajan, J. Mohanty, and A. C. Bhasikuttan, "Synergistic effect of intramolecular charge transfer toward supramolecular p k a shift in cucurbit [7] uril encapsulated coumarin dyes," *The Journal of Physical Chemistry B*, vol. 118, no. 25, pp. 7136–7146, 2014.
- [171] W. M. Nau and J. Mohanty, "Taming fluorescent dyes with cucurbituril," *International Journal of Photoenergy*, vol. 7, 2005.
- [172] F. J. McInnes, N. G. Anthony, A. R. Kennedy, and N. J. Wheate, "Solid state stabilisation of the orally delivered drugs atenolol, glibenclamide, memantine and paracetamol through their complexation with cucurbit [7] uril," *Organic & Biomolecular Chemistry*, vol. 8, no. 4, pp. 765–773, 2010.
- [173] X. Wu, Y.-M. Zhang, and Y. Liu, "Nanosupramolecular assembly of amphiphilic guest mediated by cucurbituril for doxorubicin delivery," *RSC advances*, vol. 6, no. 102, pp. 99729–99734, 2016.
- [174] M. Özkan, Y. Keser, A. Koc, and D. Tuncel, "Glycosylated porphyrin-cucurbituril conjugate for photodynamic inactivation of bacteria and doxorubicin carriage for anticancer drug delivery," *Journal of Porphyrins and Phthalocyanines*, vol. 23, no. 11, pp. 1406–1413, 2019.
- [175] D. Ma, B. Zhang, U. Hoffmann, M. G. Sundrup, M. Eikermann, and L. Isaacs, "Acyclic cucurbit [n] uril-type molecular containers bind neuromuscular blocking agents in vitro and reverse neuromuscular block in vivo," *Angewandte Chemie*, vol. 124, no. 45, pp. 11520–11524, 2012.

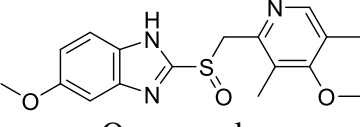
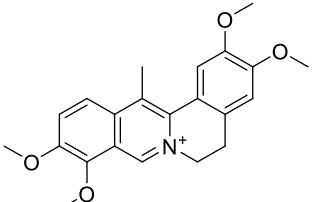
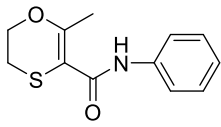
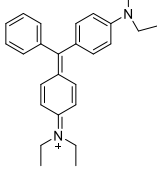
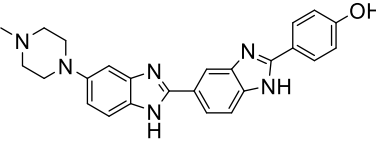
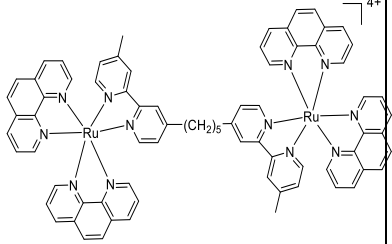
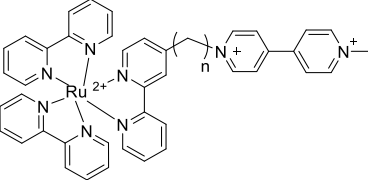
- [176] S. Sun, Y. He, Z. Yang, Y. Pang, F. Liu, J. Fan, L. Sun, and X. Peng, "Synthesis and dna photocleavage study of ru (bpy) 32^{+} -(ch 2) n-mv 2^{+} complexes," *Dalton Transactions*, vol. 39, no. 18, pp. 4411–4416, 2010.
- [177] H. Yin, L. Chen, B. Yang, D. Bardelang, C. Wang, S. M. Lee, and R. Wang, "Fluorescence enhancement and p k a shift of a rho kinase inhibitor by a synthetic receptor," *Organic & Biomolecular Chemistry*, vol. 15, no. 20, pp. 4336–4343, 2017.
- [178] H.-Y. Wang, Y. Zhou, J.-H. Lu, Q.-Y. Liu, G.-Y. Chen, Z. Tao, and X. Xiao, "Supramolecular drug inclusion complex of capecitabine with cucurbit [7] uril and inverted cucurbit [7] uril," *Arabian Journal of Chemistry*, vol. 13, no. 1, pp. 2271–2275, 2020.
- [179] R. Wang and D. H. Macartney, "Cucurbit [7] uril host–guest complexes of the histamine h2-receptor antagonist ranitidine," *Organic & Biomolecular Chemistry*, vol. 6, no. 11, pp. 1955–1960, 2008.
- [180] E. L. Robinson, P. Y. Zavalij, and L. Isaacs, "Synthesis of a disulfonated derivative of cucurbit [7] uril and investigations of its ability to solubilise insoluble drugs," *Supramolecular chemistry*, vol. 27, no. 5-6, pp. 288–297, 2015.
- [181] J. Vázquez, P. Remón, R. N. Dsouza, A. I. Lazar, J. F. Arteaga, W. M. Nau, and U. Pischel, "A simple assay for quality binders to cucurbiturils," *Chemistry—A European Journal*, vol. 20, no. 32, pp. 9897–9901, 2014.
- [182] W.-Y. Wu, J.-Y. Yang, L.-M. Du, H. Wu, and C.-F. Li, "Determination of ethambutol by a sensitive fluorescent probe," *Spectrochimica Acta Part A: Molecular and Biomolecular Spectroscopy*, vol. 79, no. 3, pp. 418–422, 2011.
- [183] H. Kim, J. Oh, W. S. Jeon, N. Selvapalam, I. Hwang, Y. H. Ko, and K. Kim, "A new cucurbit [6] uril-based ion-selective electrode for acetylcholine with high selectivity over choline and related quaternary ammonium ions," *Supramolecular Chemistry*, vol. 24, no. 7, pp. 487–491, 2012.

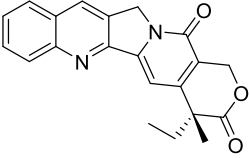
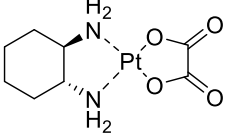
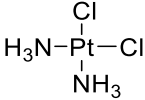
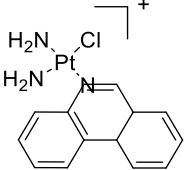
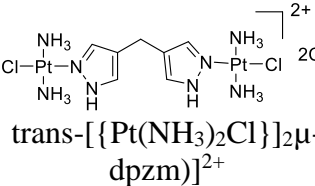
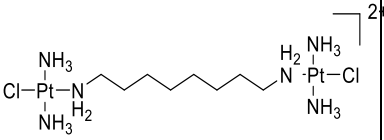
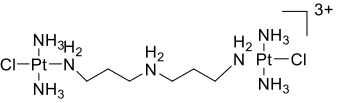
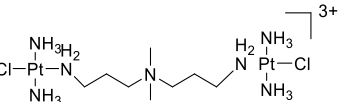
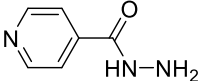
- [184] W. Li, S. Li, I. W. Wyman, D. H. Macartney, Q. Zhang, Y. Zheng, and R. Wang, "Supramolecular encapsulation of vitamin b6 by macrocyclic nanocontainer cucurbit [7] uril," *Journal of Nanomaterials*, vol. 2015, 2015.
- [185] N. Saleh, M. B. Al-Handawi, L. Al-Kaabi, L. Ali, S. S. Ashraf, T. Thiemann, B. Al-Hindawi, and M. Meetani, "Intermolecular interactions between cucurbit [7] uril and pilocarpine," *International Journal of Pharmaceutics*, vol. 460, no. 1-2, pp. 53–62, 2014.
- [186] S. Li, H. Yin, I. W. Wyman, Q. Zhang, D. H. Macartney, and R. Wang, "Encapsulation of vitamin b1 and its phosphate derivatives by cucurbit [7] uril: Tunability of the binding site and affinity by the presence of phosphate groups," *The Journal of Organic Chemistry*, vol. 81, no. 3, pp. 1300–1303, 2016.
- [187] Q. Zhang, Z. Zhen, H. Jiang, X.-G. Li, and J.-A. Liu, "Encapsulation of the ethylene inhibitor 1-methylcyclopropene by cucurbit [6] uril," *Journal of agricultural and food chemistry*, vol. 59, no. 19, pp. 10539–10545, 2011.
- [188] F. Chandra, P. Kumar, and A. L. Koner, "Encapsulation and modulation of protolytic equilibrium of β -carboline-based norharmane drug by cucurbit [7] uril and micellar environments for enhanced cellular uptake," *Colloids and Surfaces B: Biointerfaces*, vol. 171, pp. 530–537, 2018.
- [189] A. I. Lazar, F. Biedermann, K. R. Mustafina, K. I. Assaf, A. Hennig, and W. M. Nau, "Nanomolar binding of steroids to cucurbit [n] urils: selectivity and applications," *Journal of the American Chemical Society*, vol. 138, no. 39, pp. 13022–13029, 2016.

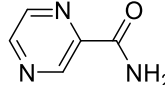
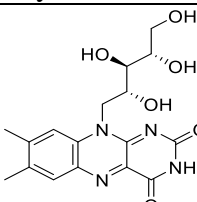
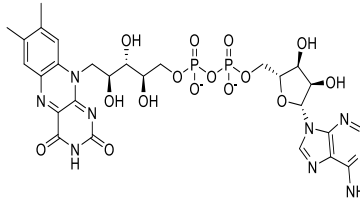
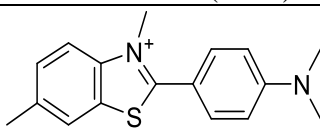
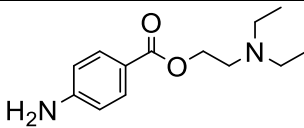
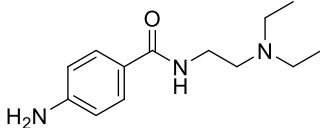
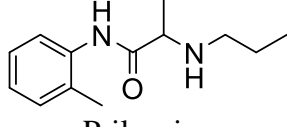
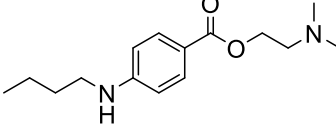
Appendix

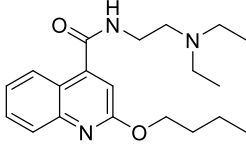
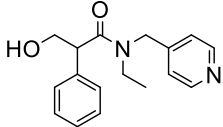
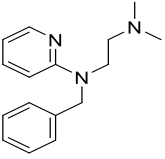
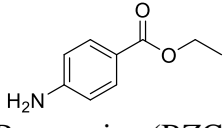
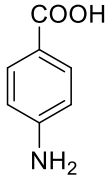
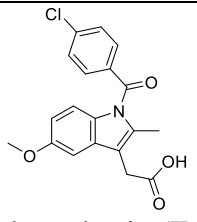
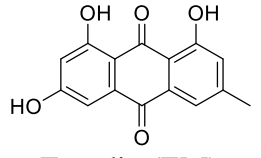
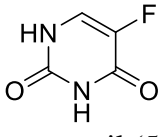
Table A.1: Cucurbituril-Biomolecule complexes in the literature

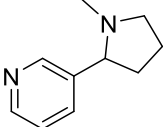
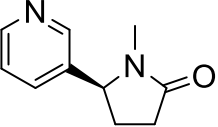
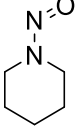
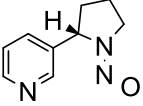
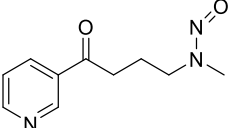
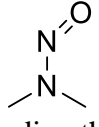
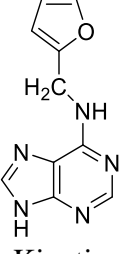
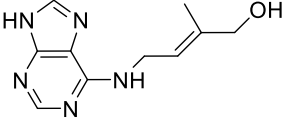
Guest	Function of Guest	Host CB	Advantage of Complexation	Reference
 <p>Benzimidazole (BZ)</p>	Anthelmintic drug	CB6, CB7, CB8	Water solubility was enhanced upon complexation by 1200-fold.	[128], [129]
 <p>Albendazole (ABZ)</p>	Anthelmintic drug	CB6, CB7, CB8	Water solubility was enhanced upon complexation by 2000-fold.	[128], [130]
 <p>Carbendazim (CBZ)</p>	Fungicide	CB7	Water solubility was enhanced upon complexation by 7-fold.	[128]
 <p>Thiabendazole (TBZ)</p>	Anthelmintic drug	CB7	Water solubility was enhanced upon complexation by 10-fold.	[128]
 <p>Fuberidazole (FBZ)</p>	Fungicide	CB7	Water solubility was enhanced upon complexation by 3-fold.	[128]
 <p>Sanguinarine</p>	Alkaloid antibiotic and botanical fungicide	CB7	Active sanguinarine was stabilized.	[131]
 <p>Coptisine (COP)</p>	Metabolite	CB5, CB6, CB7, CB8	Stability and fluorescence intensity of COP were increased.	[135]
 <p>Lansoprazole</p>	Proton pump inhibitor, prevents stomach and intestinal ulcers	CB7	Activation and stabilization were provided upon complexation.	[148]

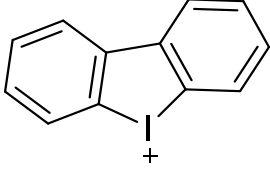
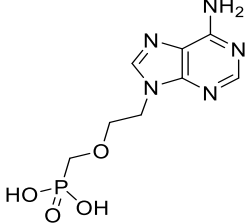
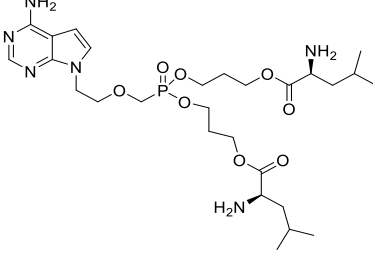
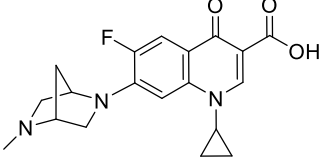
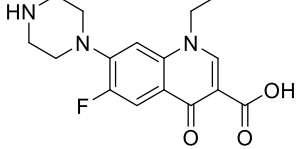
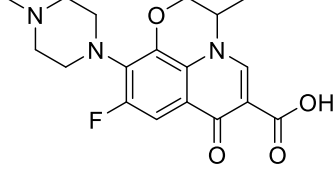
 <p>Omeprazole</p>	Proton pump inhibitor, prevents stomach and intestinal ulcers	CB7	Activation and stabilization were provided upon complexation.	[148]
 <p>Dehydrocorydaline</p>	Acetylcholinesterase inhibitor	CB7	Fluorescence intensity was enhanced upon complexation.	[149]
 <p>Carboxin</p>	Fungicide	CB8	Antifungal activity of carboxin towards <i>Rhizoctonia solani</i> was accomplished.	[132]
 <p>Brilliant Green (BG)</p>	Fluorochrome, histological dye, antiseptic drug, antibacterial agent	CB7	Binding of BG to bovine serum albumin (BSA) was increased in the presence of CB7.	[133]
 <p>Hoechst 33258</p>	Nucleic acid stain	CB7	Light-triggered release of Hoechst 33258 from Hoechst 33258-CB7 complex was shown.	[190]
 <p>[{Ru(phen)₂]₂(μbb₅)]⁴⁺{phen = 1,10-phenanthroline; bb₅ = 1,5-bis[4(4'-methyl-2,2'-bipyridyl)]pentane} (Rubb₅)</p>	Antibiotic	CB10	Strong inclusion complex formed.	[136]
 <p>Ruthenium(II) tris-bipyridly-(CH₂)_n-MV²⁺</p>	Agent used for DNA photocleavage	CB8	Ruthenium(II) tris-bipyridly-(CH ₂) _n -MV ²⁺ formed complex with CB8 and DNA photocleavage efficiency was increased by complexation.	[176]

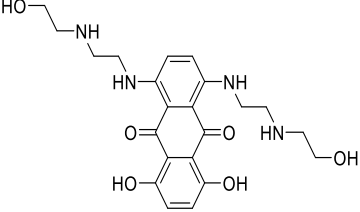
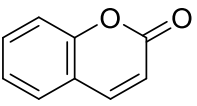
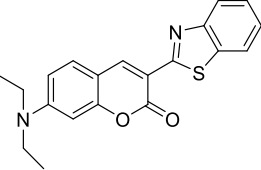
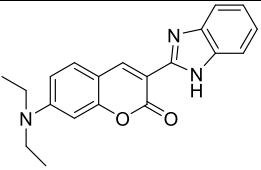
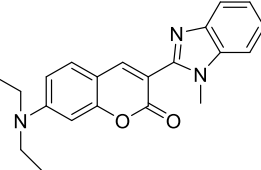
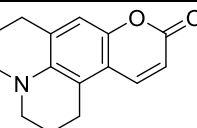
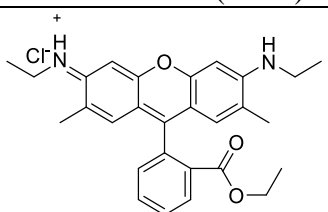
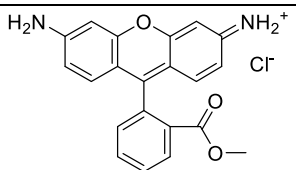
 <p>Camptothecin (CPT)</p>	Strong anti-tumor agent	CB7, CB8	<i>In vitro</i> study of targeted drug delivery towards A549, P388D1, MCF7 and MDA-MB-231 cell lines.	[137], [64]
 <p>Oxaliplatin</p>	Anti-cancer drug	CB7	Enhanced cytotoxicity in vitro towards L1210FR cells.	[140]
 <p>Cisplatin</p>	Anti-cancer drug	CB7	<i>In vitro</i> and <i>in vivo</i> studies confirmed that, complex defeats cisplatin resistance via pharmacokinetic effect.	[141]
 <p>Phenanthriplatin</p>	DNA-binding anti-cancer drug candidate	CB7, CB8	CB7 accommodates one equivalent phenanthriplatin molecule and CB8 accommodates two equivalent phenanthriplatin molecules.	[151]
 <p>trans-[[Pt(NH₃)₂Cl]₂(μ-dpzm)]²⁺</p>	DNA-binding anti-cancer Platinum complex	CB7	Stability was completely enhanced upon complexation.	[142]
 <p>trans-[[PtCl(NH₃)₂]₂(μNH₂(CH₂)₈NH₂)]²⁺</p> <p>CT008</p>	Antibiotic drug	CB10	Strong inclusion complex formed.	[136]
 <p>CT033</p>	Antibiotic drug	CB7, CB8	Enhanced cytotoxicity in vitro towards L1210 cells and cisplatin resistant subline L210/DDP.	[143]
 <p>CT233</p>	Antibiotic drug	CB7, CB8	Enhanced cytotoxicity in vitro towards L1210 cells and cisplatin resistant subline L210/DDP, however 50-times less active than CT033.	[143]
 <p>Isoniazid</p>	Antibiotic for tuberculosis	CB6, CB7	CB6 and CB7 assist hindrance of acylation of isoniazid.	[146]

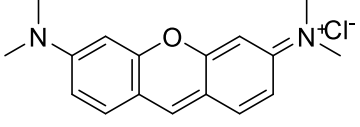
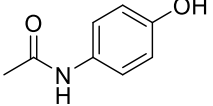
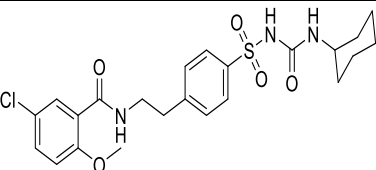
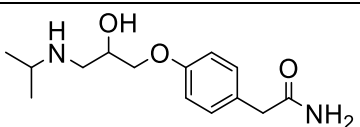
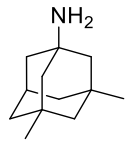
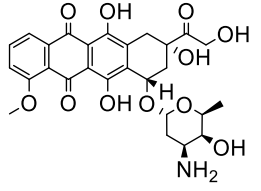
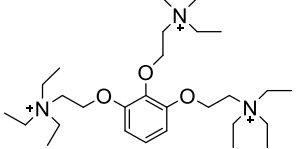
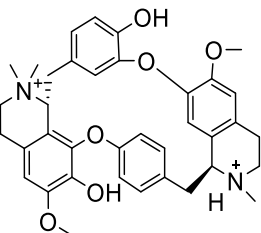
 Pyrazinamide	Medication to treat tuberculosis	CB7	Drug physical stability was achieved upon complexation.	[147]
 Riboflavin (RF)	Vitamin B2	CB7	Fluorescence intensity of RF was quenched upon complexation.	[152]
 Flavin Adenine Dinucleotide (FAD)	Human, <i>E. coli</i> and mouse metabolite	CB7	Fluorescence intensity of FAD was enhanced upon complexation.	[152]
 Thioflavin T (ThT)	Stain for amyloid	CB7	1:1 (CB7.ThT) and 2:1 [(CB7) ₂ .ThT] complexes formed and fluorescence intensities were enhanced upon addition of metal cations.	[153]
 Procaine	Local anesthetic	CB7	Very stable complex formed $K_{CB7} = (3.5 \pm 0.7) \times 10^4 \text{ dm}^3 \text{ mol}^{-1}$.	[154]
 Procainamide	Local anesthetic and medication for cardiac arrhythmias	CB7	Very stable complex formed $K_{CB7} = (7.8 \pm 1.6) \times 10^4 \text{ dm}^3 \text{ mol}^{-1}$.	[154]
 Prilocaine	Local anesthetic	CB7	Very stable complex formed $K_{CB7} = (2.6 \pm 0.6) \times 10^4 \text{ dm}^3 \text{ mol}^{-1}$.	[154]
 Tetracaine	Local anesthetic	CB7	Very stable complex formed $K_{CB7} = (1.5 \pm 0.4) \times 10^4 \text{ dm}^3 \text{ mol}^{-1}$.	[154]

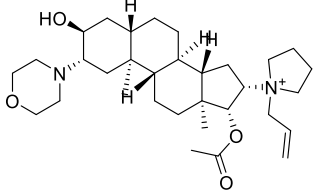
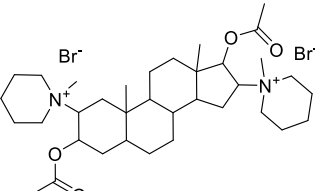
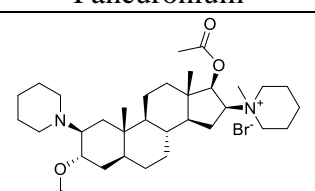
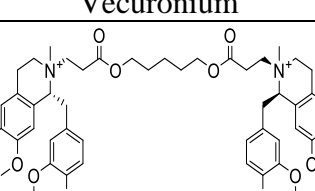
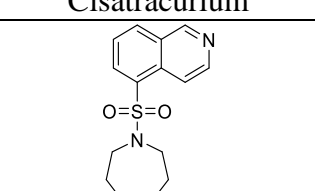
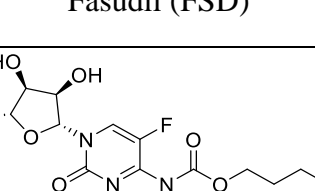
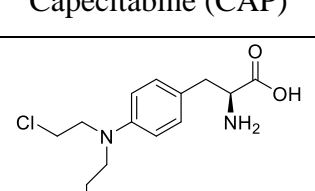
 <p>Dibucaine</p>	Local anesthetic	CB7	Very stable complex formed $K_{CB7} = (1.8 \pm 0.4) \times 10^5 \text{ dm}^3 \text{ mol}^{-1}$.	[154]
 <p>Tropicamide (TR)</p>	Ocular drug	CB7, CB8	TR formed 1:1 strong inclusion complex with CB7 and CB8.	[155]
 <p>Tripeleminamine (TRP)</p>	Antihistamine drug	CB7	TRP formed 1:1 strong complex with CB7.	[156]
 <p>Benzocaine (BZC)</p>	Local anesthetic	CB7	BZC formed 1:1 strong complex with CB7.	[157]
 <p><i>para</i>-aminobenzoic acid (PABA)</p>	Metabolite of BZC	CB7	PABA formed 1:1 strong complex with CB7.	[157]
 <p>Indomethacin (IM)</p>	Anti-inflammatory drug	CB6, CB8	Indomethacin formed complexes with CB6 (2:1) and CB8 (1:1) at pH = 6.	[158]
 <p>Emodin (EM)</p>	Anti-tumoral drug	CB6, CB7, CB8	Emodin formed complexes with CB6 (1:1), CB7 and CB8 (2:1) at pH = 2.	[158]
 <p>5-Fluorouracil (5-Flu)</p>	Anti-neoplastic agent	CB6	5-Flu was carried by CB6 mediated alginate hydrogel beads.	[159]

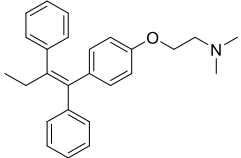
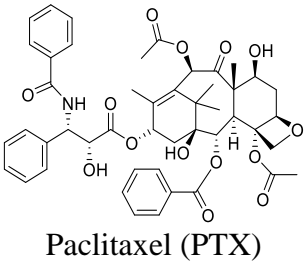


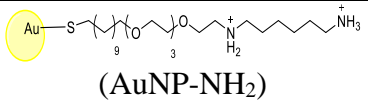
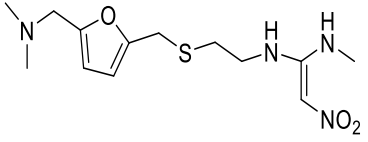
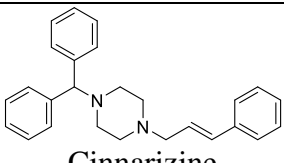
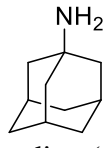
 Nicotine	Cancer-associated nitrosamine	CB7	Nicotine detection in aqueous solution was achieved by methylene blue-CB7 complex.	[150]
 Cotinine	Cancer-associated nitrosamine	Acyclic CBn	Conformationally flexible cross-reactive receptor was built for cotinine recognition.	[160]
 <i>N</i> -nitrosopiperidine (NPIP)	Cancer-associated nitrosamine	CB6	Very selective CB6 based supramolecular sensor was built for NPIP recognition.	[160]
 <i>N</i> -nitrosornicotine (NNN)	Cancer-associated nitrosamine	Acyclic CBn	Conformationally flexible cross-reactive receptor was built for NNN recognition.	[160]
 (4-methylnitrosamino)-1-(3-pyridyl)-1-butanone (NNK)	Cancer-associated nitrosamine	Acyclic CBn	Conformationally flexible cross-reactive receptor was built for NNK recognition.	[160]
 N-nitrosodimethylamine (NDMA)	Cancer-associated nitrosamine	CB6	Very selective CB6 based supramolecular sensor for NDMA recognition was built.	[160]
 Kinetin	Plant hormone promoting cell division	CB6, CB7	Water solubility of kinetin was enhanced upon complexation.	[161]
 Cytokinin	Plant hormone promoting cell division	CB8	Magnetic perhydroxy-CB8 microspheres were synthesized displaying high adsorption capacity for cytokinins in plant samples.	[162]

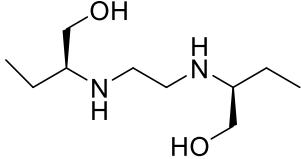
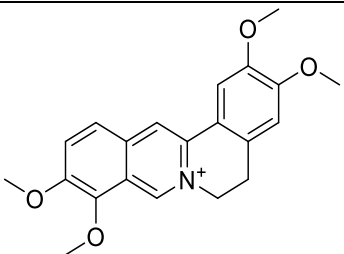
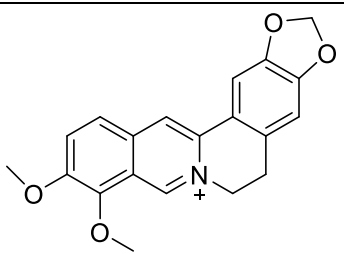
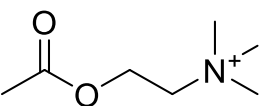
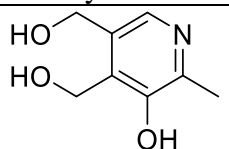
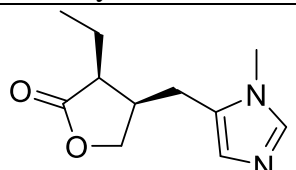
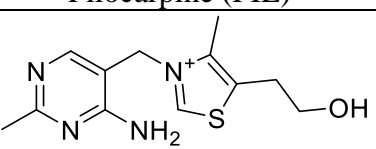
 <p>Diphenyleiodonium</p>	<p>NAD(P)H oxidase inhibitor</p>	<p>CB7, CB8</p>	<p>The inhibitory activity and cardiotoxicity of diphenyleiodonium was modulated upon complexation with CB7 (1:1) and CB8 (1:2).</p>	<p>[163]</p>
 <p>Adefovir (ADV)</p>	<p>Hepatitis B drug</p>	<p>CB7</p>	<p>ADV formed strong 1:1 inclusion complex with CB7.</p>	<p>[164]</p>
 <p>Adefovir bis(L-leucine propyl)ester (PMEA-Leu)</p>	<p>Pro-virucide</p>	<p>CB7</p>	<p>PMEA-Leu formed 2:1 host-guest complex with CB7 and this complex displayed some inhibitory activity against tobacco mosaic virus at 500 µg/ml <i>in vivo</i>.</p>	<p>[165]</p>
 <p>Danofloxacin (DOFL)</p>	<p>Fluoroquinolone antibiotic</p>	<p>CB7</p>	<p>The photostability and antibacterial activity (against <i>B. cereus</i>, <i>E. Coli</i>, <i>S. aureus</i> and <i>S. Typhi</i>) of DOFL was enhanced upon complexation with CB7.</p>	<p>[166]</p>
 <p>Norfloxacin (NRFL)</p>	<p>Fluoroquinolone antibiotic</p>	<p>CB7</p>	<p>The photostability and antibacterial activity (against <i>B. cereus</i>, <i>E. Coli</i>, <i>S. aureus</i> and <i>S. Typhi</i>) of NRFL was enhanced upon complexation with CB7.</p>	<p>[166]</p>
 <p>Ofloxacin (OFL)</p>	<p>Fluoroquinolone antibiotic</p>	<p>CB7</p>	<p>The photostability and antibacterial activity (against <i>B. cereus</i>, <i>E. Coli</i>, <i>S. aureus</i> and <i>S. Typhi</i>) of OFL was enhanced upon complexation with CB7.</p>	<p>[166]</p>

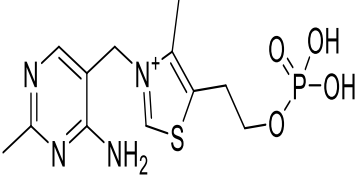
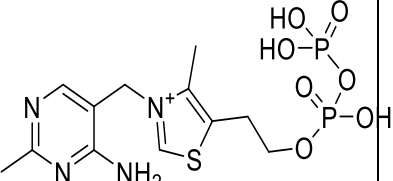

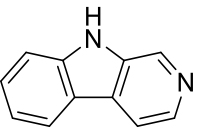
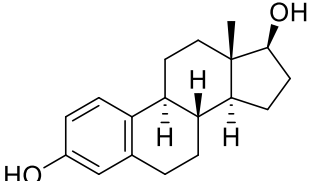
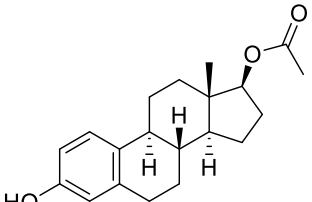
 <p>Mitoxantrone (Mito)</p>	Antineoplastic agent	CB8	Mito formed 1:2 host-guest complex with CB8 and this complex enhances Mito uptake in mouse cancer cells whereas it decreases toxicity of Mito in healthy mice.	[167]
 <p>Coumarin</p>	Anticoagulant	CB7, CB8	Coumarin formed host-guest inclusion complexes with CB7 (1:1) and CB8 (1:2).	[168]
 <p>Coumarin 6 (C6)</p>	Fluorescent dye	CB7	Stability and aqueous solubility of C6 was enhanced upon complexation with CB7.	[169]
 <p>Coumarin 7 (C7)</p>	Laser dye	CB7	Solubility and fluorescence intensity of C7 dye was enhanced upon complexation with CB7.	[170]
 <p>Coumarin 30 (C30)</p>	Laser dye	CB7	Solubility and fluorescence intensity of C30 dye was enhanced upon complexation with CB7.	[170]
 <p>Coumarin 102 (C102)</p>	Laser dye	CB7	Photostabilization of C102 was achieved upon complexation with CB7.	[171]
 <p>Rhodamine 6G</p>	Fluorescent dye, antineoplastic agent	CB7	Photostabilization of Rhodamine 6G was achieved upon complexation with CB7.	[171]
 <p>Rhodamine 123</p>	Fluorescent dye	CB7	Photostabilization of Rhodamine 123 was achieved upon complexation with CB7.	[171]

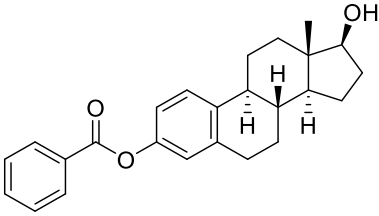
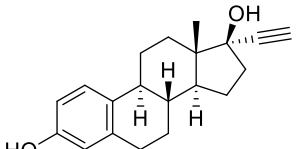
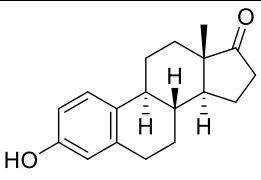
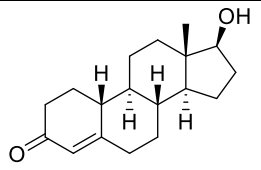
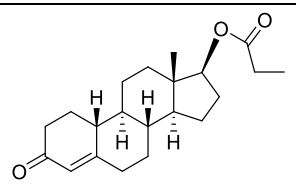
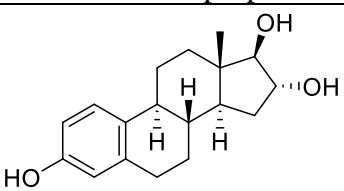
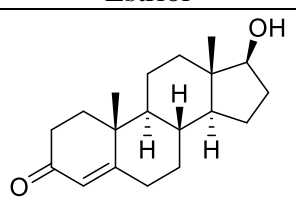
 <p>Pyronin Y</p>	Intercalating dye with a specificity towards RNA	CB7	Photostabilization of Pyronin Y was achieved upon complexation with CB7.	[171]
 <p>Paracetamol</p>	Analgesic and antipyretic drug	CB7	Paracetamol formed 1:1 inclusion complex with CB7 and it was physically stabilized upon complexation.	[172]
 <p>Glibenclamide</p>	Antidiabetic drug	CB7	Glibenclamide formed 1:1 inclusion complex with CB7 and it was physically stabilized upon complexation.	[172]
 <p>Atenolol</p>	Cardiovascular β -blocker drug	CB7	Atenolol formed 1:1 inclusion complex with CB7 and it was physically stabilized upon complexation.	[172]
 <p>Memantine</p>	Alzheimer's NMDA glutamate receptor drug	CB7	Memantine formed 1:1 inclusion complex with CB7 and it was physically stabilized upon complexation.	[172]
 <p>Doxorubicin (DOX)</p>	Chemotherapy drug	CB6, CB7	CB6 was utilized as targeted DOX carrier system against MCF-7 cell line ¹⁷³ and CB7 was used as DOX carrying system to MCF-7 without targeting ^{119,174} .	[173], [119], [174]
 <p>Gallamine</p>	Neuromuscular blocking drug	Acyclic CBn	Gallamine formed 1:1 host-guest complex with acyclic CBns. Complex reverses neuromuscular block <i>in vivo</i> .	[175]
 <p>Tubocurarine</p>	Neuromuscular blocking drug	Acyclic CBn	Tubocurarine formed 1:1 host-guest complex with acyclic CBns. Complex reverses neuromuscular block <i>in vivo</i> .	[175]

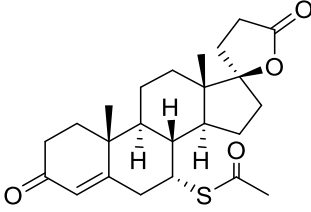
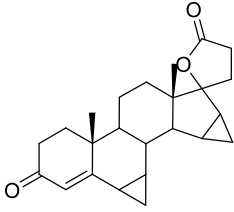
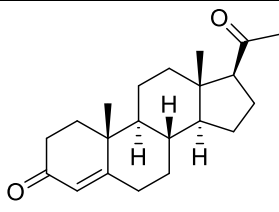
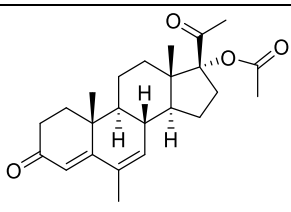
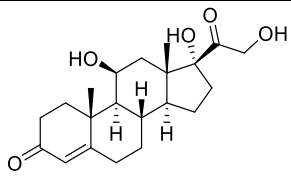
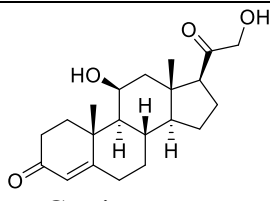
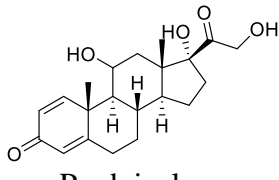
 <p>Rocuronium</p>	Neuromuscular blocking drug	Acyclic CBn	Rocuronium formed 1:1 host-guest complex with acyclic CBs. Complex reverses neuromuscular block <i>in vivo</i> .	[175]
 <p>Pancuronium</p>	Neuromuscular blocking drug	Acyclic CBn	Pancuronium formed 1:1 host-guest complex with acyclic CBns. Complex reverses neuromuscular block <i>in vivo</i> .	[175]
 <p>Vecuronium</p>	Neuromuscular blocking drug	Acyclic CBn	Vecuronium formed 1:1 host-guest complex with acyclic CBns. Complex reverses neuromuscular block <i>in vivo</i> .	[175]
 <p>Cisatracurium</p>	Neuromuscular blocking drug	Acyclic CBn	Cisatracurium formed 1:1 host-guest complex with acyclic CBns. Complex reverses neuromuscular block <i>in vivo</i> .	[175]
 <p>Fasudil (FSD)</p>	Selective rho kinase (ROCK) inhibitor	CB7	Fluorescence intensity of FSD was 69-fold enhanced upon complexation with CB7 and <i>in vitro</i> studies showed complexation preserved the drug's pro-neurite efficacy.	[177]
 <p>Capecitabine (CAP)</p>	Chemotherapy drug	CB7 and inverted CB7	CAP formed 1:1 host-guest inclusion complex with CB7 and inverted CB7.	[178]
 <p>Melphalan (Mel)</p>	Chemotherapy drug	CB7	<i>In vitro</i> targeted drug delivery towards HL-60 cell line was achieved.	[138]

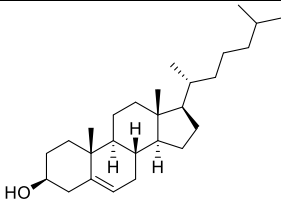
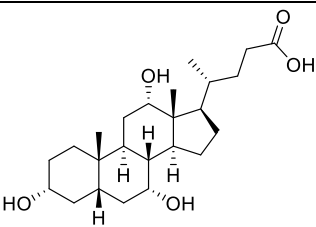
 <p>Tamoxifen</p>	Non-steroidal antiestrogen	CB7	Water solubility was enhanced upon complexation by 23 and 118-fold.	[139]
 <p>Paclitaxel (PTX)</p>	Chemotherapy drug	Acyclic CBn	Water solubility was enhanced upon complexation by 750-fold. In vitro studies of targeted drug delivery towards HEK293, HepG2, THP-1 cells and in vivo (female Swiss Webster mice).	[139]
 <p>Cp₂MoCl₂</p>	Antitumour metallocene	CB7, CB8	In vitro activity towards MCF-7 and 2008 cell lines.	[144]
 <p>Cp₂TiCl₂</p>	Antitumour metallocene	CB7, CB8	In vitro activity towards MCF-7 and 2008 cell lines.	[144]
 <p>(AuNP-NH₂)</p>	Therapeutic	CB7	Entrance into MCF-7 cells as non-toxic endosomes.	[145]
 <p>HCl Ranitidine hydrochloride</p>	Histamine H ₂ -receptor antagonist	CB7	CB7 formed very stable complexes with the diprotonated ($K_{CB7} = 1.8 \times 10^8 \text{ dm}^3 \text{ mol}^{-1}$), monoprotinated ($K_{CB7} = 1.0 \times 10^7 \text{ dm}^3 \text{ mol}^{-1}$), and neutral ($K_{CB7} = 1.2 \times 10^3 \text{ dm}^3 \text{ mol}^{-1}$) ranitidine in aqueous solution.	[179]
 <p>Cinnarizine</p>	Antihistamine and calcium channel blocker	CB7	Ability of CB7 to solubilize insoluble cinnarizine was shown.	[180]
 <p>Amantadine (AMA)</p>	Antiviral and antiparkinsonian agent	CB7, CB8	AMA formed stable complexes with CB7 and CB8 ($K_{CB7} = 1.2 \times 10^{10} \text{ M}^{-1}$ $K_{CB8} = 3.3 \times 10^7 \text{ M}^{-1}$).	[181]

 <p>Ethambutol (EMB)</p>	Antibiotic	CB7	The competitive complexation of EMB to CB7 was observed upon the release of the precomplexed fluorescent probes palmatine and berberine.	[182]
 <p>Palmatine</p>	Antimicrobial, anti-malarial, anti-inflammatory, antipyretic, hepatoprotective and antitumor agent	CB7	Fluorescence intensity was enhanced upon complexation.	[149]
 <p>Berberine</p>	Antilipemic drug, hypoglycemic agent, antineoplastic agent enzyme inhibitor	CB7	Stability and fluorescence intensity of berberine was increased upon complexation.	[134]
 <p>Acetylcholine</p>	Neurotransmitter	CB6	Acetylcholine formed stable complex with CB6 derivative ($K_a=5 \times 10^3 \text{ M}^{-1}$)	[183]
 <p>Pyridoxine</p>	Vitamin B ₆	CB7	Vitamin B ₆ formed 1:1 host-guest complex with CB7 ($K_a=4.0 \pm 0.5 \times 10^3 \text{ M}^{-1}$)	[184]
 <p>Pilocarpine (PIL)</p>	Drug to reduce pressure inside the eye and treat dry mouth	CB7	Stability of PIL was enhanced upon complexation.	[185]
 <p>Thiamine</p>	Vitamin B ₁	CB7	Thiamine formed 1:1 stable host-guest complex with CB7.	[186]

 <p>Thiamine monophosphate</p>	Phosphate derivative of Vitamin B ₁	CB7	Thiamine monophosphate formed 1:1 stable host-guest complex with CB7 and tunability of the binding site and affinity in the presence of phosphate group was shown.	[186]
 <p>Thiamine pyrophosphate</p>	Phosphate derivative of Vitamin B ₁	CB7	Thiamine pyrophosphate formed 1:1 stable host-guest complex with CB7 and tunability of the binding site and affinity in the presence of phosphate groups was shown.	[186]
 <p>1-Methylcyclopropene (1-MCP)</p>	Plant growth regulator	CB6	1-MCP formed complex with CB6 and its stability was enhanced upon complexation.	[187]
 <p>Norharmane (NHM)</p>	Anxiety control and memory-enhancing β -carboline-based drug	CB7	Solubility of NHM was enhanced by 15-fold upon complexation.	[188]
 <p>β-Estradiol</p>	Estrogen steroid hormone	CB7, CB8	β -Estradiol formed complexes with CB7 (120-fold solubility enhancement) and CB8 (7 fold solubility enhancement, $K_a = 1.9 \times 10^6 \text{ M}^{-1}$)	[189]
 <p>β-Estradiol 17-acetate</p>	The most active estrogen generated in human body	CB8	β -Estradiol 17-acetate formed complex with CB8 ($K_a = 6.5 \times 10^6 \text{ M}^{-1}$).	[189]

 <p>β-Estradiol 3-benzoate</p>	Estrogen steroid hormone	CB7, CB8	β -Estradiol 3-benzoate formed complexes with CB7 (36-fold solubility enhancement), CB8 (33 fold solubility enhancement, $K_a = 1.8 \times 10^6 \text{ M}^{-1}$).	[189]
 <p>17α-ethinyl estradiol</p>	The main component of oral contraceptives	CB8	17 α -ethinyl estradiol formed complex with CB8 ($K_a = 1.8 \times 10^6 \text{ M}^{-1}$).	[189]
 <p>Estrone</p>	Minor female sex hormone	CB7, CB8	Estrone formed complexes with CB7 (11-fold solubility enhancement), CB8 (2-fold solubility enhancement).	[189]
 <p>Nandrolone</p>	Androgen and anabolic steroid	CB7, CB8	Nandrolone formed 1:1 stable complex with CB7 ($K_a = 1.1 \times 10^7 \text{ M}^{-1}$) and CB8 ($K_a = 2.1 \times 10^7 \text{ M}^{-1}$).	[189]
 <p>Nandrolone 17-propionate</p>	Androgen and anabolic steroid	CB8	Nandrolone 17-propionate formed complex with CB8 ($K_a = 4.9 \times 10^6 \text{ M}^{-1}$).	[189]
 <p>Estriol</p>	Minor female sex hormone	CB7, CB8	Estriol formed complexes with CB7 (7-fold solubility enhancement), CB8 (2-fold solubility enhancement).	[189]
 <p>Testosterone</p>	Primary male sex hormone and an anabolic steroid	CB8	Testosterone formed complex with CB8 ($K_a = 1.1 \times 10^8 \text{ M}^{-1}$).	[189]

 <p>Spironolactone</p>	Medication to treat high blood pressure and heart failure	CB8	Spironolactone formed complex with CB8 ($K_a = 1.0 \times 10^6 \text{ M}^{-1}$) and its solubility was 5-fold increased upon complexation.	[189]
 <p>Drospirenone</p>	Synthetic progestin	CB7, CB8	Drospirenone formed complexes with CB7 (more than 4-fold solubility enhancement), CB8 (2-fold solubility enhancement, $K_a = 1.15 \times 10^8 \text{ M}^{-1}$).	[189]
 <p>Progesterone</p>	Steroid hormone	CB7, CB8	Progesterone formed complexes with CB7 (21-fold solubility enhancement), CB8 (8-fold solubility enhancement, $K_a = 9.3 \times 10^7 \text{ M}^{-1}$).	[189]
 <p>Megestrol acetate</p>	Appetite stimulant	CB7, CB8	Megestrol acetate formed complexes with CB7 (74-fold solubility enhancement), CB8 (72-fold solubility enhancement, $K_a = 1.6 \times 10^7 \text{ M}^{-1}$).	[189]
 <p>Cortisol</p>	Steroid hormone	CB8	Cortisol formed complex with CB8 ($K_a = 4.0 \times 10^6 \text{ M}^{-1}$).	[189]
 <p>Corticosterone</p>	Steroid hormone	CB8	Spironolactone formed complex with CB8 ($K_a = 1.3 \times 10^7 \text{ M}^{-1}$) and its solubility was 2-fold increased upon complexation.	[189]
 <p>Prednisolone</p>	Steroid drug	CB7, CB8	Prednisolone formed complexes with CB7 (2-fold solubility enhancement), CB8 ($K_a = 1.0 \times 10^6 \text{ M}^{-1}$).	[189]

 <p>Cholesterol</p>	<p>The membrane component</p>	<p>CB7, CB8</p>	<p>Cholesterol formed complexes with CB7 (255-fold solubility enhancement), CB8 (120-fold solubility enhancement).</p>	<p>[189]</p>
 <p>Cholic acid</p>	<p>Drug providing fat absorption and cholesterol excretion</p>	<p>CB7, CB8</p>	<p>Cholic acid formed complexes with CB7 (2-fold solubility enhancement), CB8 ($K_a = 0.2 \times 10^6 \text{ M}^{-1}$).</p>	<p>[189]</p>